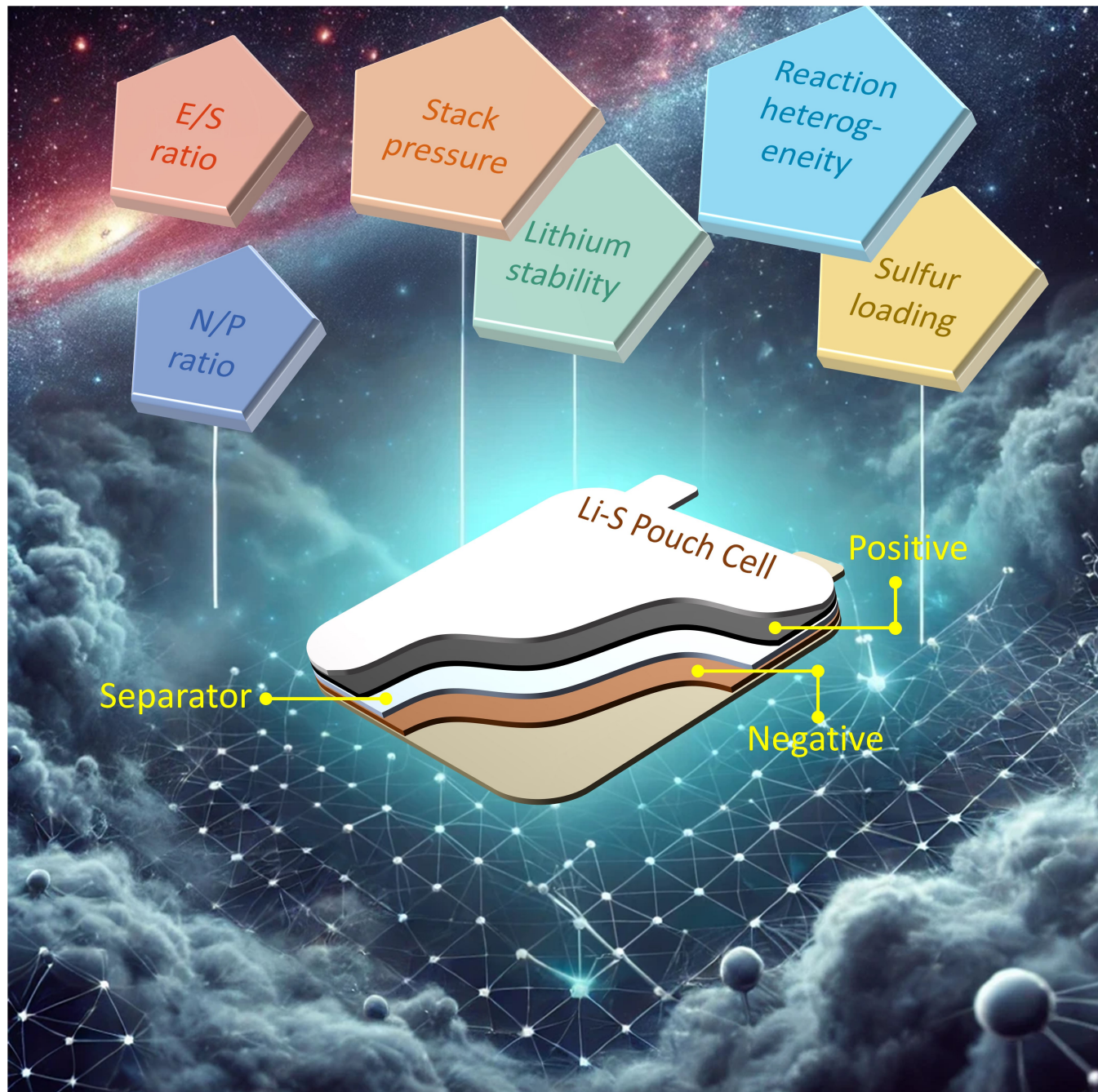


Challenges and Approaches to Designing High-Energy Density Lithium-Sulfur Pouch Cells

Srinidi Badhrinathan⁺^[a] Huidong Dai⁺^[b] and Gaind P. Pandey*^[a]



Lithium-sulfur (Li–S) batteries are of great interest as next-generation energy storage devices in a wide variety of applications, due to their high specific capacity and the environmental abundance of sulfur. However, liquid electrolyte Li–S technology faces several challenges such as polysulfide shuttling, anode corrosion and sluggish cathode kinetics. Practical deployment of Li–S batteries requires evaluation in large-format, high energy density pouch cells. Stringent operating conditions such as high sulfur loading and operating current, low electrolyte amount, and limited anode quantity are required for high energy density pouch cells, which further curtails the electrochemical performance and cycle life. This

review aims to provide an understanding of the different failure mechanisms of large-format Li–S pouch cells and formulate key design parameters of Li–S pouch cells that have high capacity, coulombic efficiency and long cycle life. Recent developments in Li–S pouch cells are then discussed, focusing on cathode and electrolyte design for polysulfide immobilization, accelerated sulfur conversion kinetics, and Li anode protection. A review of advanced characterization techniques suitable for Li–S pouch cell studies is also provided. Finally, viewpoints are offered on the remaining challenges and prospects to guide future research in scaling up Li–S technology for real-world applications.

1. Introduction

Over the past few decades, the widespread commercialization of lithium-ion batteries (LIBs) has been instrumental in the growth of many industries, such as portable electronics, aviation, and electric vehicles.^[1–3] Sustainable development of these industries alongside our existing energy infrastructure requires transitioning our energy production away from fossil fuels into cleaner and renewable sources, increasing the demand for higher energy storage greatly.^[4,5] The LIB technology faces limitations as the graphite anode's theoretical capacity is limited to 370 mAh g⁻¹,^[6,7] practically curtailing the cells' energy density to an upper limit of 400 Wh kg⁻¹.^[8] New energy storage devices suitable for powering everything from consumer electronics to grid storage must be developed to achieve better cost efficiency, safety, and high cell energy density >500 Wh kg⁻¹.^[9] Lithium-sulfur (Li–S) batteries have attracted significant worldwide interest due to their low cost and the high theoretical cell energy density of 2600 Wh kg⁻¹, which enables a theoretical specific capacity of 3860 Ah kg⁻¹.^[10] The 16-electron sulfur reduction reaction (SRR) yields a theoretical capacity of 1675 mAh g⁻¹, much superior to those achieved by insertion cathode materials and making elemental sulfur the ideal cathode pair for lithium metal anodes.^[11] Sulfur is economically favorable as a cheap and abundant material, and its low melting point enables energy-efficient cathode development and operation.^[12] However, Li–S batteries suffer from several key issues that hinder their practical applications.^[13–16] The insulating nature of sulfur and deposited Li₂S causes sluggish conversion kinetics and eventually passivate the cathode surface, which gradually reduces the cell capacity.^[17–20] The bottleneck “polysulfide shuttle effect”, in which soluble polysulfide reaction intermediates shuttle to the anode, irreversibly consumes sulfur and causes the formation of

powdery Li, which depletes the cell's active material as the lithium polysulfides (LiPS) attack and react with lithium metal.^[21,22] Furthermore, the plating/stripping of lithium occurs in a nonuniform manner, which causes uneven morphological evolution and volume change of the anode and exposes more lithium to parasitic side reactions with the electrolyte and polysulfides.^[23,24] The tendency of lithium metal to form dendrites at high or unevenly distributed current also poses short-circuit hazards.^[25] These issues reduce the cell's coulombic efficiency and cycle life due to early anode failure.^[26,27] The comparative ease of assembling coin cells to study newly developed components further confines progress in improving cell performance, as translating these achievements to practical cell sizes and formats becomes a hurdle.^[28] The complex array of challenges in the Li–S system requires a fundamental understanding of electrochemical processes, molecular dynamics, and materials engineering to fabricate long-cycling and high-energy Li–S cells.

In recent years, research efforts have focused on elucidating the multifaceted reactions associated with sulfur reduction as well as the non-electrochemical side reactions computationally and through advanced characterization efforts.^[11] Li–S systems fundamentally differ from conventional Li-ion batteries in that they operate on a conversion chemistry and the dynamics of battery operation are reliant on not only Li⁺ diffusion, but the relative concentrations of various polysulfide intermediates, the energetics of their interactions with the electrolyte, and the reversible deposition of the final solid product onto the cathode. The discharge process of Li–S batteries involves a series of two-phase, multi-step conversion of sulfur into various coexisting soluble lithium polysulfide (LiPS) intermediates before the final insoluble product is formed. Elemental sulfur (S₈) is converted to long-chain (Li₂S_n, 6 ≤ n ≤ 8) and intermediate (Li₂S_n, 4 ≤ n ≤ 6) polysulfides in a series of solid-liquid and liquid-liquid reactions.^[26,29] The SRR's rate-limiting step occurs at the second voltage plateau (2.1 V vs. Li/Li⁺), beginning at around 25% depth-of-discharge (DoD) and comprising the liquid-solid conversion of intermediate polysulfides to insoluble short-chain polysulfides, Li₂S₂/Li₂S, the final product (Figure 1a–b). The mechanisms of these reactions are complicated by the Li⁺ solvation dynamics of different electrolyte solvents that exert competing influences on soluble LiPS, creating concentration gradients that cause LiPS diffusion away from the cathode and

[a] S. Badhrinathan,[†] Dr. G. P. Pandey
Giner, Inc., 89 Rumford Avenue, Newton, MA 02466, United States
E-mail: gpp.ssi@gmail.com
gpandey@ginerinc.com

[b] Dr. H. Dai[†]
Department of Chemistry and Chemical Biology, Northeastern University,
360 Huntington Avenue, Boston, Massachusetts 02115, United States

[†] These authors contributed equally.

begin the shuttle effect.^[26] An additional layer of difficulty lies in distinguishing or isolating LiPS species through electrochemical methods due to their similar energy profiles. Moreover, polysulfides tend to constantly disproportionate or comproportionate into other S_n^{2-} species so that multiple species exist in the cell at any given time, causing overlapping signals.^[26]

One of the most prominent and effective strategies for addressing reaction kinetics and balancing polysulfide solvation in liquid Li–S batteries is tuning the electrolyte's interactions with Li^+ ions. Liquid electrolyte design for Li–S batteries focuses on stabilizing polysulfide intermediates favorable to SRR kinetics while maintaining high Li^+ conductivity, and promoting stable, homogeneous, and conductive solid-electrolyte interface (SEI) formation.^[30] Solvents are typically characterized by their donor number (DN), acceptor number (AN), and dielectric constant (ϵ) Figure 1c–e).^[31–33] Traditional carbonate solvents are not compatible with Li–S batteries as they react with polysulfide intermediates, irreversibly depleting the cell's active sulfur.^[34] Ionic liquids and high-salt-concentration electrolytes have been explored for their limited polysulfide solubility, often at the expense of ionic conductivity and electrode contact.^[35,36] Nowadays, ether-based electrolyte solvents such as 1,3-dioxolane/1,2-dimethoxyethane (DOL/DME) are commonly used due to their ability to solvate LiPS and enhance SRR kinetics, low resistance, and high Li^+ transference number, leading to low cell polarization^[29,37] Amine's group provided a backdrop parameter (relative solvating power) for understanding LiPS solvation-solvent structure relationships by correlating the solvents' structural features (polarity, steric hindrance) to electrochemical performance and thus the degree of LiPS dissolution.^[38] Ether solvents are conventionally paired with sulfonyl-based salts such as lithium

bis(trifluoromethanesulfonyl)imide (LiTFSI) and lithium bis(fluorosulfonyl)imide (LiFSI), which are electrochemically stable, lend high Li^+ conductivity and form an ion-conducting, LiPS-trapping LiF-based SEI.^[39] Due to their instability with aluminum current collectors, secondary salt additives such as lithium difluoro(oxalate)borate (LiODFB)^[40] that passivate the Al surface have been studied in small concentrations. Other explorations in the realm of lithium salts include lithium bis(oxalate)borate (LiBOB) and lithium bis(pentafluoroethanesulfonyl)imide (LiBETI)^[41] to enrich the Li surface morphology and manipulate LiPS solvation structure, respectively.

The bottleneck issue in lithium-sulfur batteries and the main inhibitor of stable, long-life battery cycling is the polysulfide shuttle effect. When the discharge process of the battery occurs, elemental sulfur is converted into soluble higher-order polysulfides. These polysulfides can dissolve into the electrolyte and shuttle to the anode, reacting parasitically with the Li metal to form lower-order polysulfides and corroding the anode. The deposition of insulating Li_2S_2/Li_2S also occurs onto the metal surface, passivating the lithium surface over continuous cycles. The weakly soluble lower-order polysulfides diffuse to the cathode in small amounts, are oxidized to form higher-order polysulfides during the charging process, and the shuttle repeats.^[42] This process depletes active material, causes severe anode corrosion and charging instability, and can eventually lead to cell failure.^[29,43] Researchers have explored several ways to mitigate the polysulfide shuttle effect, through modifying various components of the cell. One way is to prevent the formation of long-chain polysulfides completely by restricting cathodic sulfur in micropores, in which long-chain polysulfides cannot form due to size restrictions.^[44] Chemically or physically



Gaind P. Pandey is a Senior Project Scientist at Giner, Inc., Newton, Massachusetts. He received his Ph.D. degree in Physics from Pt. Ravishankar Shukla University, Raipur, India. Before joining the Giner, he was working as Research Scientist/Research Associate at various institutes including Virginia Commonwealth University, Xavier University of Louisiana, Kansas State University, and Binghamton University in USA. His research interests focus on the advanced Li-ion batteries, Li–S batteries, solid electrolytes/polymer electrolytes for solid-state batteries. Currently, he is leading Giner's efforts on Li–S scale-up to multi-layer pouch cell designs and electrolyte development for Li–S batteries.



Huidong Dai is a postdoctoral researcher at Northeastern University, USA, specializing in advanced battery technologies, particularly lithium-sulfur and lithium-ion batteries. He earned his Ph.D. from Stevens Institute of Technology, USA, where he focused on characterizing renewable energy materials using spectroscopy techniques, including Raman, FTIR, XRD, and synchrotron-based X-ray absorption spectroscopy (XAS). Dr. Dai has extensive experience in designing in-situ and operando experiments to advance the understanding of battery materials and their performance.



Srinidi Badhrinathan is a Staff Engineer at Giner Inc. She received her Bachelor of Science and Master of Science in Chemical Engineering from Drexel University, USA in 2022. Prior to joining Giner, her research focused on understanding hydrogen evolution kinetics on platinum catalysts for alkaline fuel cell applications. At Giner, she focuses on fabrication and testing of lithium-sulfur pouch cells. She also works on optimizing electrolyte and cathode design for lithium-sulfur batteries.

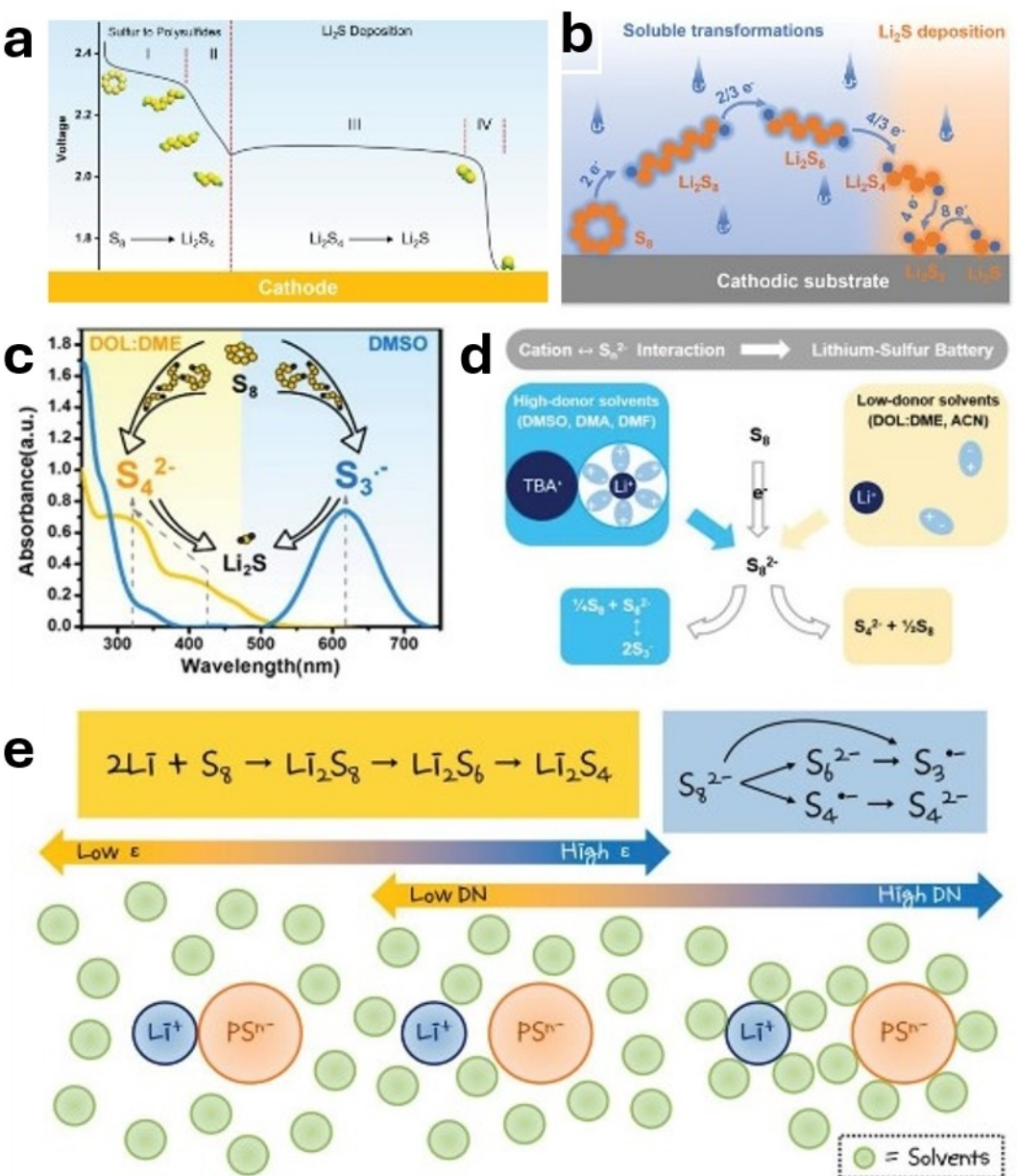


Figure 1. (a) Schematic of sulfur reduction reaction. Reproduced with permission.^[26] Copyright © 2022, L. Zhou et al., Wiley-VCH. (b) Schematic of polysulfides redox phase transformation. Reproduced with permission.^[70] Copyright © 2023, J. Sun et al., Wiley-VCH. (c) UV-vis spectra of S_4^{2-} and S_3^- radicals in DOL/DME and DMSO solvents. Reproduced with permission.^[31] Copyright © 2016, American Chemical Society. (d) Schematic of high- and low-donor solvents' interacting with S_8^{2-} species and resulting reaction mechanisms. Reproduced under terms of the CC-BY 4.0 license.^[32] (e) Schematic representation of solvent molecules' interaction with Li^+ ions and polysulfides based on dielectric constant and donor number. Reproduced under terms of the CC-BY 4.0 license.^[33]

confining formed polysulfides on the cathode through functionalized sulfur hosts,^[45,46] catalysts that increase the energetics of long-chain polysulfide conversion over dissolution,^[47–49] using sparingly solvating electrolytes that do not dissolve polysulfides,^[50,51] or designing polysulfide-trapping interlayers on the separator^[52] are other ways. Alternatively, strategies to prevent polysulfide-anode reactions and suppress dendritic Li formation through protective coatings on the anode,^[24,53] forming inorganic SEI layers that react with and consume polysulfides,^[54,55] or 3D lithium hosts that regulate lithium consumption and deposition^[56,57] also abound.

To address the problems of polysulfide dissolution and sluggish cathode redox kinetics, tuning the Li^+ solvation structure through sparingly solvating electrolytes and localized high concentration electrolytes (LHCEs) has lately received attention.^[58] LHCEs use various fluorinated ethers (such as 1,1,2,2-tetrafluoroethyl-2,2,3,3-tetrafluoropropyl ether (TTE),^[59] bis(2,2,2-trifluoroethyl) ether (BTFE)^[60]) to dilute the solvating power of DME/DOL, thereby locally decreasing ionic conductivity and reducing LiPS dissolution to mitigate the shuttle effect.^[61] These electrolyte systems achieve Li^+ ion coordination with anions along with solvents, leading to a more robust and

ionically conductive SEI composed of anion-based products.^[58,62] Zheng et al.'s recent work characterizing LiPS solvation in hydrofluoroether-containing electrolytes allows direct comparison of electrochemical performance and cycle life in strongly- and weakly-solvating electrolytes, which is critical to designing electrolytes that balance anode protection with cathode kinetic enhancement.^[63] The SEI plays a crucial role in mitigating issues like uneven Li deposition, dendrite growth, and high reactivity with the electrolyte. Unlike in-situ formed SEI, artificial SEI can be tailored to possess favorable properties such as uniform composition, high ionic conductivity, and suitable mechanical modulus.^[62,64,65] Organic-inorganic hybrid artificial SEI films can combine the strengths of both components, offering high strength, ionic conductivity, and flexibility to effectively protect the Li metal anode.^[66] Wang et al. and Liu et al. provide a comprehensive summary of Li–S electrolyte design concepts and other previously explored materials and formulations.^[30,67]

The overall SRR kinetics are further dependent on the cathode's microstructure, which controls accessibility of sulfur

to the electrolyte and provides avenues for SRR catalysis. Cathode development for Li–S batteries kickstarted in 2009 with Nazar's group's formative work on nanostructured conductive mesoporous carbon sulfur hosts to overcome the bottleneck issue of sulfur's insulating nature, allowing reversible cycling of Li–S batteries.^[68] Since then, most Li–S cells are assembled with sulfur/carbon (S/C) composite cathodes where sulfur is confined in microporous carbons. Cathode engineering and materials research has hitherto focused on addressing a few main challenges: i) improving sulfur's electrochemical properties and achieving high-performing, high-sulfur-loaded cathodes through designing nanostructured S/C matrices, ii) encapsulating soluble LiPS physically or chemically to prevent the shuttle effect which depletes active sulfur, iii) maintaining the cathode structure during the large volume expansion (80%) caused by lithiation/delithiation, and iv) incorporating catalysts for favorable polysulfide conversion and Li₂S deposition energetics^[27,69,70] (Figure 2a). The selection of conductive polymer binders (such as polyvinylidene difluoride (PVdF),

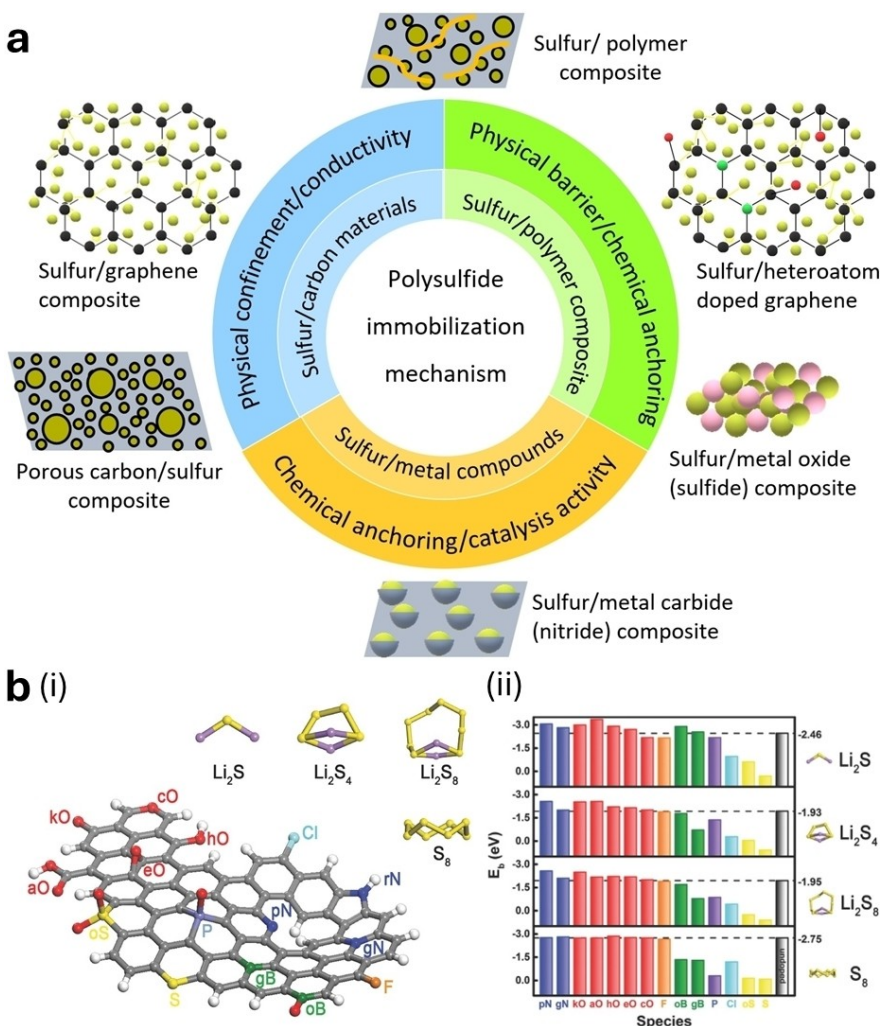


Figure 2. (a) Summary of polysulfide encapsulation strategies with nanostructured cathode materials. Reproduced with permission.^[69] Copyright © 2022, M.A. Weret et al., Wiley-VCH. (b) X-doped graphene nanowires (X=N, O, F, B, P, S, Cl), (i) Schematic of doped nanowires and polysulfide intermediates' structures, (ii) binding energies of X-doped graphene nanowires interacting with various polysulfide intermediates. Reproduced with permission.^[73] Copyright © 2016, T.Z. Hou et al., Wiley-VCH.

poly(acrylic acid) (PAA)) plays a critical role in achieving high areal sulfur loading, maintaining electrochemical contact between composite cathode particles during cycling, and forming pores for appropriate electrolyte uptake.^[29,71] Heteroatom-doped carbon materials such as nitrogen-doped carbon, N-doped carbon nanotubes, and N-doped graphene which chemically bond with and anchor LiPS have received extensive attention^[72,73] (Figure 2b). Polymer-sulfur crosslinked nanocomposites (such as polyacrylonitrile (PAN)/sulfur, poly(3,4-ethylenedioxythiophene) (PEDOT)/sulfur) and polymer-carbon structures are another promising avenue as these can generally be synthesized below 100 °C, can be self-healing to accommodate volume expansion, and can be tuned with the addition of different functional groups to improve polysulfide anchoring.^[74] Metal-organic frameworks (MOFs) cannot be utilized as sole sulfur hosts due to their poor conductivity, but are attractive in composites due to their ultrahigh porosity and tunability which allow high sulfur loading, electrolyte uptake, and accommodate volume expansion.^[75,76] Reviews by Manthiram's group, Ong's group and Mori provide fundamental understanding of structure-activity relationships for organic and inorganic cathode materials and summarize design of sulfur hosts and catalysts over the past several years.^[72,77,78]

High-performing Li–S batteries must also incorporate lithium metal anode protection strategies to prevent coulombic efficiency and capacity fade, as Li metal is thermodynamically unstable with conventional ether and carbonate electrolytes.^[24] The formation of an ionically conductive SEI layer is desirable to prevent anode corrosion through extensive electrolyte reactions, but SEI growth increases interfacial impedance due to build-up of Li-electrolyte reaction products, which reduces cyclability and can cause cell failure.^[64] Uncontrolled SEI growth consumes the cell's active material and leads to "dead" lithium when plated lithium is deposited inside the thick SEI, away from the current collector.^[79] Morphological changes in the anode during plating/stripping at high current density also lead to rapid and uneven lithium deposition and the well-documented growth of lithium dendrites that penetrate the SEI and separator and short-circuit the cell.^[80] To overcome these challenges, anode protection strategies validated at the lab-scale include construction of an artificial SEI through electrolyte additives for dendrite blocking, designing Li⁺ conductive interlayers on the separator/anode to prevent LiPS-anode contact,^[81,82] and introducing 3D host architectures (composite Li metal anodes with organic or inorganic host materials) to control and homogenize Li deposition.^[83,84] The use of LiNO₃ as an SEI-former that reacts with dissolved polysulfides to form various Li_xNO_y and Li_xSO_y species has been well-documented, and the formed SEI shows good mechanical integrity, suppresses dendrites and promotes uniform deposition of a pancake-like lithium.^[85] Jozwiuk et al. further observed suppressed gas evolution in cells containing LiNO₃ as gas-forming products are instead absorbed into the SEI, and polysulfide side reactions are suppressed by LiNO₃-LiPS reactions.^[86] Alternatively, Meng's group carried out a study on tuning the direction and density of Li deposition though stack pressure and achieved stable, reversible cycling with a columnar Li deposi-

tion by preserving the base of the SEI during stripping.^[87] Zhang's group has published recent reviews on Li dendrite suppression and anode protection that provide further insight into electrolyte additives for SEI formation and the dynamics of Li plating/stripping.^[88,89]

Despite significant progress achieved in optimizing Li–S battery components over the past decade, translating cell performance improvements into larger formats remains a challenge.^[4,28,90] Most academic experiments occur in coin cells, which are easy to build and reproduce and suitable for developing and characterizing individual cell components (Figure 3a). However, coin cells provide capacities in the mAh range and cannot be directly scaled up for heavy-duty applications such as electric vehicles and aviation technologies that demand >500 Wh kg⁻¹ cell-level energy density.^[28,91] The key to increasing energy density lies in maximizing cell performance while minimizing component weights.^[8,92] Several larger formats such as prismatic, cylindrical and pouch-type cells have been developed, of which pouch cells are the most versatile and suitable for increasing energy density due to their comparatively low cell packaging weight.^[28] Li–S pouch cells have been increasingly used for materials development since 2014 also due to their optimal configuration for reducing electrolyte amount while maintaining cyclability.^[93] Pouch cells involve the stacking of rectangular negative and positive electrodes in single or multiple layers with separator sheets placed in between. The usage of multiple electrode layers allows precise control of the cell size and scale-up with minimal effort (Figure 3b–i).

The key parameters for increasing pouch cells' energy density above 300 Wh kg⁻¹ include increasing cathodes' areal sulfur loading (>6 mg cm⁻²), reducing electrolyte-to-sulfur (E/S) ratio under 5 µL mg⁻¹ and controlling the negative-to-positive (N/P) electrode ratio below 3^[94] (Figure 3b). For comparison, coin cells typically use low sulfur-loaded cathodes, thick lithium chips (N/P ratio >100) and flooded electrolytes (E/S ratio >20 µL mg⁻¹). The curtailment of active components and electrolytes in pouch cells naturally compromises the cycling performance due to reduced reaction kinetics, primarily during discharge. The increased areal loading causes high areal current density on the lithium anode, which worsens the growth of lithium dendrites and nonuniform Li deposition.^[90] Applied stack pressure in pouch cells is much lower than crimped coin cells and can vary across the larger length scale of pouch cells (Figure 3). This has the dual effect of i) affecting cathode porosity in certain regions, which can increase or decrease electrolyte diffusion to those areas and cause spatial variation in sulfur redox and side kinetics, further leading to over- or under-utilized active material^[95]; and ii) varying the Li deposition density and morphology regionally, which can lead to dendrite growth, SEI inhomogeneity, and dead lithium formation.^[96] Pouch cell performance has improved over the past decade, but still falls short of consistently reaching 500 Wh kg⁻¹ or cycling for more than 100 cycles due to the different failure mechanisms in these cells and the difficulty of scaling up coin cell improvements. Also, addressing one challenge in large cells often comes at the expense of others—for example, increasing

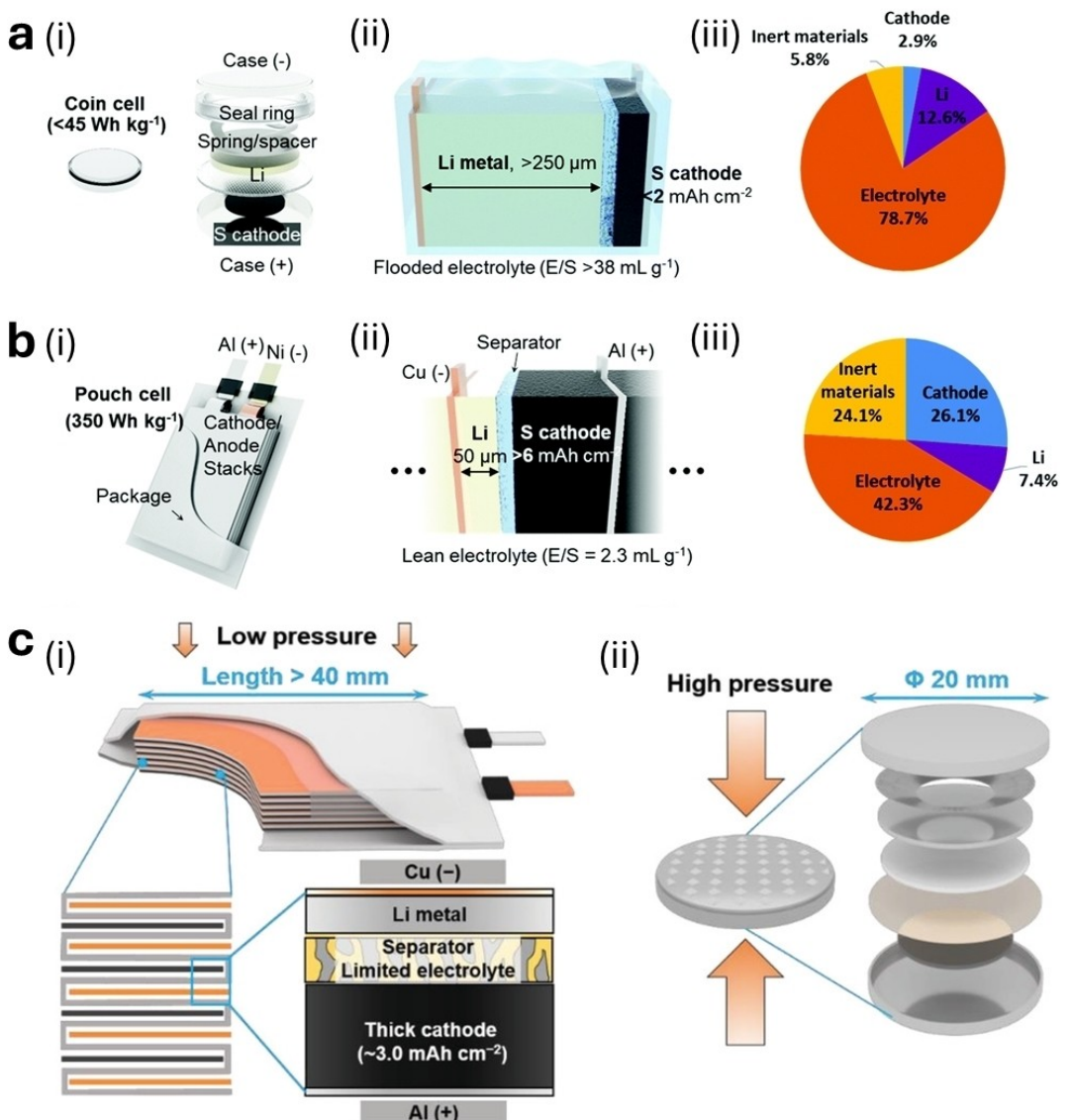


Figure 3. Comparison of coin cells and pouch cells. (a) Standard coin cell design, (b) Standard pouch cell design, (i) assembly, (ii) visual of component ratios, (iii) approximate percentages of component weights. Reproduced with permission.^[94] Copyright © 2020, Royal Society of Chemistry. (c) Stack pressure comparison for (i) pouch cells and (ii) coin cells. Reproduced with permission.^[91] Copyright © 2022, H. Liu et al., Wiley-VCH.

carbon fraction in the cathode provides increased conductivity and surface area for reaction sites, but lowers the amount of active material and the volumetric energy density. Various cathode engineering strategies to increase sulfur loading and utilization, anode protection methods, separator coatings, electrocatalysts and redox mediators have been deployed to improve pouch cell performance. A comprehensive review of recent advancements in Li–S pouch cells is essential at this juncture to underscore the significant breakthroughs achieved in various components at the laboratory scale. Additionally, summarizing the current state-of-the-art characterization methods for Li–S cells will be invaluable for troubleshooting and designing novel battery systems. Consolidating these developments in one place provides a pathway to integrate effective strategies, thereby facilitating the creation of high-energy density, long-cycling lithium-sulfur pouch cells.

In this comprehensive review, we first discuss illustrative failure analysis studies of pouch cells and use the deductions to develop form factors for the design and operation of high energy pouch cells. Although Li–S technology has received great interest in the past decade, validating developments in high-energy-density pouch cells and overcoming the challenges of scale-up is still necessary to realize the full potential of this system at the device level. This review provides pathways towards understanding and addressing the performance decay in pouch cells and identifies the key factors to optimize in designing high-performing Li–S batteries. We further explore recent achievements in pouch cell performance improvement, covering innovations in cathode structure and anode protection strategies, and close out with an overview of advanced techniques for characterizing and studying molecular phenomena unique to pouch cells. The takeaways from the highlighted

studies, each focusing on a particular component of battery design, are expected to synergistically guide future academic and industrial research in this field.

2. Failure Mechanisms of Pouch Cells

It is generally acknowledged that although the fundamental electrochemical principles of Li–S systems remain the same, scaling up the cell size from coin to pouch cells inevitably changes the electrochemical performance and failure mechanisms of the cells. To achieve practical energy densities of 400–500 Wh kg⁻¹, it is necessary to operate Li–S pouch cells at lean electrolyte and low N/P conditions in order to reduce the weight of the cells. These constrained conditions combined with high operating current and regional variation in large electrodes cause reduced capacity, coulombic efficiency, and cycle life. This review covers failure analyses of pouch cells in three categories: i) studying evolving electrode morphologies and compositions during cycling to determine reaction-related failure mechanisms, ii) evaluating thermal runaway mechanisms under abuse conditions, and iii) calendar ageing to determine intrinsic failure mechanisms occurring during storage.

2.1. Spatial Reaction Heterogeneity During Cycling

Spatial heterogeneity in both the SRR and side reactions is known to be a leading cause for pouch cell failure, but there is room to investigate component-level cycling evolutions to pinpoint the mechanisms of heterogeneity. Pouch cell cathodes must have high areal sulfur loadings >5 mg cm⁻² to increase

energy density above 350 Wh kg⁻¹, which results in large and unevenly distributed areal current density on the anode surface and nonuniform plating/stripping of Li in turn. This facilitates Li dendrite nucleation and increases Li surface area for SEI formation, which consumes electrolyte and leads to cell polarization.^[9,97] Das et al. studied cycled anodes' morphology with low and high sulfur-loaded cathodes and observed significant increase in Li dendrite growth and powdered Li formed on the separator with increased sulfur loading^[98] (Figure 4a). This has the dual effects of causing significant discharge polarization with LiPS accumulation and reducing the cell's Li inventory if the powdery Li breaks away from the current collector.^[91] Shi et al. discovered the formation of LiF-rich SEI in certain locations on the anode through X-ray photoelectron spectroscopy (XPS) analysis, indicating areas of higher and lower Li plating/stripping (Figure 4b).^[94] This is the result of Li pulverization and electrolyte saturation in some areas and under-utilization of active Li in other areas. Through multi-physics simulation, they revealed that under lean electrolyte conditions, excess electrolyte diffusion into areas of high electrolyte consumption becomes difficult due to high electrode tortuosity, leading to certain areas on both electrodes losing cycling capability after electrolyte depletion to side reactions. They proposed an improved cathode design targeting lower tortuosity to allow planar diffusion of the electrolyte according to its concentration gradient, as well as electrolyte stabilization strategies to prevent regional electrolyte over-consumption. Chen et al. also pinpointed nonuniform electrolyte distribution as the leading cause of cell failure; cycled anodes and cathodes were found to recover capacity and maintain good redox kinetics in fresh cells, ruling both electrodes' active material content and morphology out as failure

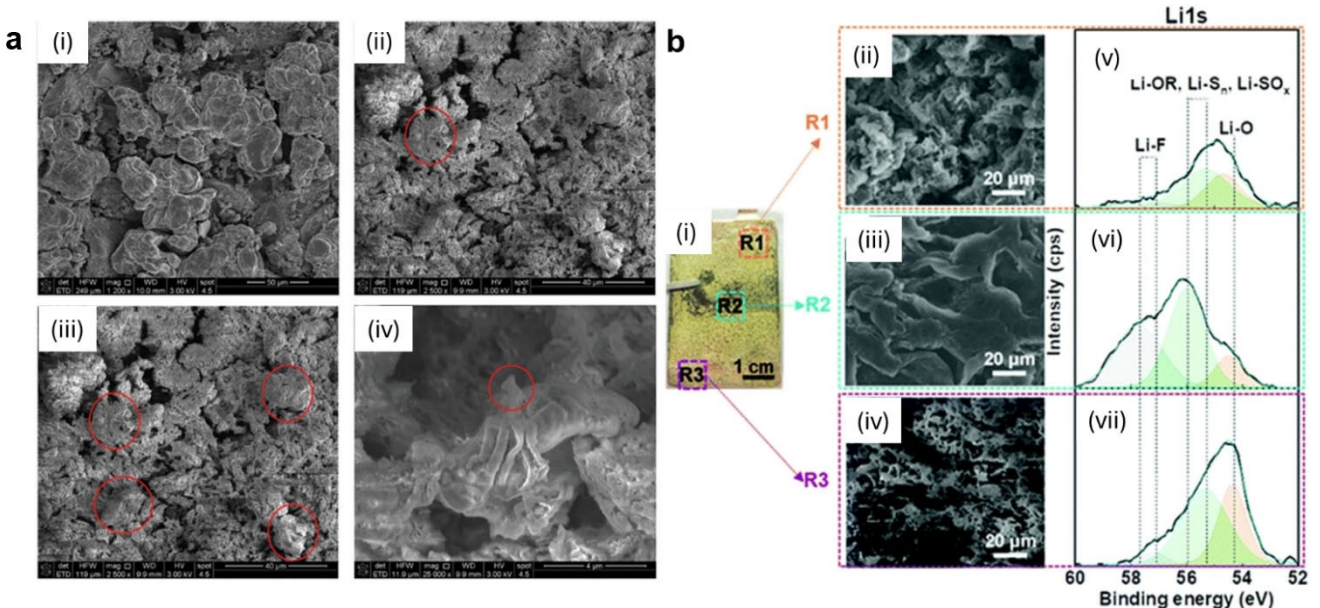


Figure 4. (a) SEM images of cycled Li anode from pouch cells with: (i, ii) 1.78 mg cm⁻² sulfur loading, (iii, iv) 3.5 mg cm⁻² sulfur loading. Reproduced under terms of the CC-BY 4.0 license.^[98] (b) SEM images and XPS spectra of three regions of cycled Li anode. (i) Photograph of Li anode showing three selected regions R1 (near electrode tab), R2 (center) and R3 (bottom corner of electrode), (ii, iii, iv) SEM images corresponding to R1, R2 and R3, (v, vi, vii) XPS spectra corresponding to R1, R2 and R3. Reproduced with permission.^[94] Copyright © 2020, Royal Society of Chemistry.

causes.^[99] Moreover, the addition of electrolyte to failed pouch cells led to recovered kinetics, shown through high discharge capacity and coulombic efficiency. Cheng et al. studied the failure of long-cycling pouch cells and observed continuously increasing resistance to Li⁺ diffusion, which they correlated with depleted electrolyte due to Li metal-electrolyte reactions.^[100] The increased polysulfide shuttle at high current density in pouch cells damaged the SEI layer and worsened the effect of these side reactions, ultimately leading to higher electrolyte viscosity and increased Li⁺ diffusion resistance as polysulfide buildup occurred at the anode. Recently, ultrasonic scanning techniques have emerged as non-destructive operando techniques to characterize electrolyte distribution in pouch cells.^[100] This technique is highly sensitive to the solid-air interface and can detect a single dry electrode layer, which can be useful in determining pressure applications during large cell fabrication.

Incorporating a conductive 3D framework for the anode that uniformizes current distribution has been suggested as a strategy to homogenize Li plating/stripping, suppress dendrite growth and recycle dead lithium back to the current collector.^[101] In liquid electrolytes, plastic deformation of the Li surface occurs under high current density and creates slip lines that induce preferential stripping of lithium.^[102] This can eventually lead to void formation along the grain boundaries and accumulation of disconnected lithium in the centers. Li et al. explored the changes in electrolyte diffusion and wetting with increasing external stack pressure through studying the ratio of porosity to tortuosity, aiming to address high volume change of Li anodes resulting from uneven Li accumulation/depletion.^[103] Their non-calendared sulfur cathodes showed high electrolyte wettability after a few cycles, corresponding to better electrolyte diffusion and accommodation of sulfur volume expansion, but promoted a porous anode structure with high SEI formation. High porosity and low tortuosity cathodes allow greater electrolyte diffusion; when combined with a high external pressure, this type of cathode is found to stabilize the Li anode by promoting a compressed anode morphology.^[91,104]

Cathode redox kinetics also suffer greatly from lean or unevenly distributed electrolyte conditions. This is especially true under the high working currents used by most pouch cells due to their high areal sulfur loading, which leads to huge cell polarization. Cheng et al. conducted polarization decoupling with failed cells after identifying uneven sulfur distribution on cycled cathodes and narrowed the failure cause down to cathodic polarization.^[105] They revealed the sharp increase in activation polarization at the beginning of the second discharge, associated with sluggish charge transfer kinetics. Activation polarization (η_{ac}) is identified as the dominant polarization at the Li₂S nucleation stage and is the key kinetic limiting factor under lean-electrolyte conditions. To address this, they validated the use of a redox mediator to react with soluble LiPS and form redox-promoting lithium organo-poly-sulfides, thereby favoring Li₂S deposition. Similarly, Capkova et al. conducted electrochemical impedance spectroscopy (EIS) studies on cycling pouch cells at various DoD and found

increasing charge transfer resistance with cell discharge, attributed to slower polysulfide reduction kinetics as well as increasing concentration of precipitated, insulating Li₂S on the cathode's surface.^[106] Incorporating kinetic promoters such as transition-metal sulfides,^[107] nitrides and carbides^[108] into the cathode as secondary sulfur hosts has been reported extensively as an effective strategy for reducing conversion energy barriers and increasing conductivity, which will be elaborated on in later sections. Beyond immobilized metal compounds, homogeneous catalysts within the scope of organic and inorganic electrolyte additives such as Yu et al.'s self-assembled Cu(II) complex have received recent interest.^[109] Attention must be focused on developing such additives that not only homogenize Li deposition, but also promote cathode-side polysulfide conversion and maintain Li⁺ diffusion dynamics.

2.2. Thermal Runaway Routes of Li–S Pouch Cells

Beyond electrochemical performance, this review considers the safety risks and thermal events within the scope of failure mechanisms, as these prevent the practical application of large-format Li–S cells in EVs and electronic devices. Lithium-sulfur cells utilize flammable Li metal and ether electrolyte solvents, are prone to dendrite growth and internal short-circuit, and form pyrophoric powdery lithium upon cycling, inviting serious potential safety hazards such as fire or explosion if thermal runaway is triggered.^[91,110] The thermal runaway behaviors of lithium-sulfur batteries have been systematically investigated in comparison to LIBs in several works by testing cells under abuse conditions and conducting calorimetric studies.^[110–112] Abuse testing of batteries typically involves three main tests: overcharge, overdischarge, and nail penetration. Meng's group documented uncontrolled SEI growth when overcharging Li–S cells through the decomposition of the DOL-LiTFSI electrolyte complex at 4.2 V.^[110] They describe three stages of overcharge behavior starting with ohmic polarization at the beginning of overcharge, which causes electrolyte oxidation and high deposition of lithium and electrolyte products on the anode (Figure 5). The electrolyte decomposition in turn generates heat and gas, which raises the temperature of the cell until the remaining liquid electrolyte begins to evaporate (~73 °C). This continues until the cell's internal pressure is too high and the packaging ruptures. The group describes a similar thermal runaway process occurring during nail penetration, which internally short-circuits the cell. The large amount of current passing through the penetrated region leads to rapid electrolyte evaporation and eventual cell rupture.

The separator is generally considered as the key component to develop to prevent thermal runaway through internal short-circuit.^[113] This can occur through mechanically suppressing Li dendrites or external penetration, improving thermal stability and diffusivity of separators at high temperatures/voltage, or engineering a "shut-off" mechanism that prevents temperature rise in the event of shorting.^[114] The baseline polyolefin separators used in most Li–S cells experience thermal shrinkage and deformation with modest cell heating (150 °C), which can

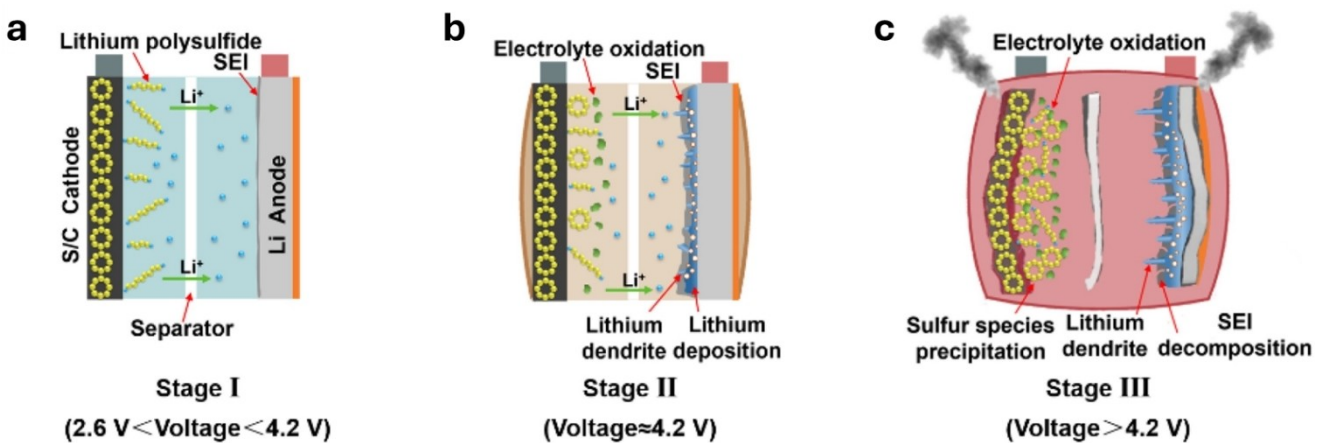


Figure 5. Schematic of thermal runaway of Li–S cells in three stages. (a) Stage I: ohmic polarization of the cell; (b) Stage II: electrolyte oxidation and uncontrolled SEI formation, temperature increase; (c) Stage III: electrolyte evaporation and cell rupture. Reproduced with permission.^[110] Copyright © 2020, Elsevier B.V.

cause them to collapse and internally short the cell.^[115] Heat-resistant ceramic-polymer composite coatings can lend mechanical and thermal support to PP and PE separators,^[116,117] although this can come with a trade-off in flexibility, wettability and cell resistance. Standalone organic composite separators with enhanced heat resistance have also been developed via electrospinning, phase inversion, and other techniques.^[118,119] However, there are few reports of scaled-up production of heat-resistant separators and testing in large cells, necessitating a look at the scalability of these methods.

A saving grace of Li–S cells compared to Li-ion batteries is that sulfur cathodes are oxygen-free, delaying cell combustion due to lack of fuel. Meng's group's works further advance the insulating nature of sulfur and Li₂S as thermal runaway inhibitors.^[110,111] During nail penetration, they observed an insulating layer of solid polysulfides on the nail which was thought to have deposited from dissolved LiPS during the large current response. This "insulating seal" layer of polysulfides reduces the cyclability of the cells but prevents thermal runaway by blocking electron transfer, which increases the safety of the cells. The ability of dissolved polysulfides to inhibit thermal runaway is further explored in Huang's group's research investigating pouch cells cycled to 16 and 45 cycles.^[120] The 45-cycle pouch cell experiences cell polarization and high concentration of dissolved lower-order (Li₂S_x, 4 ≤ x ≤ 6) LiPS, which thickens the electrolyte and worsens electrode-electrolyte contact and prevents thermal runaway-inducing Li anode-electrolyte reactions. In this way, Li–S cells experience a trade-off between cycling performance, which is limited by polysulfide dissolution, and safety in the event of thermal runaway.

2.3. Calendar Ageing Mechanisms of Pouch Cells

To bring Li–S technology on par with state-of-the-art LIBs, calendar ageing is an important parameter to study in large-format cells. Applications such as EVs require batteries to spend

the majority of their lives in a charged state and held at fixed voltage when in parking mode, and resting-phase performance degradation of batteries is a critical issue that has still not been fully examined.^[121] Real-world cycling protocols do not involve continuous cycles, and batteries typically charge and discharge repeatedly to different states of charge (SOC). Calendar ageing studies aim to elucidate the mechanisms of capacity loss outside of the charge-discharge processes, which are associated with cycling ageing. Phenomena such as electrode volume expansion, sluggish redox kinetics, and irreversible polysulfide deposition are related with cycling ageing of cells.^[122] By contrast, calendar ageing deals with corrosive or exhaustive side reactions related to materials' instability, which causes resistive interphase formation and self-discharge.

In liquid electrolyte systems, the reduction of the electrolyte and increased SEI formation are known to be the leading causes of capacity loss.^[123,124] In LIBs with graphite anodes, this passivation can be reduced through formation of a stable protective SEI layer in initial cycles and storing the battery under partially charged states. However, the continuous plating and stripping of lithium in lithium metal batteries (LMBs) renders fresh Li available to the electrolyte even during partial discharge steps.^[125] Li–S batteries especially are known to suffer from high self-discharge of >50% capacity fade per month, and the issue is exacerbated with high sulfur-loaded cathodes.^[126] Wood et al. developed a predictive model based on SEI composition information and concluded that capacity loss during calendar ageing is primarily controlled by chemical reactions between Li metal and ether electrolytes due to the high reactivity of lithium^[127] (Figure 6a–b). Cui's group's work also characterized the formed SEIs on Li metal after cycling compared to after calendar ageing through cryo-STEM electron energy loss spectroscopy to detect nanoscale heterogeneities.^[125] The preliminary compact SEI formed after aging in FEC:DEC electrolyte displays primarily salt-related peaks, but the extended SEI formed after aging consists of large clusters of organics from solvent decomposition and is thought

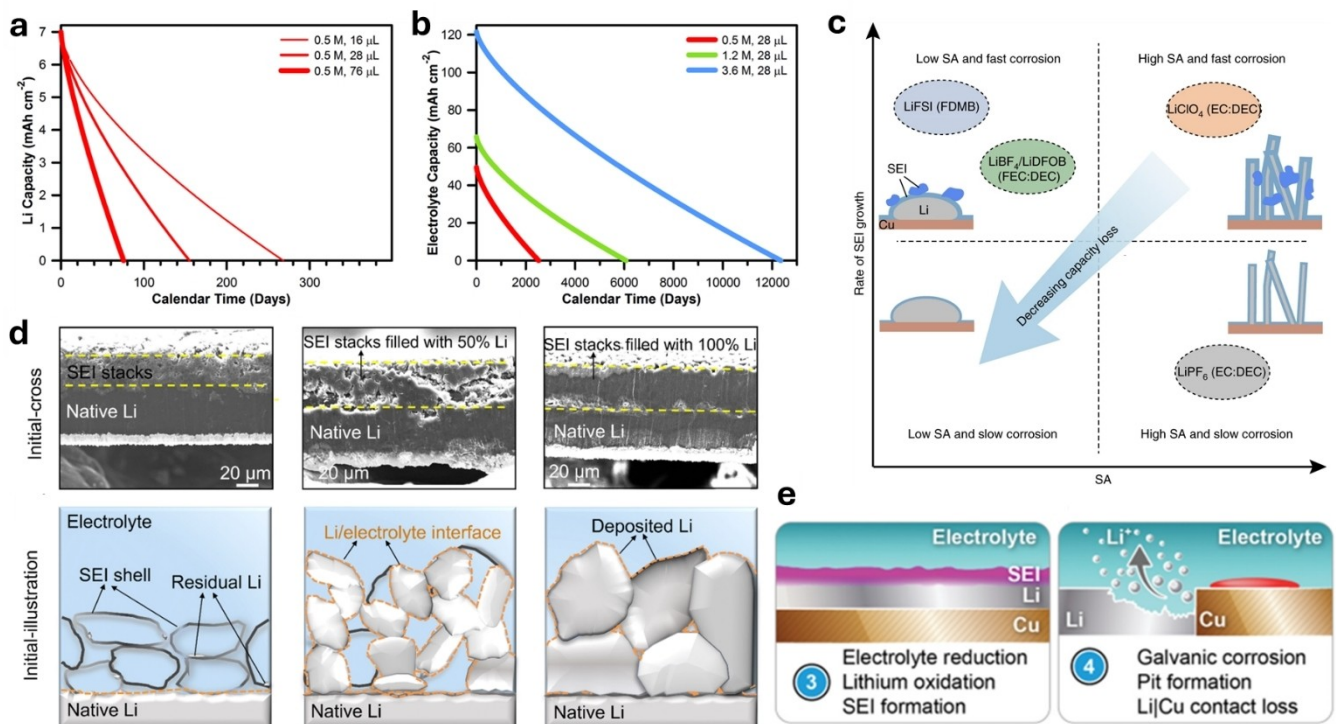


Figure 6. Effect of calendar ageing on (a) Li capacity (mAh cm^{-2}), (b) electrolyte capacity (mAh cm^{-2}). Reproduced with permission.^[127] Copyright © 2018, S. M. Wood et al., Wiley-VCH. (c) Schematic of the capacity loss of Li metal anodes with increasing Li surface area (SA) and SEI growth rate in different electrolyte chemistries. Reproduced with permission.^[125] Copyright © 2021, D. T. Boyle et al., Nature Energy 2021, published by Springer Nature. (d) Cross-section SEM images and schematic of Li deposition into SEI shells formed by orthoformate-based LHCEs at different SOC. Reproduced under terms of the CC-BY 4.0 license.^[129] (e) Schematic of galvanic Cu corrosion when exposed to electrolyte due to Li depletion. Reproduced under terms of the CC-BY 4.0 license.^[134]

to primarily contain carbonate-based polymers. Their group related coulombic efficiency loss after aging to the rate of growth of this SEI layer and the exposed lithium surface area, which vary in different electrolyte systems (Figure 6c). These works prove that Li anode surface protection and Li deposition control for stable morphology are critical methods of enhancing Li–S batteries' calendar life. Merrill et al. utilized a ZnO lithiophilic layer along with fluorosulfonyl-based salts to form a LiZn alloy, which promotes stable Li morphology and adhesion and reduces self-discharge.^[128] Cao et al. also demonstrated the principle of a reusable, robust SEI in the form of "shells" that guide Li deposition and dissolution with minimal structural changes, enabling 94% capacity retention after 100 cycles following an 18-month storage period^[129] (Figure 6d). The shells are formed by orthoformate-based LHCEs that enable anion decomposition into monolithic, mechanically strong SEI structures,^[130] which retain residual Li after stripping that helps to facilitate subsequent Li deposition in an engineered electronic passage. Atomic layer deposition (ALD) techniques for depositing thin and highly uniform Li-protecting aluminum oxide layers have also been shown to suppress self-discharge and promote dense Li plating in coin cells.^[131,132] The Al₂O₃-protected Li-electrolyte interface maintains high capacity and achieves long cycle life due to the absence of side reactions with polysulfides.^[133]

At low N/P ratio and lean electrolyte conditions, uncontrolled SEI formation during storage is an even greater problem

that leads to active material depletion and capacity fade, necessitating large-format evaluation and optimization of calendar aging performance. Capkova et al. carried out a shelf-life study in 3.4 Ah pouch cells at different SOC and observed the highest overall cell resistance in cells stored at discharged conditions (70–90% DOD).^[122] Storing the battery during the second voltage plateau resulted in the irreversible formation of a blocking layer on the cathode of short-chain polysulfides, which increases diffusion and charge-transfer resistance. Moreover, Li deposition and dissolution in practical LMBs occurs on the surface of a current collector, which introduces a new electrolyte-accessible material that provides pathways for corrosion. Copper is a commonly used current collector for LMBs due to its nonreactivity with Li during normal battery operation, but its higher oxidation potential can result in galvanic Li corrosion when both metals are exposed to oxidizing electrolyte^[134] (Figure 6e). Lin et al. observed fast galvanic corrosion of Li deposited on Cu surface, where the formation of an organics-rich SEI on the Cu surface causes electrolyte reduction coupled with Li oxidation.^[135] The oxidized Li forms dendrites and detaches from the Cu surface, while continuous electrolyte depletion occurs at the Cu-electrolyte interface. Galvanic corrosion is worsened at low Li/Cu ratio, as the Li anode is sacrificed to protect the current collector surface and corrodes at an accelerated rate.^[134] This phenomenon can be mitigated by improving Li deposition to provide superior inter-particle Li contact and uniform coverage of Cu, thereby

reducing the electrolyte exposure area. Passivation of the current collector through physically depositing thin film coatings^[132] or chemically forming anticorrosive layers^[136] has been reported to reduce galvanic corrosion and stabilize Li metal anodes. However, these methods are still being developed in coin cells and have not been validated at high areal loading, lean electrolyte conditions. It is also necessary to go beyond academic cycling protocols and conduct cycling and rest evaluations at different time periods and SOC to determine the states at which side reactions propagate and effectively mitigate the resulting performance decay.

3. Form Factors for Designing High-Energy Pouch Cells

Understanding the various failure mechanisms of practical pouch cells enables systematic development of form factors, or guidelines, to fabricating high-energy density pouch cells with long cycle life. Cell design ideally starts with selecting a target cell-level energy density and tuning the cell parameters accordingly, which can be done through developing a simple mathematical model of the energy density. The gravimetric energy density of the cell is briefly defined as the total energy of the cell divided by its total mass (m_{cell}). Considering the calculation of cell energy through multiplying the specific capacity of the cell's active material sulfur (C_s) by its mass (m_s), this can be written as follows:

$$\text{Energy density} = \frac{C_s * V * m_s}{m_{cell}} \quad (1)$$

where V is the cell's voltage (~2.1 V) and m_{cell} is the total mass of the cell. The specific capacity (C_s) of the cell's sulfur can be understood as the sulfur utilization rate, U_s , multiplied by the theoretical capacity of sulfur ($C_{s,\text{theo}}$). The sulfur utilization rate is a parameter that quantifies the effectiveness with which the cell's sulfur is extracted and used.

The cell's total mass is expanded in Equation (2):

$$m_{cell} = m_{cathode} + m_{anode} + m_{electrolyte} + m_{inactive} \quad (2)$$

Here, $m_{cathode}$ is the mass of the cathode, m_{anode} is the mass of the anode, $m_{electrolyte}$ is the mass of the electrolyte, and $m_{inactive}$ is comprised of the mass of the separator, current collectors, and packaging materials.

By combining these equations and dividing m_s out, a more detailed equation for energy density can be formulated in terms of the sulfur fraction in the cathode (ω_s), electrolyte-to-sulfur ratio ($r_{E/S}$), negative-to-positive electrode ratio ($r_{N/P}$), and areal sulfur loading (L_s) as shown in Equation (3).

$$\text{Energy density} = \frac{C_{s,\text{theo}} * U_s * V}{\frac{1}{\omega_s} + r_{N/P} + r_{E/S} * \rho_{elec} + \frac{L_{cc}/2 + L_{sep}}{L_s} + \frac{L_{packaging}}{2N * L_s}} \quad (3)$$

Here, ρ_{elec} is the density of the electrolyte, L_{cc} is the sum of the areal densities of the current collectors, L_{sep} is the areal density of the separator, and $L_{packaging}$ is the areal density of the packaging materials. Along with V and $C_{s,\text{theo}}$, all of these parameters can be taken as constant values for a given facility.^[92] Thus, the key parameters to tune for increased energy density are the sulfur utilization (U_s), the sulfur fraction in the cathode (ω_s), areal sulfur loading (L_s), the E/S ratio ($r_{E/S}$), and the N/P ratio ($r_{N/P}$). Strategies to increase cell performance that involve the addition of inactive materials as polysulfide-trapping frameworks or catalysts must also focus on reducing the weight of inactive materials to minimize cell weight.

3.1. Cathode Design for High Energy Density

Cathode design is widely considered to be a key part of cell design to maximize cell energy while reducing the mass of inactive material. Conventional cathodes must incorporate conductive carbon additives and binder along with sulfur to achieve reversible cycling. Overly maximizing the amount of sulfur or minimizing the weight of the inactive components comes with significant tradeoff in cell performance if the cathode fails to achieve high sulfur utilization.^[92] Increasing the sulfur content in the cell without efficient utilization will negatively impact the energy density as some of the sulfur mass would essentially be inactive. Mathematical modeling of the energy density according to Equation (3) reveals that energy density does not increase linearly with areal sulfur loading, instead tapering off around 8–10 mg cm⁻², as seen in Figure 7. Moreover, while the weight of inactive cathode materials is only a small fraction of the cell weight, increasing sulfur beyond its practical utilization necessitates higher weights of anode and electrolyte materials to match, which has a much greater impact on the cell weight. Thus, while sulfur content in the cathode is an important parameter, overly high (> 90 wt%) sulfur content or ultrahigh areal loading (> 9 mg cm⁻²) is generally not practical.

Achieving areal sulfur loadings of 6–9 mg cm⁻² with porous and wettable cathodes that have high conductivity is a challenging task, even before taking catalytic additives into account. A common strategy for achieving high areal sulfur loading is to increase the thickness of the cathode coating.^[137] This enables a lower electrolyte to cathode ratio with the same contact area and reduces the weight of inactive components such as the current collector. However, engineering thick sulfur cathodes requires an entirely new cathode architecture that accounts for increased polysulfide shuttling due to the high sulfur concentration. From a mechanical perspective, thick cathodes have a higher tendency towards cracking or delamination from the substrate. Lu et al. also observed lowered initial capacity due to slow wetting of thick cathodes over the first few cycles.^[138] The areal capacity of their thick cathode, which increases with sulfur content at low areal sulfur loadings, also plateaus when loaded with > 3.5 mg cm⁻² sulfur due to the poor ionic and electronic conductivity caused by sulfur's insulating nature and poor utilization of sulfur.

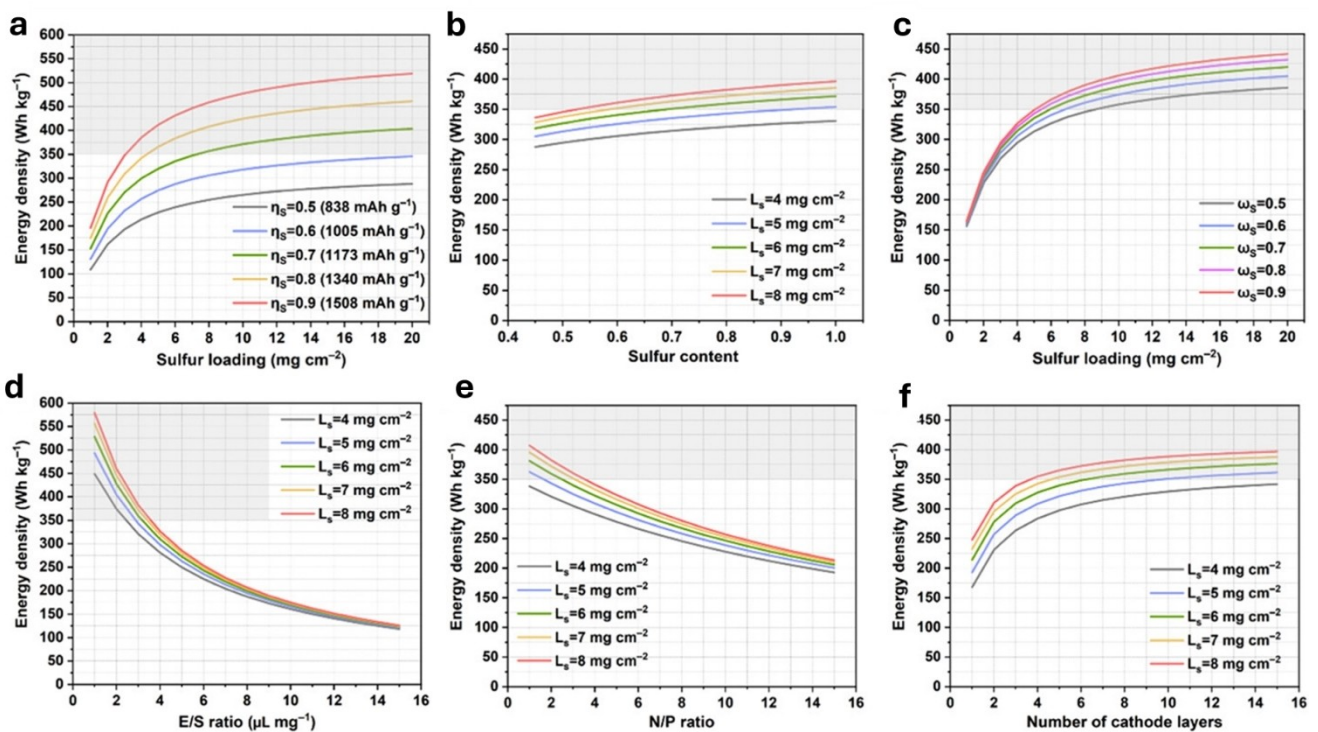


Figure 7. Projected energy density of Li-S pouch cells when varying: (a) Sulfur loading and sulfur utilization (η_s), (b) Sulfur content and sulfur loading (L_s), (c) Sulfur loading and sulfur content (ω_s), (d) E/S ratio and sulfur loading (L_s), (e) N/P ratio and sulfur loading (L_s), (f) Number of cathode layers and sulfur loading (L_s). Reproduced under terms of the CC-BY 4.0 license.^[92]

Rational design of thick cathodes can remedy this with the addition of porous carbon materials such as multiwall carbon nanotubes (CNT) or graphene.^[138] Sulfur is typically impregnated into the capillaries of such a highly porous host carbon material, which can reduce LiPS dissolution, enhance ion diffusion and increase sulfur utilization through maximizing electrolyte uptake and diffusion into the cathode pores. The importance of tuning porosity to achieve high sulfur loading and utilization cannot be understated. Voluminous carbons with high pore fraction provide mechanical integrity when volume expansion of sulfur occurs, which can be up to 8 times that of a typical Li-ion electrode.^[139] The high surface area of such porous carbons also provides more reaction sites, corresponding to increased sulfur utilization and capacity. Kang et al. pointed out that loss of pore surface area in lower porosity cathodes corresponded to a lowered second discharge plateau, which corresponds to the precipitation of $\text{Li}_2\text{S}_2/\text{Li}_2\text{S}$.^[140] Reducing the porosity reduces the reaction sites for this deposition, which affects the discharge capacity (Figure 8a-b). Furthermore, due to poor dissolution of polysulfides at low porosity, the sulfur utilization rate is also reduced (Figure 8c). However, their study also concludes that porosity is not a one-dimensional parameter—too much free space in the cathode reduces the volumetric energy density and necessitates a high E/S ratio to fully wet the cathode, which also impacts the gravimetric energy density (Figure 8d). They achieved an 18% reduction in electrolyte when reducing the cathode porosity to 50% and concluded

that 50–60% porosity is optimal for high sulfur loading (5–6 mg cm⁻²) cathodes.

The drive to control porosity and develop efficient pore architectures has recently inspired several studies on 3D interconnected porous cathodes, which can provide multidimensional ion and electron transfer pathways with shorter diffusion length.^[141] Cheng et al. developed a multifunctional 3D nitrogen-doped graphene which exhibited a hierarchical pore structure with mechanically stabilizing graphitic structures that helped to confine polysulfides, facilitated ion transfer and enabled high sulfur utilization.^[142] Hierarchically porous cathodes that have multiple levels of porosity (micropores, mesopores and macropores) have also received much interest as frameworks for sulfur containment.^[143,144] Mesopores (2–50 nm) and micropores (<2 nm) with high specific surface area provide active sites for reaction, which helps to mitigate polysulfide dissolution by ensuring that the SRR takes place in specific locations to and from which Li^+ diffusion occurs.^[145] The addition of macropores (>50 nm) enables high sulfur loading and provides void space for sulfur's volume expansion to help the microporous structures retain mechanical integrity. Macropores also provide sites for incorporating catalytic nanoparticles or other conductive additives.^[29]

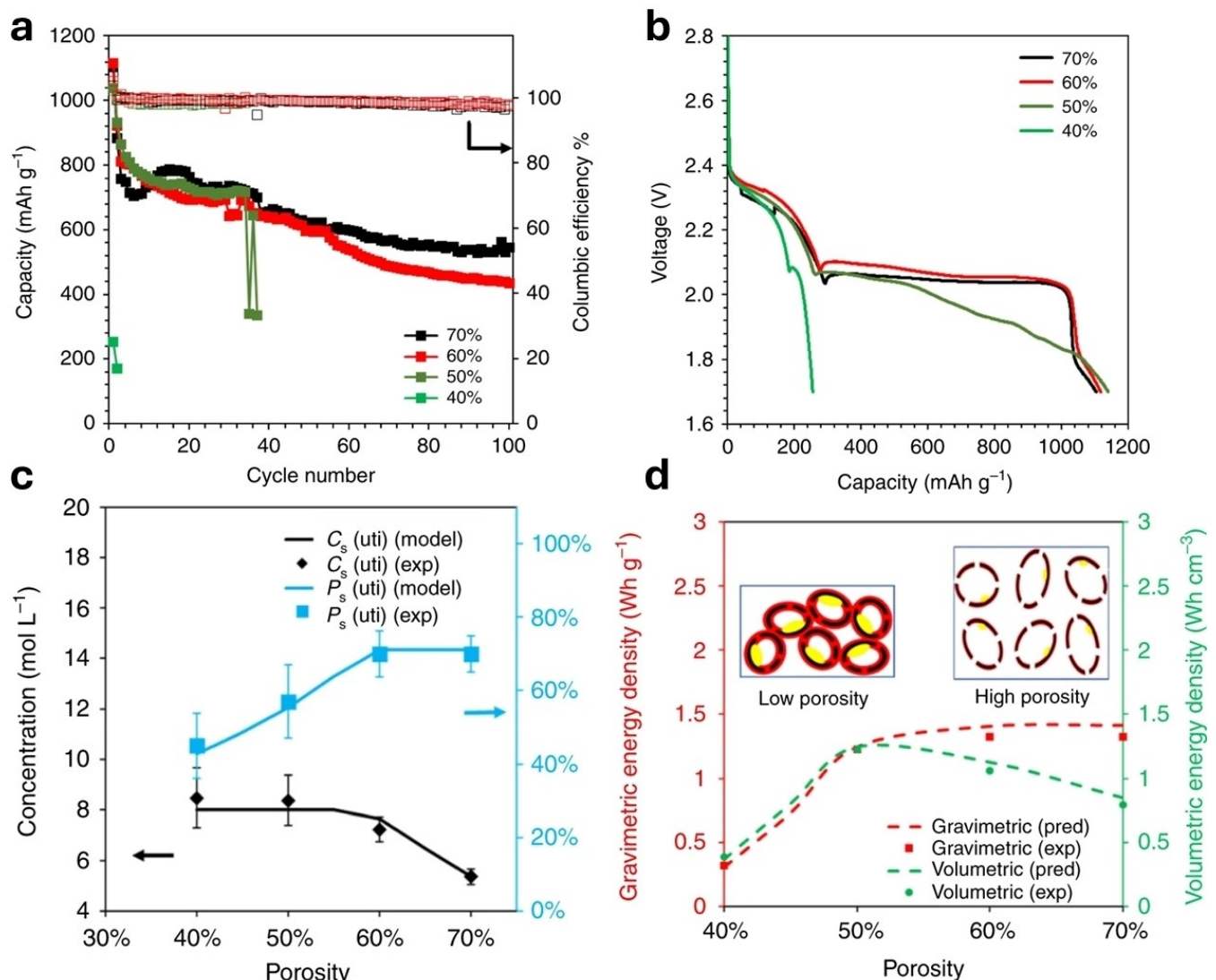


Figure 8. Effect of varying cathode porosity (40–70%) on various cell parameters. Electrochemical performance in coin cells at sulfur mass loading of 5 mg cm⁻², (a) Discharge capacity, cycle life and coulombic efficiency, (b) Discharge profiles. Analytical modeling predictions and experimental results, (c) LiPS concentration (C_s (uti)) and sulfur utilization rate (P_s (uti)) as a function of porosity, (d) Gravimetric and volumetric energy densities based on total cathode mass or cathode volume as a function of porosity. Reproduced under terms of the CC-BY 4.0 license.^[140]

3.2. Importance of Low Electrolyte-to-Sulfur Ratio

The liquid electrolyte plays a large role in the cyclability of liquid Li–S cells, and is also responsible for Li⁺ ion diffusion, dissolving polysulfides and facilitating liquid-phase redox reactions. The rationale for adding electrolyte proportional to the amount of sulfur in the cell comes from the need of electrolyte to access embedded sulfur and propagate the sulfur reduction reactions, resulting in the commonly used parameter of electrolyte-to-sulfur ratio (E/S). However, excess electrolyte is a high contributor to cell weight in practical pouch cells, which significantly reduces the energy density of this system (Figure 7d). Studies report that electrolyte can comprise anywhere from 47%^[92]–58%^[146] of the total cell weight, meaning that reducing this ratio can significantly improve, or even almost double the energy density. Cui's group offers a valuable

framework for understanding the importance of the E/S ratio in Li–S batteries.^[8] They break down the energy density calculation into two components: cell weight and cell energy, analyzing the impact of these parameters separately. Their findings indicate that reducing the N/P ratio and E/S ratio has the most significant effect on increasing the mass percentage of active components, compared to merely increasing the overall cathode mass. For instance, when the N/P ratio is set at 2 and the E/S ratio is reduced from 2–1 $\mu\text{L mg}^{-1}$, the active material mass percentage increases from 28.6%–39.4%—a substantial improvement. Moreover, mathematical models of Li–S cells consistently show that achieving 500 Wh kg⁻¹ in pouch cells requires reducing the E/S ratio below 3 $\mu\text{L mg}^{-1}$. This reduction in electrolyte amount is thus essential for optimizing the energy density and advancing the practical application of Li–S batteries.^[8,92,147]

The detrimental effects of lean electrolyte conditions are primarily on the cathode side. Porous carbon hosts often require excess electrolyte for complete wetting and sulfur utilization, so lower electrolyte amounts directly reduce the electroactive surface area by isolating sulfur deposits, leading to lowered capacity and reduced cycle life.^[148] Secondly, reducing the electrolyte amount limits the quantity of dissolved LiPS and slows down the sulfur conversion reactions, leading to greater concentration of LiPS and higher viscosity, which reduces the ionic conductivity.^[43,149] Increased polysulfide concentration in the electrolyte worsens the shuttle effect and increases the parasitic LiPS-anode reactions as well. At practical charging rates, the accessible sulfur cannot be converted fast enough due to the sluggish kinetics, leading to the accumulation of "dead" sulfur on the cathode surface. Alongside, high concentrations of liquid-phase LiPS can also passivate the cathode through nonuniform and uncontrolled deposition of insulating $\text{Li}_2\text{S}/\text{Li}_2\text{S}_2$, which blocks the ion transfer channels of the porous host.^[150,151] All of these factors combine to limit the cycle life of practical lean electrolyte pouch cells to a relatively short period of less than 120 cycles.^[4,8]

The self-discharge behavior of Li–S cells is also significantly influenced by the E/S ratio.^[152–154] Shen et al. discovered that low E/S ratios enhance electrode surface protection and capacity recovery during resting periods.^[153] They found that the high concentration of liquid LiPS in low E/S conditions initiates the nucleation process of Li_2S "seeds" during resting, which then act as adsorption centers for Li_2S precipitation during discharge (Figure 9c). This mechanism allows for capacity recovery by regulating Li_2S deposition, mitigating capacity losses due to a passivated cathode surface. In contrast, high E/S ratios, with their low concentration of dissolved LiPS, do not facilitate seed nucleation, leaving cathode passivation unaffected (Figure 9a–b).

In the event of continuous cycling, controlling polysulfide dissolution and homogenizing redox reactions under lean electrolyte conditions are critical for both the cathode and electrolyte. High-DN solvents interact more effectively with Li^+ ions and can dissolve higher concentrations of liquid LiPS, which enhances sulfur utilization.^[155] Chu et al. also reported the use of high-DN salt anions (such as Br^- , CF_3SO_3^-) to modulate the morphology of deposited Li_2S and promote partial solubility

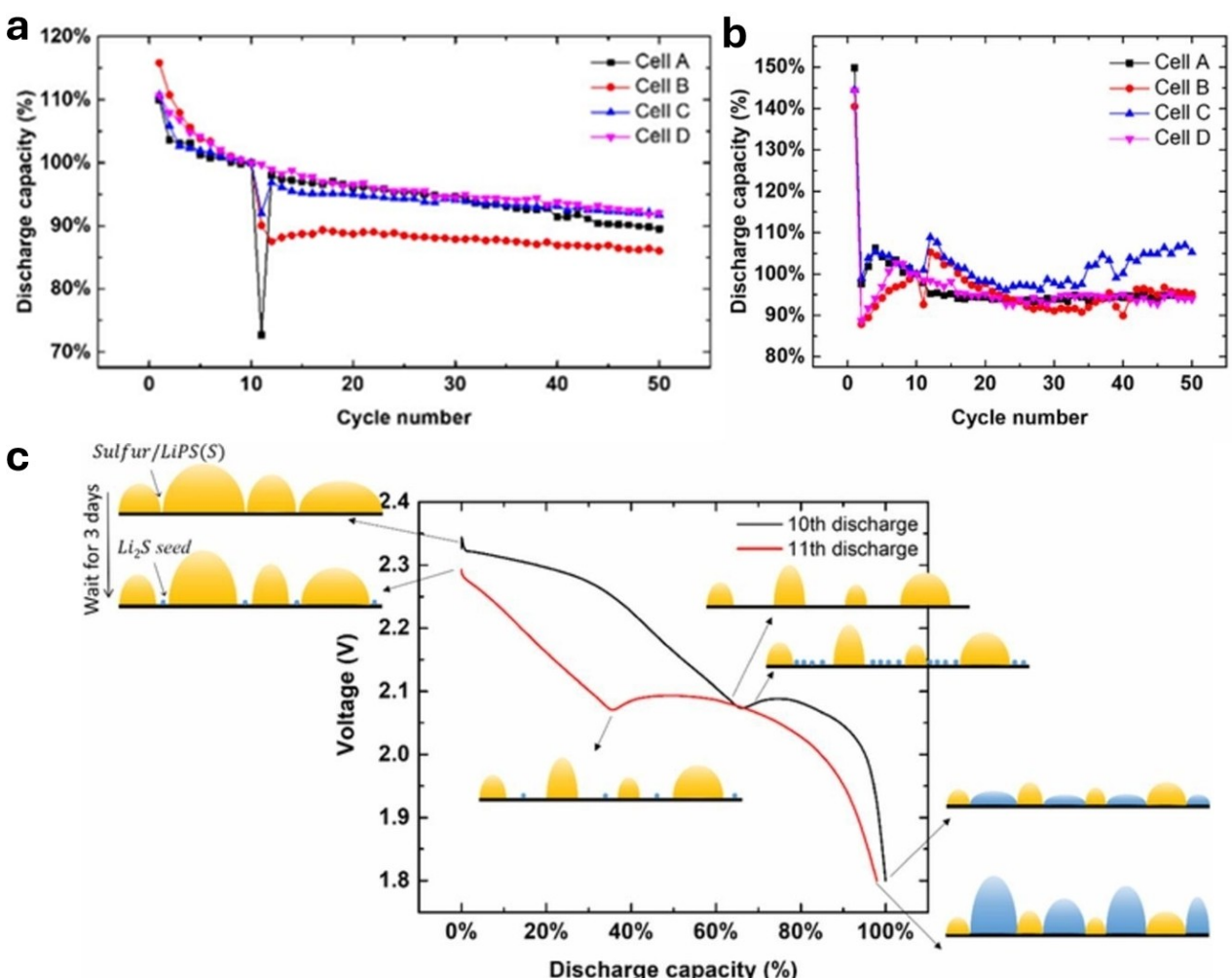


Figure 9. Self-discharge evaluation (between cycles 10 and 11) of Li–S pouch cells at different E/S ratios. (a) Self-discharge performance of cells with $E/S = 16 \mu\text{L mg}^{-1}$, (b) self-discharge performance of cells with $E/S = 5 \mu\text{L mg}^{-1}$, (c) Schematic of Li_2S seeds nucleation and Li_2S precipitation at low E/S ratio. Reproduced under terms of the CC-BY 4.0 license.^[153]

of Li_2S .^[156] These anions, with low dissociation energies, compete effectively with S^{2-} for binding to Li^+ ion, increasing Li_2S solubility. This process enhances the affinity of dissolved Li_2S for adsorbing onto precipitated Li_2S , which 3D Li_2S agglomerates and prevents surface passivation, giving an advantage over lower-DN salts like LiTFSI. Conversely, another strategy to manage high LiPS concentration is to use sparingly solvating electrolytes that reduce polysulfide solubility and transform the conversion pathways into “quasi-solid-state” reactions.^[151] Nazar’s group proposed that maintaining a smaller fraction of dissolved polysulfides (<3%) mitigates polysulfide shuttling while still enabling liquid-phase disproportionation reactions, which are preferable to the high cell polarization caused by entirely solid-state operation.^[157] Their diglyme-based electrolyte exhibited late-stage sulfur consumption and early reformation during discharge-charge, suggesting a single-plateau conversion model due to the different energetics of quasi-solid-state reaction.

3.3. Importance of Negative-to-Positive Electrode Ratio

Lithium metal has a high theoretical capacity of 3860 mAh g^{-1} , which theoretically enhances the energy density of LMBs due to the minimal amount of anode material required. Li–S cell models, such as the one depicted in Figure 7d, indicate that the cell-level energy density increases sharply when the N/P ratio is reduced below 6. It is commonly found that to reach 500 Wh kg^{-1} , an N/P ratio of 2 at the highest is required. In an ideal Li–S configuration, a stoichiometrically equal amount of lithium and sulfur would be sufficient to achieve the highest theoretical capacity, resulting in an N/P ratio of 1. However, practical Li–S pouch cells always use an excess of Li metal to compensate for significant losses during cycling due to higher currents and Li loss. Anode failure mechanisms such as dendrite growth, parasitic side reactions, anode corrosion and formation of dead Li deplete the cell’s active material, making it necessary to use an excess of lithium. The cycle life of pouch cells almost always suffers from curtailing the lithium amount, although lithium excess does not directly contribute to increased cell longevity.^[4] Consequently, most coin cells have an N/P ratio greater than 100, with thick Li anodes ($> 100 \mu\text{m}$), to provide an optimal testing environment.

Achieving low N/P ratio in pouch cells is also dependent on the thickness of the Li anode when the cathode areal capacity is fixed. Pouch cells typically contain the same number of anode and cathode layers, so reducing the N/P ratio necessitates the use of thin lithium foils. The industrial process for thin lithium foil production involves hydraulic extrusion and rolling, which becomes challenging and highly expensive when the lithium thickness is reduced below $20 \mu\text{m}$.^[158] Additionally, the Li surface is prone to damage during production or handling, potentially altering the crystallographic orientation of the lithium or introducing impurities.^[102] Moreover, the copper current collector has a high density of 8.9 g cm^{-3} compared to 0.534 g cm^{-3} for Li. As the Li thickness decreases, the copper current collector contributes a significantly higher (up to 75%)

percentage of the cell weight.^[97] Therefore, other factors such as increasing Li utilization, protecting the Li from corrosion, and exploring different Li host and current collector materials become crucial for maximizing cell energy density when using the lowest practical Li thickness.

4. General Approaches to Optimize SRR Kinetics for Li–S Batteries

4.1. Sulfur Host Materials with Heteroatom Catalysis

In the preceding sections, the failure mechanisms and the key form factors of Li–S pouch cells were discussed. Beyond the well-known polysulfide shuttling effect, which arises from the high solubility of certain lithium polysulfides, another significant challenge hindering the application of Li–S batteries is the sluggish kinetics associated with polysulfide conversion. During the conversion process, polysulfides undergo phase changes from liquid to solid, and insoluble polysulfides such as Li_2S_2 undergo solid-to-solid transformations, further impeding the conversion. Consequently, the polysulfide shuttling effect is exacerbated due to the prolonged presence of long-chain polysulfides, which detrimentally affects the battery’s cycling performance and lifespan. Several reviews have comprehensively discussed the principles of heterostructures and cathode design to accelerate lithium polysulfides conversion and minimize polysulfide shuttling by anchoring lithium polysulfides.^[72,159–162]

Given the significant challenges, considerable efforts have been devoted to mitigating these issues, broadly categorized into two main strategies: rational design of the sulfur host and optimization of the electrolyte.^[163–167] The first strategy involves the use of carbonaceous hosts, such as carbon capsules,^[168] carbon nanotubes,^[169] carbon nanofibers,^[170–172] graphene nanosheets,^[173–176] and porous graphitic carbon.^[163,177,178] These materials enhance electron transfer and physically absorb dissolved polysulfides, preventing their migration. However, carbon-based hosts suffer from the weak Van der Waals interactions between non-polar carbon and polar polysulfides, which makes them less effective in curbing polysulfide shuttling during prolonged cycling.^[176,179–181] To address this limitation, chemical polysulfide entrapment methods with catalytic acceleration have been introduced. These methods fall into two main categories: heteroatom co-doping and catalyst/heteroatom doping composites. Examples include modifying carbonaceous materials with heteroatoms such as N, O, P, S, Fe, and Co, or surface functionalization with –OH or –O– groups.^[163,171,182] Another approach involves creating ionic-electronic cooperative catalytic heterointerfaces using polar compounds like metal nitrides, oxides, sulfides, alloys, and MXenes.^[17,183–186] These techniques enhance the catalytic activity by regulating the electronic structure, thereby inhibiting the shuttle effect. Adjusting the d/p-band center, e_g -orbital electron filling, or spin electrons of electrocatalysts strengthens polysulfide adsorption ability, enhances catalytic activity, and enables high areal sulfur

loading.^[187–193] The cathode engineering focuses on polysulfide immobilization and conversion to enhance SRR kinetics, facilitating the fabrication of high energy Li–S cells.

Carbonaceous materials are extensively used as substrates for creating heterostructures in Li–S batteries due to their superior electrical conductivity, high specific surface area, and robust mechanical properties. Although porous and high surface area carbonaceous materials are frequently utilized as sulfur hosts in Li–S batteries, their weak interaction with polar polysulfides sometimes fails to effectively inhibit the dissolution and shuttling effect of LiPSs. To address this issue, these carbon-based heterostructures consist of hybrid materials that integrate carbonaceous conductive materials with single metals or metallic compounds.^[194–197] For example, Huang et al. recently employed a ZnTe/CoTe₂@NC host material containing tellurium vacancies to enhance the adsorption of LiPSs.^[198] By leveraging heterojunction engineering between ZnTe and CoTe₂, the interface of these two transition metal compounds forms rich phase boundaries, charge accumulation/depletion regions, and electronic band bending. These unique features promote the diffusion of ions and electrons, optimizing electronic properties and facilitating ion and electron transport, thereby enhancing the performance of the lithium-sulfur battery. The material is also annealed under a reducing atmosphere to generate tellurium vacancies, which further enhances the adsorption of LiPSs and catalytic activity. The structure and composition of the material were analyzed using X-ray diffraction (XRD) and XPS, while its electrical conductivity was measured using the four-point probe method. The results showed that the heterostructured transition metal telluride (TMT) promotes ion diffusion and increases electrical conductivity. Additionally, the density of states (DOS) analysis and Bader charge analysis provided further insights into the charge transfer and catalytic properties of the material. Consequently, the v-ZnTe/CoTe₂@NC/S sulfur cathodes exhibited excellent initial capacities up to 1608 mAh g⁻¹ at 0.1 C and demonstrated stable cycling with an average capacity decay rate of only 0.022% per cycle at 1 C over 500 cycles in coin cells. The pouch cells assembled with v-ZnTe/CoTe₂@NC/S cathodes retained 86.78% of their capacity after 150 cycles (0.1 C) at a sulfur loading of 5.6 mg cm⁻² and 11.2 mL g⁻¹ electrolyte. Furthermore, when the sulfur load was increased to 6.4 and 8.2 mg cm⁻² at pouch cell level, the capacity retention was 77.6% and 75.4% after 100 cycles.

Other 2D polar transition metal carbides and nitrides, such as MXenes with surface functional groups like –OH, –O, or –F, offer an effective method to immobilize LiPSs and thereby extend the battery's lifespan.^[108,199,200] The porous design of MXene nanosheets, such as Ti₃C₂ MXene, addresses the long-standing issues of restacking and aggregation, simultaneously adjusting sulfur conversion and Li-ion flux in Li–S batteries.^[201] Chen et al. developed a dual-functional V₂C MXene as a sulfur host material by etching a commercial V₂AIC precursor with LiF/HCl.^[108] This approach enhances sulfur evolution kinetics and regulates Li-ion sieving behavior. The VC spheres formed in this process offer increased specific surface area, providing more active sites for tuning the Li–S redox reaction. Additionally, the

high-density channel structure created by the stacking of smaller VC spheres ensures a more uniform Li-ion flux, as demonstrated by COMSOL simulations. This unique scale effect allows VC spheres to optimize both sulfur conversion kinetics and Li stripping/plating behavior, leading to an outstanding initial discharge capacity and excellent cycling stability in the optimized Li–S battery. To assess the electrocatalytic activity of the VC spheres for the sulfur redox reaction, the researchers conducted cyclic voltammetry (CV) and linear sweep voltammetry (LSV) measurements. They also employed potentiostatic discharge and charge techniques to analyze the nucleation and dissociation reactions of Li₂S. Furthermore, synchrotron X-ray 3D nano-computed tomography (X-ray 3D nano-CT) was used to investigate the spatial distribution and morphology of precipitated Li₂S within the VC architectures (Figure 10). These comprehensive characterization methods enabled the researchers to evaluate the scale effect-triggered activity changes and the role of VC in regulating the redox kinetics of lithium polysulfides.

Zhao et al. proposed a cathode design to enable a high-energy and long-cycling Li–S pouch cell by uniformly embedding polar ZnS nanoparticles and Co–N–C SAC double-end binding sites into a highly oriented macroporous conductive framework as a catalytic S host to effectively immobilize polysulfide intermediates during cycling and minimize the shuttle effect.^[202] They demonstrated a 1 Ah pouch cell with low E/S ratio of 2.5 μL mg⁻¹ showing good cycling stability with Coulombic efficiency >95% for 80 cycles. Lee and coworkers proposed an advanced cathode comprising a highly active Fe–N–C catalysts to manipulate their local environment to achieve high-energy Li–S pouch cells.^[203] The introduction of thiophene-like-S (–S) and oxidized-S (–SO₂) electron-exchangeable binding (EEB) sites adjacent to Fe–N–C improves the lithium polysulfides adsorption and enhances the kinetics. These two different types of S species show different polysulfide adsorption behaviors. The group successfully fabricated and demonstrated a high-energy Li–S pouch cell with a 320.2 Wh kg⁻¹ energy density using low E/S (3.0 μL mg⁻¹), and N/P (2.3) ratios. Li et al. developed a highly efficient Li–S catalyst of V-doped CoSe₂ (single-phase Co_{0.9}V_{0.1}Se₂) and demonstrates higher activity for polysulfide conversion with a strong interaction between polysulfides and Co_{0.9}V_{0.1}Se₂.^[204] They successfully fabricated a large pouch cell with four cathodes and five anodes and demonstrated a cathode capacity of 700 mAh/g and cell which cycled 70 times with a capacity retention of 65.7%. All these studies demonstrate the current trend and effectiveness of using single-atom catalysts and hetero-catalyst designs to accelerate sulfur reduction kinetics.

4.2. Electrolyte Design for Lithium Metal Anode Protection

The second strategy to address polysulfide shuttling and anode corrosion focuses on electrolyte design.^[67,205–209] Various electrolyte additives, such as polymerizable additives,^[210] organometallic salt,^[211] and organosulfur,^[212] have been used to suppress the polysulfide shuttling effect by catalytically improv-

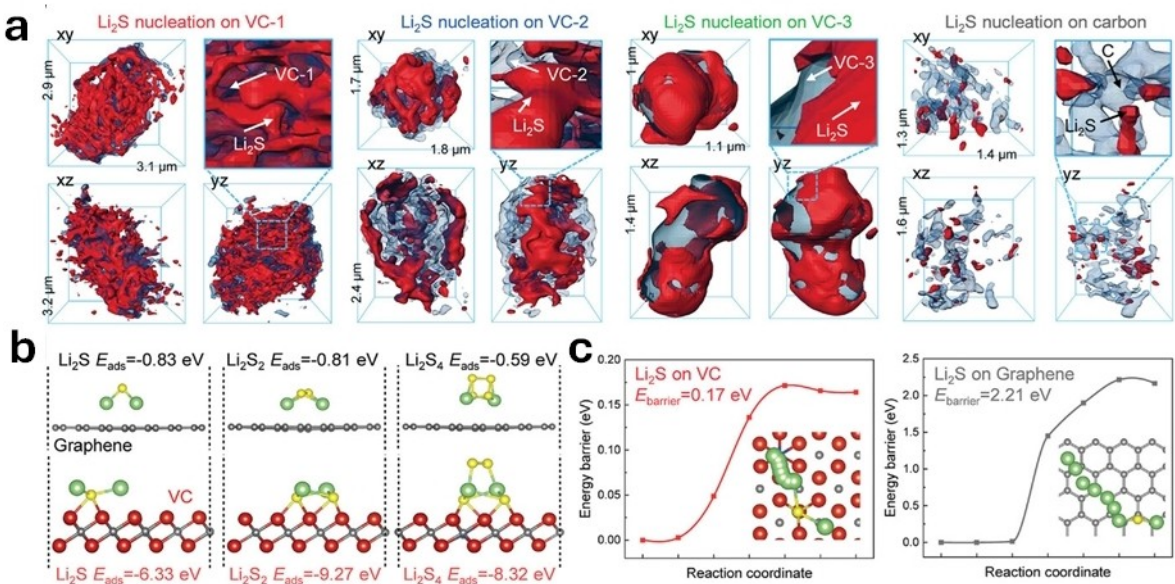


Figure 10. (a) Synchrotron X-ray 3D nano-CT images of electrochemically deposited Li₂S on various VC MXene substrates. (b) Adsorption energies and corresponding configurations for Li₂S, Li₂S₂, and Li₂S₄ on VC and graphene. (c) Dissociation barriers and pathways for Li₂S clusters on VC MXene and graphene. Reproduced with permission.^[108] Copyright © 2023, L. Chen et al., Wiley-VCH.

ing Li₂S deposition. However, the effectiveness of low-concentration additives, particularly in systems with lean electrolytes (low E/S ratio), remains debated.^[95,213–215] Consequently, the use of co-solvents with ether-based electrolytes has been proposed to modify the solvation structure of lithium ions and polysulfides.^[16,216–218] Fluorinated co-solvents like hydrofluoroether (HFE),^[63,219] di-isopropyl sulfide (DIPS),^[220] hexyl methyl ether (HME)^[221] or fluorinated-1,2-diethoxyethane (F4DEE)^[222] regulate the solvating power of polysulfides and improve the kinetics of polysulfide conversion.^[63,219] Electrolyte design focuses on creating LHCE and lean electrolytes, both of which have been shown to enhance capacity retention and lifespan.^[95,215,223–227] SEI engineering through electrolyte additives and the use of sparingly solvating electrolytes to minimize lithium polysulfide dissolution are also discussed as avenues for anode protection. While sulfur host strategies primarily aim to immobilize lithium polysulfides and accelerate their conversion, electrolyte strategies focus on encapsulating polysulfides and suppressing parasitic reactions at the anode.^[228–230] These advanced techniques significantly suppress polysulfide migration and anode corrosion, and their scalability and applicability to pouch cell configurations highlight the potential for Li–S battery commercialization.

4.2.1. Electrolyte Design with Additives and Cosolvents

To enhance the discharge capacity, rate capability, and reversibility of Li–S batteries, various techniques have been developed, including the use of electrolyte additives to regulate Li₂S deposition.^[231–233] Significantly, modifying the electrolyte composition to manage the solvent coordination structure can effectively control LiPS speciation and conversion, impacting

the Li₂S deposition process and morphology.^[155,207] Meng et al. proposed the use of quaternary ammonium salt (QAS) electrolyte additives in Li–S batteries.^[234] The T3⁺/T4⁺ cations and high-DN halogen Br[−]/Cl[−] anions in QAS can trigger and stabilize the formation of S₃^{·−} radical intermediates, thereby enhancing polysulfide conversion kinetics and promoting growth of Li₂S. This improvement results in better reversibility and sulfur utilization. Additionally, the cationic surfactant nature of QAS additives helps suppress lithium dendrite growth, while the higher lowest unoccupied molecular orbital (LUMO) value of QAS compared to LiTFSI alters the solvation structure of Li⁺, increasing the LiF content and enhancing compatibility with the lithium metal anode (Figure 11a–d). The competition between the dissociation of Li₂S₆ to Li₂S₄ and the formation of S₃^{·−} radicals in the T3Br electrolyte leads to a lower concentration of S₃^{·−} radicals compared to the T4Br electrolyte, although the S₃^{·−} concentration is still significantly higher than in the baseline electrolyte. To further analyze the chemical composition and bonding states of the SEI layer on the lithium metal anode as exhibited by XPS results, operando XAS was employed to track the evolution of sulfur species during cycling. Additionally, molecular dynamics (MD) simulations were conducted to calculate the radial distribution functions (RDFs) and coordination numbers of Li–O and Li–Br (T3Br) pairs, revealing changes in the solvation structure of Li⁺ in the presence of the T3Br additive and its impact on polysulfide conversion kinetics. As a result, the Li–S batteries demonstrated outstanding cycling stability, with a low capacity decay rate of 0.049% per cycle after 700 cycles at 1 C. This formulation enabled high capacity under lean electrolyte conditions with an E/S ratio of 5 μL mg^{−1}.

Electrolytes with low solvating ability, including high concentration electrolytes (HCE) and LHCE, have been suggested and applied in Li–S batteries.^[235] However, these electro-

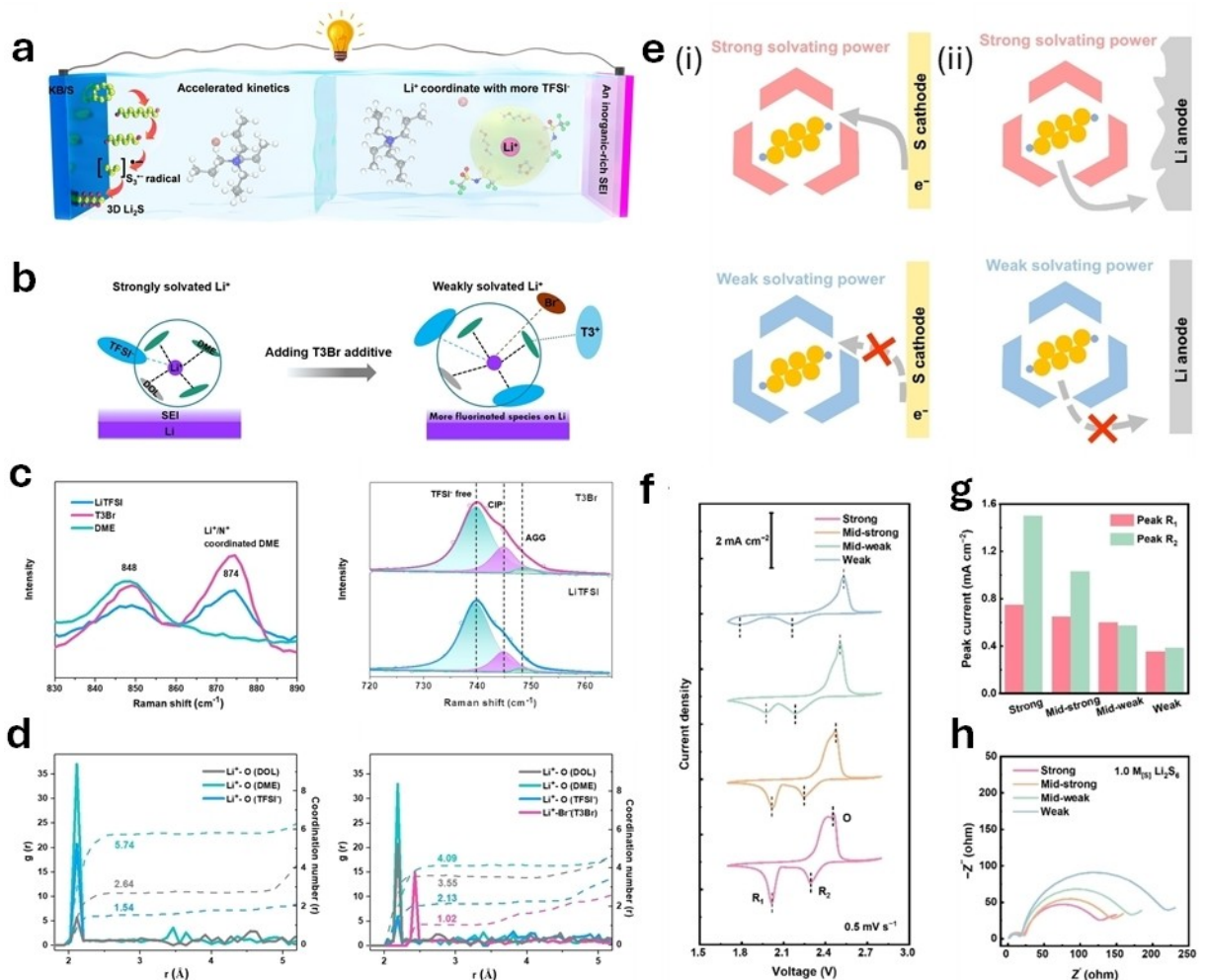


Figure 11. (a) Schematic illustration of the mechanism involving the S cathode and Li anode with the T3Br electrolyte. (b) Schematic illustration showing how blank LiTFSI and T3Br electrolytes affect SEI evolution on Li. (c) Raman spectra comparison of pure DME, blank LiTFSI electrolyte, and T3Br electrolyte (left), and deconvoluted Raman spectra highlighting the environment of TFSI⁻ anions in blank LiTFSI and T3Br electrolytes (right). (d) RDFs and coordination number plots of Li-O and Li-Br (T3Br) pairs calculated from MD simulations for blank LiTFSI (left) and T3Br electrolyte (right). Reproduced with permission.^[234] Copyright © 2023, R. Meng et al., Wiley-VCH. (e) Schematic representation of (i) cathode redox reactions of LiPSs with strong (upper) and weak (lower) solvation structures, and (ii) parasitic reactions between LiPSs and Li metal with strong (upper) and weak (lower) solvation structures. (f) CV curves and (g) corresponding peak currents for Li | Li₂S₈ cells at a scan rate of 0.5 mV s⁻¹. (h) EIS results of Li₂S₆ symmetric cells. Reproduced with permission.^[63] Copyright © 2023, Z. Li et al., Wiley-VCH.

lytes often exhibit sluggish cathode kinetics, severely limiting the capacity of these batteries.^[224,236] In contrast, electrolytes with strong solvating power have been widely used, but they tend to accelerate anode kinetics, which can limit their practical advantages in pouch cells with limited anode excess.^[237] To address these challenges, Li et al. proposed using HFE, which have weak solvating power, to regulate the solvation structure of LiPSs.^[63] In their study, dimethoxyethane (DME) was found to exist in both the inner and outer solvation shells of LiPSs, while HFE only appeared in the outer shell due to its weaker solvating power. This solvation structure significantly affects anode kinetics. Specifically, electrolytes with weaker solvating power suppress parasitic reactions between LiPSs and Li metal, reducing anode kinetics and influencing the morphology of deposited lithium. Consequently, weaker solvating power leads to denser and smoother lithium deposition, enhancing anode performance. Conversely, electrolytes with strong solvating

power, such as those with higher DME content, increase the solubility of LiPSs in the electrolyte. This robust solvation structure can result in more parasitic reactions between LiPSs and the Li metal anode, leading to several issues such as higher shuttle current, lower Coulombic efficiency, and inferior lithium deposition morphology. These effects negatively impact the performance and cycling stability of Li-S batteries (Figure 11e-h).

The key insight from this work is the importance of balancing cathode and anode kinetics by regulating the solvating power of the LiPS solvation structure. Strong solvating power induces rapid cathode and anode kinetics, which can accelerate LiPS formation while the Li metal anode can fail quickly due to destructive parasitic reactions. On the other hand, weak solvating power results in sluggish cathode kinetics, hindering the conversion processes of LiPSs but can effectively preserve the Li anode morphology. Therefore, an electrolyte

with medium solvating power can balance the kinetics at both electrodes, prolonging the cycling lifespan of Li–S batteries. Li's work demonstrated a Li–S coin cell with a thin Li anode using a mid-weak solvating electrolyte, which delivered a long cycling lifespan of 146 cycles with an initial specific capacity of 887 mAh g^{-1} and a capacity retention of 78.5% at a sulfur loading of 4.3 mg cm^{-2} . Additionally, a Li–S pouch cell with this medium solvation structure achieved a stable cycling lifespan of 30 cycles and an energy density of 338 Wh kg^{-1} based on the total mass of the pouch cell.

4.2.2. SEI Engineering Impact on Cell Performance

The SEI layer is crucial for the performance of lithium-based batteries, including Li–S batteries. A well-designed SEI layer can effectively inhibit the parasitic reaction between the lithium metal and the electrolyte, suppress the growth of lithium dendrites, and facilitate the uniform deposition of lithium, thereby improving the overall battery performance and safety. Strategies to optimize the SEI layer, such as surface modifications, advanced deposition techniques, and using electrolyte additives have been extensively explored to address the challenges associated with the lithium metal anode and unlock the full potential of Li–S batteries.

Li et al. employed 1,3,5-trioxane (TXA) as a cosolvent in Li–S batteries to form an organic-SEI (O-SEI) that is superior to the regular SEI (R-SEI) typically found in these batteries.^[66] The O-SEI exhibits higher mechanical stability, a greater proportion of organic components, and effectively suppresses parasitic reactions between LiPSs and the Li metal anode. This results in improved cycling performance and stabilized Li metal anodes, as shown in Figure 12. The Li–S pouch cell with O-SEI layer demonstrated an initial specific capacity of 1280 mAh g^{-1} and maintained stable cycling for 26 cycles with a capacity retention of 73% (Figure 12a). The cell utilized ultrathin Li metal anodes ($75 \mu\text{m}$) and high-areal-loading sulfur cathodes (7.8 mg cm^{-2}) with a low E/S ratio of $3.0 \text{ mL g}_{\text{sulfur}}^{-1}$. The Li | Li featuring O-SEI demonstrated a markedly extended cycling lifespan of 300 hours, in contrast to the 180 hours observed for the cell with R-SEI. This suggests improved stability of the Li metal anodes, attributed to a decrease in parasitic reactions (Figure 12b).

Li's group also used in-situ atomic force microscopy (AFM) to assess the SEI morphology in regular DOL-based and TXA-based electrolytes. In the DOL-based electrolyte, AFM images (Figure 12c-(i and ii)) show that random nanoparticles, approximately $3.0 \pm 0.2 \text{ nm}$ in height, began depositing on the electrode during the cathodic scan from 1.19–0.99 V. These nanoparticles expanded and dispersed slowly over an hour, likely representing slight decomposition products that do not

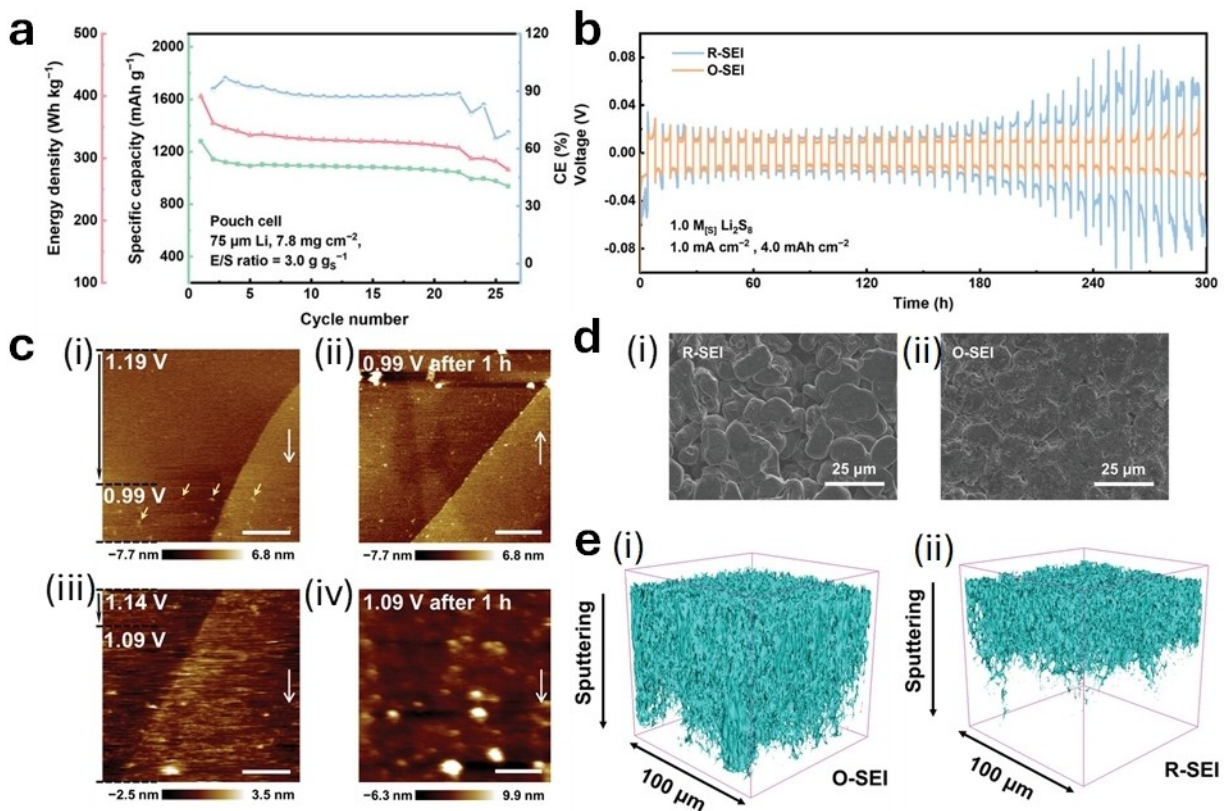


Figure 12. Cycling performance of the Li–S pouch cell using a TXA-based electrolyte. (b) Electrochemical performance of Li|Li symmetric cells at a current density of 1.0 mA cm^{-2} and an areal capacity of 4.0 mAh cm^{-2} . (c) In-situ AFM images in DOL-based electrolyte at different potentials: (i) 1.19–0.99 V, (ii) 0.99 V after 1 hour, and in TXA⁻-based electrolyte at cathodic (iii) 1.14–1.09 V, (iv) 1.09 V after 1 hour. (d) SEM images of deposited Li after five cycles with (i) R-SEI and (ii) O-SEI. (e) ToF-SIMS 3D distribution views of $\text{C}_2\text{H}_2\text{O}^-$ in (i) O-SEI and (ii) R-SEI. Reproduced with permission.^[66] Copyright © 2024, Z. Li et al., Wiley-VCH.

significantly contribute to SEI formation. In contrast, in the TXA-based electrolyte (Figure 12c–(iii and iv)), no visible changes were observed on the electrode during the cathodic sweep from OCP to 1.09 V, indicating that TXA preferentially decomposes reductively to form an organic-rich SEI. SEM images of deposited Li after 5 cycles (Figure 12d) reveal that Li with O-SEI has a dense and smooth morphology, whereas Li with R-SEI exhibits a loose and porous structure with extensive Li dendrites. XPS and ToF-SIMS results further indicate a higher concentration of $C_2H_2O^-$ species in the O-SEI compared to the R-SEI, suggesting a more homogeneous distribution of organic components in the O-SEI (Figure 12e). The introduction of TXA as a cosolvent leads to the formation of an organic-rich SEI on the lithium anode surface. This mitigates parasitic reactions between lithium polysulfides and the lithium metal anode, thereby improving the cycling performance of lithium-sulfur batteries.

4.2.3. Sparingly Solvating Electrolytes in Pouch Cell Applications

Liquid electrolytes in Li–S batteries significantly influence redox reaction kinetics, due to their influence on LiPS solubility.^[226] However, high solubility of polysulfides also leads to increased polysulfide shuttle effect, which causes electrolyte consumption and raises cycling stability concerns.^[63,67,218,219,238] To mitigate these issues, electrolyte component modification, development of new functional solvents, and the addition of various additives are critical areas for further exploration.^[168,216,239]

Weakly solvating electrolytes, which have low LiPS solvating power, can protect the lithium anode and improve cycling stability. However, they also hinder LiPS kinetics in the cathode, leading to increased polarization, reduced discharge capacity, and lower energy density. Li et al. investigated the LiPS kinetic degradation mechanism in weakly solvating electrolytes and proposed using a titanium nitride (TiN) electrocatalyst to construct high-energy-density Li–S batteries for pouch cell applications.^[218] Their findings, illustrated in Figure 13a, show that weakly solvating electrolytes impair LiPS kinetics in cathode reactions, thus increasing polarization and reducing energy density, particularly in practical pouch cells. DFT calculations on the conversion from Li_2S_4 to Li_2S indicate that as the content of highly solvating molecules (HME) increases, the rate-determining step shifts from Step III to Step II (Figure 13b), suggesting that both the decomposition of LiS_2 radical solvated by two solvent molecules and the generation of LiS radical solvated by two solvent molecules are kinetically unfavorable in LiPS liquid-solid conversions. The regional diagram of overpotential versus $\Delta G(LiS\cdot)$ and $\Delta G(LiS_2\cdot)$ (Figure 13c) reveals that the system with 2DME solvent is located in Region III, while the systems with HME + DME and 2HME solvents are located in Region II. Region III and Region II represent different thermodynamic and kinetic regimes for the liquid-solid conversion reactions in Li–S batteries, with Region II corresponding to more sluggish kinetics in weakly solvating electrolytes compared to Region III. This demonstrates that it is harder for the

$LiS_2\cdot$ radical solvated by HME to gain an electron and be converted to Li_2S_2 compared to the radical solvated by DME, which hinders the overall LiPS redox kinetics and induces enlarged overpotential of the liquid-solid conversion processes in weakly solvating electrolytes.

High-resolution SEM images of Li_2S precipitates on carbon paper (CP) electrodes demonstrate morphological changes in Li_2S deposits as electrolyte solvating power weakens, further confirming impaired liquid-solid conversion kinetics as shown in Figure 13e. Introducing TiN electrocatalysts reduces activation polarization in weakly solvating electrolytes. The GITT profiles of Li–S full cells with HME electrolytes, with and without TiN electrocatalysts, show a significant reduction in activation overpotential (from 115–35.2 mV at DOD = 0.3) and a decrease in their proportion of total polarization, indicating enhanced intrinsic interfacial charge transfer kinetics (Figure 13d). Ultimately, the 1st cycle and long cycling performances of 400 Wh kg⁻¹-level 2.5 Ah pouch cells with HME electrolyte and TiN electrocatalyst, as shown in Figure 13f, demonstrate the practical applicability of this optimization strategy. This approach highlights the importance of electrolyte and electrocatalyst selection in achieving high-performance Li–S batteries.

In Li–S batteries, an excessive amount of electrolyte significantly undermines their high-energy-density potential. The E/S ratio is crucial for determining the achievable energy density of a practical Li–S cell.^[95,150,185,226] However, under low E/S ratio conditions, the sulfur cathode kinetics become extremely sluggish, resulting in reduced discharge capacity and limited cycling rates. A comprehensive kinetic analysis is necessary to identify the key limiting factors and guide the design of strategies to enhance kinetics under practical lean-electrolyte conditions. To address these kinetic limitations, Chen et al. conducted a comprehensive investigation of the E/S ratio impact on the activation polarization in Li–S batteries.^[226] As the E/S ratio decreases, kinetic voltage (polarization) increases significantly, particularly during the Li_2S nucleation stage. When LiFSI is used in a lean electrolyte with an E/S ratio of 4 $\mu L mg^{-1}$, the total polarization drops significantly at 0.08 C. The most notable reduction occurs in the rate-determining step of Li_2S nucleation. The rate performance at an E/S ratio of 4 $\mu L mg^{-1}$ indicates that cells using the LiFSI electrolyte achieved higher specific capacities of 800, 229, and 216 mAh g⁻¹ at 0.2, 0.1, and 0.08 C, respectively, which are significantly higher compared to cells using the LiTFSI electrolyte. The corresponding charge-discharge profiles at different rates further demonstrate the improved kinetic performance of cells with the LiFSI electrolyte under lean electrolyte conditions. Moreover, electrolytes with low salt concentrations are also used to operate Li–S batteries under cryogenic conditions.^[240]

5. Advanced Characterization Techniques for Li–S Batteries

Advanced characterization techniques are indispensable for the study and development of lithium-sulfur (Li–S) batteries,

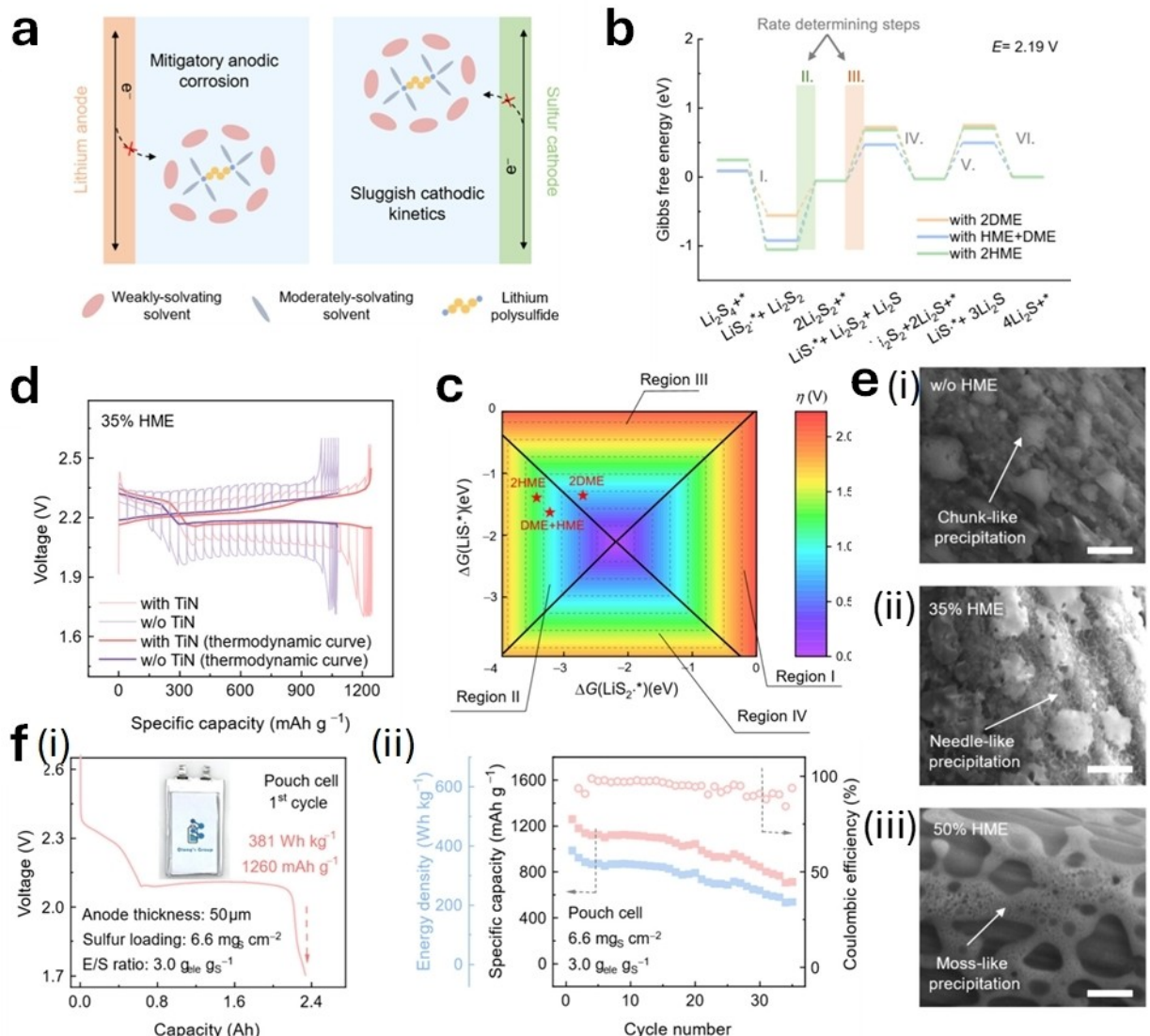


Figure 13. (a) Schematic of the LiPS anodic and cathodic behaviors in a weakly solvating electrolyte. (b) Calculated Gibbs free energy diagrams of the liquid-solid conversion from Li_2S_4 to Li_2S at the equilibrium potential in 2DME, DME + HME, and 2HME electrolytes. (c) Regional diagrams of overpotential versus $\Delta G(\text{LiS}_2^{x+})$ and $\Delta G(\text{Li}_2\text{S}_4)$ for the liquid-solid conversion from Li_2S_4 to Li_2S . (d) GITT profiles of Li–S full cells using HME electrolytes with or without TiN electrocatalysts. (e) High-resolution SEM images of the Li_2S precipitates on CP electrodes with (i) no HME, (ii) 35% HME, and (iii) 50% HME (scale bar: 1 μm). (f) Cycling performances of 400 Wh kg⁻¹-level 2.5 Ah pouch cells with HME electrolyte and TiN electrocatalyst: (i) 1st cycle and (ii) up to 38 cycles, with energy density calculated based on the total mass of the pouch cell (inset: photograph of the pouch cell). Reproduced with permission.^[218] Copyright © 2024, American Chemical Society.

offering profound insights into the mechanisms and challenges of these systems by probing their structural, chemical, and electrochemical properties.^[241,242] These techniques elucidate critical issues such as electrode/electrolyte degradation, polysulfide shuttling effect, and sluggish kinetics associated with polysulfides.^[1,243,244] Spectroscopy, in particular, is highly regarded in both industry and academia for its ability to provide quantitative or quasi-quantitative information on the chemical pathways and structural evolution within the investigated systems, offering significant benefits for chemists.^[244–246]

Spectroscopic methods are highly versatile and can be broadly categorized into in-situ (or operando) and ex-situ techniques. In-situ/operando experiments provide real-time

information about the reaction pathway or structure evolution at different depths of discharge (DoD) or states of charge (SoC), while ex-situ experiments offer crucial data for interpreting the results from in-situ/operando modes.^[242,247–249] Common techniques such as Raman spectroscopy, X-ray absorption spectroscopy (XAS), X-ray photoelectron spectroscopy (XPS), ultraviolet-visible (UV-vis) spectroscopy, and Fourier-transform infrared (FT-IR) spectroscopy are all adaptable and can be easily conducted in-situ or operando with appropriate customized cell designs.^[150,250–258] Other methods including diffractometry such as XRD, microscopy such as scanning electron microscopy (SEM) and transmission electron microscopy (TEM), and electrochemistry such as CV and EIS are also widely employed in Li–S

battery research for various purposes.^[107,108,159,259,260] Each technique provides unique insights into sulfur and lithium polysulfide behavior, structural changes, and morphological evolution. However, it is essential to recognize that a comprehensive understanding of Li–S chemistry cannot be achieved through a single technique alone. The combined application of multiple techniques is necessary to gain a precise and holistic understanding of the investigated system. Furthermore, conventional pouch cell designs are often impractical for such advanced characterization, requiring substantial effort in troubleshooting and customizing setups. Consequently, experiments are typically conducted using customized coin cells with specialized optical windows or commercial spectroscopy cells such as EL-CELL®. This approach is widely accepted in academia for pouch cell evaluation, as the fundamental electrochemical principles are consistent across both systems.^[244,261,262] However, an in-situ/operando pouch cell design is preferable for maintaining setup consistency. Certain advanced techniques, such as XAS, necessitate additional administrative procedures. For instance, utilizing synchrotron facilities for XAS involves a stringent application process to evaluate the scientific significance and novelty of the proposed research. Table 1 summarizes these advanced characterization techniques, comparing their principles, scopes

of application, and limitations in the context of Li–S battery research.

5.1. In-Situ/Operando Raman Spectroscopy

In general, Raman spectroscopy is highly advantageous in Li–S battery studies because sulfur-related species exhibit significant sensitivity to Raman shifts. This technique allows for the qualitative or semi-quantitative detection of soluble polysulfides in ether-based electrolytes during cycling.^[11,263,264] For instance, Liu et al. effectively utilized a modified coin cell with a spectroscopy window for in-situ Raman spectroscopy to identify and quantify specific reaction intermediates and their transformations during the discharge process in sulfur redox reactions (Figure 14a).^[11] By integrating CV results with the sulfur redox reactions using an N,S-HGF catalyst, distinct peaks at various potentials indicated the presence and transformation of specific intermediates (Figure 14b-i). In-situ Raman spectroscopy further facilitated the identification and tracking of intermediates such as Li_2S_4 , Li_2S_6 , and Li_2S_8 , along with their conversion processes throughout the discharge cycle. The appearance and disappearance of particular Raman peaks at

Table 1. Summary of advanced characterization techniques, detailing their fundamental principles, application scopes, limitations, and illustrative examples from literature.

Characterization techniques	Fundamental Principle	Application	Limitation	Example
In-situ/operando Raman	Various vibrational modes of Raman-active sulfur species	Track sulfur and polysulfides transformation and conversion	Relatively less sensitive to the polysulfides with shorter chain orders	Identification and quantification of polysulfides and reaction kinetics in Li–S batteries using N,S-HGF catalyst ^[11,264]
In-situ/operando XAS	X-ray beam excites a core electron, promoting it to an unoccupied level or ejecting it from the atom.	Determine sulfur valence state and local coordination structure, regardless of sulfur compound crystallinity	Requires a specialized custom cell design for in-situ/operando experiments	Elucidate the stabilizing effect of LiNO_3 between the polysulfides in Li–S batteries ^[268]
In-situ XPS	When excited by high-energy UV photons with sufficient ionizing energy, materials will eject electrons	Monitor chemical compositions and identify elements qualitatively or semi-quantitatively with detection limits of approximately 0.1%–1%	Typically probes depths from a few nanometers to a few microns as a more surface sensitive tool, hard to conduct in operando mode	Monitor the SEI formed on the Li metal anode of a TTCA–Li coating Li_2S cathode ^[210,270]
In-situ/operando XRD	Interference enhancement and disappearance of X-rays create a diffraction pattern when scattered by crystalline sulfur species	Monitor the crystalline structures of the final discharge product (Li_2S) and the final charge product (S_8)	More sensitivity to periodic crystal structures	Track the polysulfides conversion during cycling at a $\text{VS}_4@\text{RGO}$ host for sulfur in Li–S batteries ^[271]
In-situ/operando UV-vis	Absorption of the ultraviolet and visible light	Identify different polysulfides qualitatively and quantitatively	The spectra are a collective spectrum of all soluble polysulfides during in-situ/operando experiments	Investigate the evolution of lithium disulfide (Li_2S_2) and its impact on the reversible capacity of Li–S batteries ^[272]
In-situ/operando FT-IR	Absorption of infrared light from vibrational frequencies of groups	Sensitive to molecular structure and detect the sulfur species	Possible interference from organic solvents	Detect sulfur converted to Li_2S_8 during the discharge process and subsequently reduced to LiPs ^[254]
In-situ EIS	Apply a small amplitude sinusoidal excitation signal to the system under investigation and measure the response	Capable to detect all impedance change during the redox reaction pathway	Requires specialized fitting procedure for quantitative information such as equivalent circuit model	Calculate the activation energy associated with the polysulfides conversion kinetics at different DoDs ^[107]

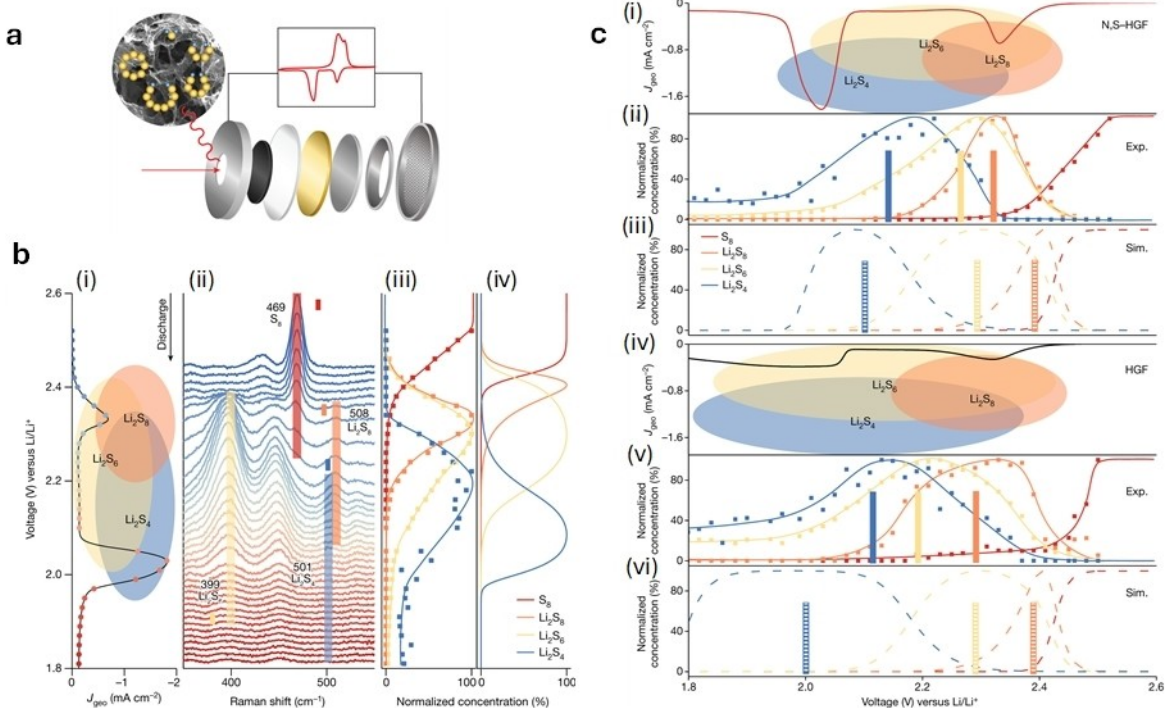


Figure 14. (a) Schematic representation of the in-situ Raman technique. (b) (i) CV profile and (ii) experimental in-situ Raman spectra for N,S-HGF, with colors indicating specific voltages. The Raman cell was operated with a scan rate of 0.05 mV s^{-1} during discharge CV, highlighting characteristic peaks of each intermediate polysulfide. Comparison between (iii) experimental voltage-dependent concentrations and (iv) simulated concentrations from DFT derived from in-situ Raman spectra. (c) (i and iv) Experimental CV curves, (ii and v) experimental and (iii and vi) simulated voltage-dependent concentrations for each polysulfide species for N,S-HGF and HGF, respectively. Colored bars indicate the peak centers of voltage-dependent concentration curves for each species: orange for Li_2S_8 , yellow for Li_2S_6 , and blue for Li_2S_4 . Solid lines and bars in (ii) and (v) represent experimental results, while dashed lines and bars in (iii) and (vi) represent simulated results. Reproduced with permission.^[11] Copyright © 2024, R. Liu et al., Nature 2024, published by Springer Nature.

different potentials revealed the conversion of one polysulfide species to another (Figure 14b-ii). The Raman spectra were analyzed using peak deconvolution and assignments were given for different polysulfides based on their behavior during the sulfur redox process, previous reports, and DFT simulations.^[250,265–267] Specific Raman shifts, such as 501, 399, 508, and 469 cm^{-1} , were primarily used to quantify Li_2S_4 , Li_2S_6 , Li_2S_8 , and elemental sulfur (S_8), respectively. These shifts allowed researchers to determine the voltage-dependent concentrations of various polysulfides and validate the concentration evolution of different species with decreasing potential by comparing with DFT calculation results (Figure 14b-(iii and iv)). Combining CV data with in-situ Raman spectroscopy provided valuable insights into the electrochemical transformation pathways of polysulfides and the kinetics of these reactions. This comprehensive approach enhanced the understanding of the reaction mechanisms in sulfur redox processes when comparing two different catalyst systems, N,S-NF and NGF (Figure 14c).

Lang et al. employed operando confocal Raman microscopy to advance redox investigations by simultaneously identifying sulfur and polysulfides, imaging their spatial distribution at high resolution, and quantitatively analyzing the Li–S redox mechanism and kinetics.^[264] High-resolution imaging offers detailed visual information on the spatial distribution of sulfur and polysulfides during redox processes. This technique enables the visualization of potential-dependent reactants and intermediates,

quantification of intensity changes, and comparisons among various classical models, thereby elucidating the first-order reaction kinetics of sulfur reduction and polysulfide redox processes.

These instances clearly demonstrate Raman spectroscopy's capability as a quantitative tool for analyzing the concentration and distribution of polysulfides within Li–S redox reactions, establishing in-situ Raman spectroscopy as a prevalent technique for investigating the associated kinetics. Moreover, the design of cells for Raman spectroscopy is practical since the visible wavelength laser permits the use of sapphire or quartz windows. These durable optical windows simplify the customization of the spectroscopy cell, thereby making Raman spectroscopy a widely utilized technique in advanced characterization.

5.2. In-Situ/Operando X-Ray Absorption Spectroscopy

While Raman spectroscopy offers distinct advantages for studying the chemical evolution within Li–S batteries, it also has certain limitations, such as detecting short-chain polysulfides (Li_2S_x , $x < 5$). Acquiring Raman spectra in an ex-situ mode is straightforward, but replicating these results in an in-situ or operando mode is challenging. One of the primary reasons is that short-chain polysulfides are less sensitive to Raman shifts.

Additionally and more significantly, during the discharge/charge process, the polysulfides are often present as a mixture, complicating the analysis because Raman spectroscopy relies on the vibrational modes of chemical bonds.^[11] In contrast, XAS offers excellent elemental selectivity, enabling it to overcome these issues. XAS can be effectively developed as an in-situ/operando technique to track polysulfide formation within Li–S batteries, thereby complementing Raman spectroscopy.^[258,268,269] However, XAS also presents its own challenges, particularly the dependency of the optical window material on the synchrotron beam specifications, which vary with the atomic number of the target element. For sulfur, which has a lower K-edge range of 2460–2480 eV within the so called “tender X-ray” energy range,

the X-ray beams are more readily absorbed by window materials, complicating their selection.

Rahman et al. utilized a modified coin cell with an in-situ XAS setup to investigate the reactivity of lithium nitrate (LiNO_3) with polysulfides in Li–S batteries, aiming to elucidate the stabilizing effect of LiNO_3 , commonly used as an electrolyte additive (Figure 15a).^[268] Their study revealed a spatially progressing chemical reaction influenced by the polysulfide concentration gradient, thereby illuminating the complex electrolyte chemistry. The top panels of Figure 15b display sulfur K-edge spectra collected from the electrolyte near the sulfur cathode, while the bottom panels show spectra from the electrolyte near the Li metal anode. Peaks in these spectra

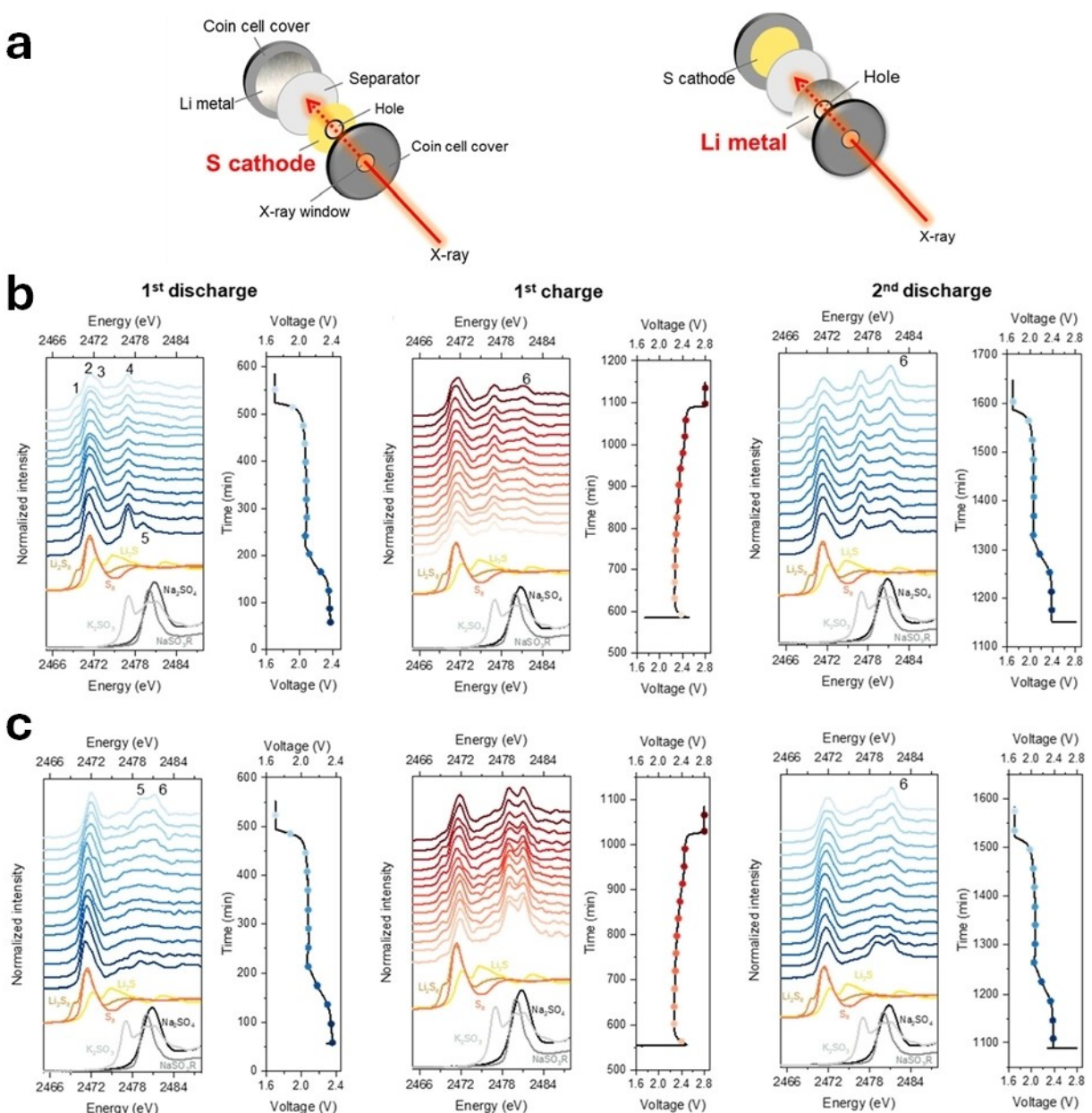


Figure 15. (a) Schematic illustration of operando XAS cell configurations. Two configurations were showed with focusing on the sulfur cathode side (left) and the lithium metal anode side (right). (b–c) Operando Sulfur K-edge spectra at different cycling stages from (b) the electrolyte near the sulfur cathode, and (c) electrolyte near the Li metal anode. Identified peaks are: 1, charged end of polysulfide; 2, S–S σ^* transition; 3, Li₂S; 4, sulfite; 5, sulfonate; and 6, sulfate. Reproduced with permission.^[268] Copyright © 2024, American Chemical Society.

correspond to various sulfur-derived species, such as polysulfides, elemental sulfur, Li_2S , sulfites, sulfonates, and sulfates, identified as peaks 1 through 6. These peaks, collected at different stages of cycling, provide insights into the transformation of polysulfides into other sulfur species as cycling progresses, reflecting the interaction between polysulfides and LiNO_3 throughout the cell. By analyzing the electrolyte on both the cathode and anode sides, XAS facilitated a deeper understanding of the reactivity of LiNO_3 and its role in stabilizing Li–S batteries. The study revealed the formation of oxidized sulfur species, such as sulfites, sulfonates, and sulfates, which contribute to passivating the interphases and preventing polysulfide shuttling.

Similarly, Xu et al. utilized operando XAS to investigate the catalytic mechanisms of Li–S batteries employing cobalt single-atom electrocatalysts (Co-SAs/NC).^[269] This technique was used to examine the dynamic chemical state evolution of the sulfur composite cathode during discharge-recharge cycles. The sulfur K-edge spectra provided detailed insights into the speciation of sulfur species, including elemental sulfur (S_8), lithium sulfide (Li_2S), and polysulfides, throughout the electrochemical processes. The data highlighted the conversion of elemental sulfur into polysulfides and Li_2S , and the subsequent oxidation of Li_2S back to polysulfides and elemental sulfur (S_8). This enhanced the understanding of electrocatalysis and interfacial dynamics in electrical energy storage systems.

It should be noted that the salts commonly used in Li–S batteries, such as LiTFSI or LiFSI, can significantly interfere with XAS measurements due to the sulfur compounds within the salts. Consequently, some researchers opt to replace these salts with lithium perchlorate (LiClO_4) for in-situ/operando studies or perform a washing procedure to remove residual salts from the surface for ex-situ investigations.^[94,268]

5.3. Other In-Situ/Operando Techniques

In addition to Raman and XAS spectroscopy, which can directly probe the redox pathways of sulfur and polysulfides, several other techniques address different aspects of Li–S battery performance.

XPS is widely used to monitor chemical compositions and identify elements qualitatively or semi-quantitatively. However, due to its surface sensitivity, XPS typically probes depths from a few nanometers to a few microns, making it particularly suitable for investigating thin layers such as the solid electrolyte interphase (SEI) or the cathode electrolyte interphase (CEI). Zhang et al. employed in-situ irradiated X-ray photoelectron spectroscopy (ISI-XPS) to convert the “black box” Li–S battery into a “see-through” battery, directly observing and identifying selective bifunctional electrocatalytic sites that promote redox reactions.^[270] Using an amorphous $\text{TiO}_{2-x}/\text{Ni}$ model catalyst, the study reveals that the amorphous TiO_{2-x} and Ni nanoparticles serve as oxidation and reduction sites, respectively, selectively facilitating the decomposition and nucleation of Li_2S .

XRD is highly valued for its sensitivity to periodic crystal structures, though its application in Li–S studies is constrained

due to the amorphous nature of most intermediate polysulfides. Consequently, XRD is predominantly used to monitor the crystalline structures of the final discharge product (Li_2S) and the final charge product (S_8). Luo et al. showcased the fabrication and performance of a novel three-dimensional hybrid architecture, $\text{VS}_4@\text{RGO}$, as a sulfur host for Li–S batteries.^[271] The in-situ XRD analysis elucidates the enhanced polysulfide absorptivity and redox conversion reversibility offered by the $\text{VS}_4@\text{RGO}$ structure. Notably, the in-situ XRD results reveal that the cell containing $\text{VS}_4@\text{RGO}$ exhibits significantly weaker polysulfide signals at the end of discharge compared to the control cell without VS_4 , indicating a substantial reduction in polysulfide diffusion and improved polysulfide utilization in the $\text{VS}_4@\text{RGO}$ configuration as shown in Figure 16a. Furthermore, the in-situ XRD analysis demonstrates that at the end of charge, the intensities of sulfur peaks for the cell with $\text{VS}_4@\text{RGO}$ are markedly decreased compared to the beginning of discharge. This suggests that the well-distributed VS_4 nanoparticles effectively absorb polysulfides and redistribute sulfur species into smaller particles during the redox conversion.

UV-vis spectroscopy is adept at monitoring the formation of intermediate polysulfides, as these species exhibit distinct light transmittance properties based on their chain orders. However, the effectiveness of UV-vis spectroscopy is highly dependent on the dissolution of various polysulfides in the solution. During in-situ/operando conditions, the solution typically contains a mixture of different polysulfides, which complicates precise quantitative analysis. Therefore, validation with complementary techniques such as Raman or XAS is often necessary to ensure accuracy. Luo et al. utilized an operando pouch cell for UV-vis experiments to investigate the evolution of lithium disulfide (Li_2S_2) and its impact on the reversible capacity of Li–S batteries.^[272] The operando UV-vis data reveals that Li_2S_2 undergoes slow electrochemical reduction and chemical disproportionation during the discharge process, leading to further polysulfide dissolution and Li_2S generation without contributing to capacity. During charging, the oxidation of Li_2S to Li_2S_2 involves both electrochemical conversion and chemical neutralization (Figure 16b). The residual Li_2S_2 , rather than Li_2S , is identified as the solid “dead” sulfur, which limits sulfur utilization and reversible capacity.

Several other common techniques are employed to track electrochemical pathways and understand the modified electrocatalysis within Li–S battery systems. In-situ FT-IR spectroscopy is used to identify lithium polysulfides through their S–S vibration modes, providing insights into electrochemical processes.^[254,273] Additionally, electrochemical techniques such as CV and EIS are instrumental in monitoring polysulfide formation and analyzing the system’s kinetics.^[107,274–276] However, FT-IR spectroscopy is highly sensitive to organic compounds in the electrolyte, which can interfere with data interpretation. While CV and EIS are valuable for distinguishing different impedance contributions from various processes within the Li–S battery system, a dedicated analysis procedure, such as Randles-Sevcik analysis for CV or an equivalent circuit model (ECM) for EIS, is necessary to obtain quantitative or semi-

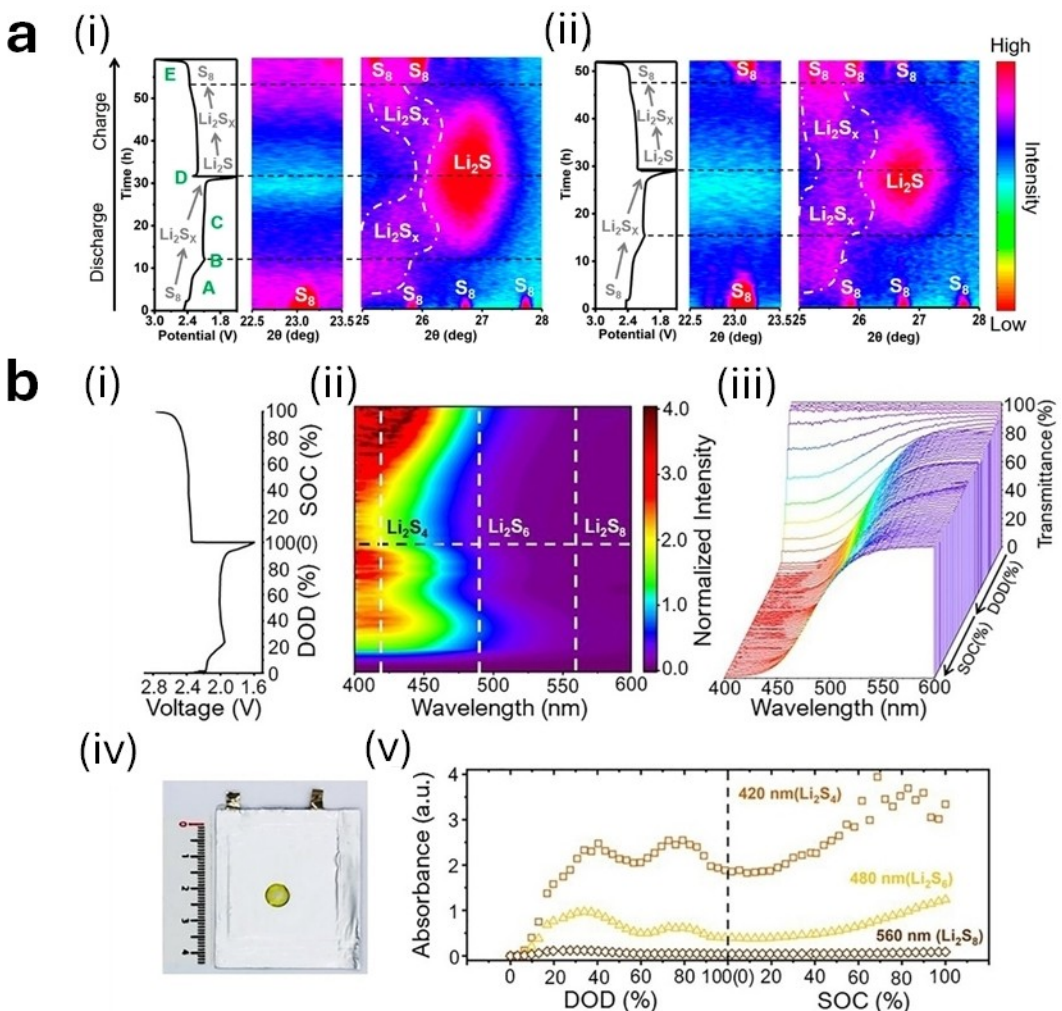


Figure 16. (a) In-situ XRD contour plots of the Li–S cells (i) with and (ii) without VS₄ during the first discharge/charge cycle. Reproduced with permission.^[271] Copyright © 2020, American Chemical Society. (b) Operando UV-vis measurements of a pristine Li–S pouch cell. (i) and (ii) display voltage profiles and the corresponding operando UV-vis spectra. (iii) displays operando UV-vis spectra at different DOD and SOC. (iv) illustrates an optical image of the cycled pouch cell with a polyethylene window. (v) presents absorbance data of dissolved polysulfides at 420 nm (Li₂S₄), 480 nm (Li₂S₆), and 560 nm (Li₂S₈) during cycling. Reproduced with permission.^[272] Copyright © 2023, Y. Luo et al., Wiley-VCH.

quantitative information. Once optimized, these techniques could significantly enhance the understanding of the kinetics associated with lithium-ions and polysulfides.

6. Summary and Outlook

In order to advance the commercial potential of lithium-sulfur technology, it is crucial to guide Li–S research along the pathway of scale-up and widespread evaluation at the pouch cell level. Energy density is typically an ignored parameter in coin cells, but gravimetric energy density becomes critical as the technology approaches commercialization. Recent battery development has been geared towards achieving 500 Wh kg⁻¹ at the cell level, which is within the theoretical energy density limit of Li–S technology. Pouch cells provide a promising avenue for realizing this target due to their comparative ease of fabrication at the lab scale, scalability and low packaging

weights, compared to other cell formats. However, although Li–S pouch cells were first built in 2014, it is still challenging to achieve consistent performance in the larger cell format a decade later due to the different failure mechanisms of pouch cells. A summary of the key factors needed to fabricate high energy density, long cycle life pouch cells at the lab scale is necessary at this time to drive lithium-sulfur battery development towards this goal.

This review aims to elucidate the differences between coin and pouch cells to understand these new failure mechanisms and highlights a few key parameters to focus on to improve pouch cell design. We concur with other reviews of Li–S technology in emphasizing the importance of low E/S ratio, low N/P ratio, and high areal sulfur loading as drivers of high energy density. Operating at lean electrolyte conditions of E/S < 3 μL mg⁻¹ is vital for achieving an energy density beyond 400 Wh kg⁻¹, but these conditions often induce low capacity and early cell failure due to regional electrolyte depletion,

which creates cell polarization and isolates active material. Hence, we also highlight the importance of optimizing the stack pressure due to this spatial reaction inhomogeneity often observed in pouch cells. Moreover, cathode design that facilitates planar electrolyte diffusion is needed to lower the possibility of dry areas in the electrodes. From a fabrication perspective, electrolyte filling in pouch cells can be irregular, which is intensified with low electrolyte volume and multiple electrode layers. Furthermore, lithium stabilization is a critical parameter for achieving long cycle life in pouch cells. High areal sulfur loading in pouch cell cathodes enables higher capacity due to the larger amount of sulfur packed into the cell, but also creates a need for high operating current, which can exacerbate the formation of Li dendrites and nonuniform lithium plating/stripping. Moreover, the polysulfide shuttle worsens with increased sulfur, which depletes more lithium to reactions with dissolved polysulfides. Operating at low N/P ratio < 3 results in a low availability of lithium, which makes the anode more vulnerable to depletion through dendrite formation or passivation. To address these issues, several electrolyte-focused anode protection strategies validated in pouch cells are reviewed. Combining these with rational cathode design and reliable methods of fabrication is expected to result in high-performing pouch cells with long cycle life.

Commercialization of Li–S technology also requires that battery manufacturers address a few practical issues beyond electrochemical performance, such as cell safety and calendar life. Lithium-sulfur batteries are at risk of thermal runaway and cell rupture in the event of short-circuit due to the volatile nature of electrolyte solvents and lithium metal, and we cover the mechanisms of this phenomenon to develop preventative strategies. The separator is considered the most promising avenue to suppress internal short-circuit for the cell in the case of thermal runaway; a few studies that improved the heat resistance of separators while maintaining their intrinsic performance are referenced. Finally, calendar life is another aspect of Li–S technology that is poorly understood due to different failure mechanisms and lack of research. In the last six years, both theoretical and experimental calendar aging studies have been increasingly conducted on lithium-sulfur cells. Protecting the anode from parasitic reactions over long periods of time remains the main challenge, but several innovative methods of regulating lithium plating/stripping, promoting dense anode morphology and applying protective coatings to the lithium surface have been included here as promising approaches.

To appropriately study the fundamentals of pouch cell electrochemistry, interface evolution and the phase transitions of various species, advanced characterization techniques are required. A summary of various in-situ spectroscopic techniques such as Raman, NMR, XAS and XPS among others is provided to illustrate the capabilities of each and the advantages of utilizing multiple techniques together. Through these techniques, it is possible to gain a deep understanding of the sulfur reduction reaction pathways, the kinetics associated with the various lithium polysulfide species, and the lithium surface evolution during cycling. Moreover, studying the spatial variations in

these reactions can provide useful information for improving the cell design.

Lithium-sulfur technology is a promising field of research that has received growing attention over the past two decades. Along with the fundamental challenges of the Li–S chemistry such as the polysulfide shuttle and insulating cathode material, it is now time to address the challenges that come with scaling up and increasing the energy density of the cells, which are altogether new fields of study. The guidelines provided in this review and others are expected to address these trials and facilitate the fabrication and evaluation of high-energy density lithium-sulfur pouch cells. The commercialization for Li–S technology as a sustainable and high-capacity battery promises a great breakthrough in energy storage once realized.

Acknowledgements

The authors acknowledge financial support received from the U.S. Department of Energy (DOE), Vehicle Technology Office under award No. DE-EE0009646.

Conflict of Interests

The authors declare no conflict of interest.

Keywords: Lithium-sulfur batteries · Pouch cells · Calendar ageing · Heteroatom catalysis · Lithium anode

- [1] A. Manthiram, Y. Fu, Y.-S. Su, *Acc. Chem. Res.* **2013**, *46*, 1125–1134.
- [2] J. W. Choi, D. Aurbach, *Nat. Rev. Mater.* **2016**, *1*, 1–16.
- [3] M. R. Busche, P. Adelhelm, H. Sommer, H. Schneider, K. Leitner, J. Janek, *J. Power Sources* **2014**, *259*, 289–299.
- [4] Z. X. Chen, M. Zhao, L. P. Hou, X. Q. Zhang, B. Q. Li, J. Q. Huang, *Adv. Mater.* **2022**, *34*, 2201555.
- [5] H. Dai, R. Besser, *Appl. Energy* **2022**, *307*, 118163.
- [6] A. Manthiram, Y. Fu, S.-H. Chung, C. Zu, Y.-S. Su, *Chem. Rev.* **2014**, *114*, 11751–11787.
- [7] J.-M. Tarascon, M. Armand, *Nature* **2001**, *414*, 359–367.
- [8] G. Zhou, H. Chen, Y. Cui, *Nat. Energy* **2022**, *7*, 312–319.
- [9] Y. Jie, C. Tang, Y. Xu, Y. Guo, W. Li, Y. Chen, H. Jia, J. Zhang, M. Yang, R. Cao, Y. Lu, J. Cho, S. Jiao, *Angew. Chem.* **2024**, *136*, e202307802.
- [10] A. Manthiram, S. H. Chung, C. Zu, *Adv. Mater.* **2015**, *27*, 1980–2006.
- [11] R. Liu, Z. Wei, L. Peng, L. Zhang, A. Zohar, R. Schoeppner, P. Wang, C. Wan, D. Zhu, H. Liu, *Nature* **2024**, *626*, 98–104.
- [12] M. A. Pope, I. A. Aksay, *Adv. Energy Mater.* **2015**, *5*, 1500124.
- [13] Z. W. Seh, Y. Sun, Q. Zhang, Y. Cui, *Chem. Soc. Rev.* **2016**, *45*, 5605–5634.
- [14] M. Zhao, B.-Q. Li, X.-Q. Zhang, J.-Q. Huang, Q. Zhang, *ACS Cent. Sci.* **2020**, *6*, 1095–1104.
- [15] H. Li, Y. Li, L. Zhang, *SusMat* **2022**, *2*, 34–64.
- [16] R. Deng, M. Wang, H. Yu, S. Luo, J. Li, F. Chu, B. Liu, F. Wu, *Energy Environ. Mater.* **2022**, *5*, 777–799.
- [17] J. Wang, W. Q. Han, *Adv. Funct. Mater.* **2022**, *32*, 2107166.
- [18] S. Li, Z. Fan, *Energy Storage Mater.* **2021**, *34*, 107–127.
- [19] L. Yang, Q. Li, Y. Wang, Y. Chen, X. Guo, Z. Wu, G. Chen, B. Zhong, W. Xiang, Y. Zhong, *Ionics* **2020**, *26*, 5299–5318.
- [20] H. Ye, Y. Li, *InfoMat* **2022**, *4*, e12291.
- [21] G. Xu, B. Ding, J. Pan, P. Nie, L. Shen, X. Zhang, *J. Mater. Chem. A* **2014**, *2*, 12662–12676.
- [22] S. H. Chung, C. H. Chang, A. Manthiram, *Adv. Funct. Mater.* **2018**, *28*, 1801188.

- [23] C. X. Bi, M. Zhao, L. P. Hou, Z. X. Chen, X. Q. Zhang, B. Q. Li, H. Yuan, J. Q. Huang, *Adv. Sci. (Weinh)* **2022**, 9, 2103910.
- [24] H. Zhao, N. Deng, J. Yan, W. Kang, J. Ju, Y. Ruan, X. Wang, X. Zhuang, Q. Li, B. Cheng, *Chem. Eng. J.* **2018**, 347, 343–365.
- [25] X. Xu, S. Wang, H. Wang, B. Xu, C. Hu, Y. Jin, J. Liu, H. Yan, *J. Storage Mater.* **2017**, 13, 387–400.
- [26] L. Zhou, D. L. Danilov, F. Qiao, J. Wang, H. Li, R. A. Eichel, P. H. Notten, *Adv. Energy Mater.* **2022**, 12, 2202094.
- [27] S. Rehman, K. Khan, Y. Zhao, Y. Hou, *J. Mater. Chem. A* **2017**, 5, 3014–3038.
- [28] S. Dörfler, H. Althues, P. Härtel, T. Abendroth, B. Schumm, S. Kaskel, *Joule* **2020**, 4, 539–554.
- [29] Y. Fei, G. Li, *Adv. Funct. Mater.* **2024**, 34, 2312550.
- [30] G. Liu, Q. Sun, Q. Li, J. Zhang, J. Ming, *Energy Fuels* **2021**, 35, 10405–10427.
- [31] Q. Zou, Y.-C. Lu, *J. Phys. Chem. Lett.* **2016**, 7, 1518–1525.
- [32] Q. He, Y. Gorlin, M. U. Patel, H. A. Gasteiger, Y.-C. Lu, *J. Electrochem. Soc.* **2018**, 165, A4027–A4033.
- [33] G.-Y. Du, C.-Y. Liu, E. Y. Li, *Catalysts* **2020**, 10, 911.
- [34] J. Gao, M. A. Lowe, Y. Kiya, H. D. Abruna, *J. Phys. Chem. C* **2011**, 115, 25132–25137.
- [35] Q. Li, J. Chen, L. Fan, X. Kong, Y. Lu, *Green Energy & Environ.* **2016**, 1, 18–42.
- [36] K. Sun, Q. Wu, X. Tong, H. Gan, *ACS Appl. Energ. Mater.* **2018**, 1, 2608–2618.
- [37] F. Y. Fan, M. S. Pan, K. C. Lau, R. S. Assary, W. H. Woodford, L. A. Curtiss, W. C. Carter, Y.-M. Chiang, *J. Electrochem. Soc.* **2016**, 163, A3111.
- [38] C. C. Su, M. He, R. Amine, Z. Chen, K. Amine, *Angew. Chem.* **2018**, 57, 12033–12036.
- [39] N. N. Rajput, V. Murugesan, Y. Shin, K. S. Han, K. C. Lau, J. Chen, J. Liu, L. A. Curtiss, K. T. Mueller, K. A. Persson, *Chem. Mater.* **2017**, 29, 3375–3379.
- [40] X. Liu, C. Shen, N. Gao, Q. Hou, F. Song, X. Tian, Y. He, J. Huang, Z. Fang, K. Xie, *Electrochim. Acta* **2018**, 289, 422–427.
- [41] Y. W. Song, L. Shen, N. Yao, S. Feng, Q. Cheng, J. Ma, X. Chen, B. Q. Li, Q. Zhang, *Angew. Chem.* **2024**, 63, e202400343.
- [42] W. Ren, W. Ma, S. Zhang, B. Tang, *Energy Storage Mater.* **2019**, 23, 707–732.
- [43] M. Zhao, B. Li, H. Peng, H. Yuan, J. Wei, J.-Q. Huang, *Angew. Chem.* **2020**, 132, 2–20.
- [44] S. Xin, L. Gu, N.-H. Zhao, Y.-X. Yin, L.-J. Zhou, Y.-G. Guo, L.-J. Wan, *J. Am. Chem. Soc.* **2012**, 134, 18510–18513.
- [45] Z. Zeng, X. Liu, *Adv. Mater. Interfaces* **2018**, 5, 1701274.
- [46] J. Zhang, H. Huang, J. Bae, S. H. Chung, W. Zhang, A. Manthiram, G. Yu, *Small Methods* **2018**, 2, 1700279.
- [47] M. Zhang, W. Chen, L. Xue, Y. Jiao, T. Lei, J. Chu, J. Huang, C. Gong, C. Yan, Y. Yan, *Adv. Energy Mater.* **2020**, 10, 1903008.
- [48] P. Zeng, B. Su, X. Wang, X. Li, C. Yuan, G. Liu, K. Dai, J. Mao, D. Chao, Q. Wang, *Adv. Funct. Mater.* **2023**, 33, 2301743.
- [49] J. Qin, R. Wang, P. Xiao, D. Wang, *Adv. Energy Mater.* **2023**, 13, 2300611.
- [50] C.-W. Lee, Q. Pang, S. Ha, L. Cheng, S.-D. Han, K. R. Zavadil, K. G. Gallagher, L. F. Nazar, M. Balasubramanian, *ACS Cent. Sci.* **2017**, 3, 605–613.
- [51] L. Cheng, L. A. Curtiss, K. R. Zavadil, A. A. Gewirth, Y. Shao, K. G. Gallagher, *ACS Energy Lett.* **2016**, 1, 503–509.
- [52] J.-Q. Huang, Q. Zhang, F. Wei, *Energy Storage Mater.* **2015**, 1, 127–145.
- [53] L. Luo, A. Manthiram, *Energy Technol.* **2020**, 8, 2000348.
- [54] C. Yan, X.-B. Cheng, C.-Z. Zhao, J.-Q. Huang, S.-T. Yang, Q. Zhang, *J. Power Sources* **2016**, 327, 212–220.
- [55] Y. X. Yao, X. Q. Zhang, B. Q. Li, C. Yan, P. Y. Chen, J. Q. Huang, Q. Zhang, *InfoMat* **2020**, 2, 379–388.
- [56] S. Huang, Z. Wang, Y. Von Lim, Y. Wang, Y. Li, D. Zhang, H. Y. Yang, *Adv. Energy Mater.* **2021**, 11, 2003689.
- [57] R. Fang, S. Zhao, Z. Sun, D. W. Wang, H. M. Cheng, F. Li, *Adv. Mater.* **2017**, 29, 1606823.
- [58] G. Zhang, X. Deng, J. Li, J. Wang, G. Shi, Y. Yang, J. Chang, K. Yu, S.-S. Chi, H. Wang, *Nano Energy* **2022**, 95, 107014.
- [59] N. Azimi, Z. Xue, N. D. Rago, C. Takoudis, M. L. Gordin, J. Song, D. Wang, Z. Zhang, *J. Electrochem. Soc.* **2014**, 162, A64.
- [60] H. A. Ishfaq, C. C. Cardona, E. Tchernychova, P. Johansson, R. Dominko, S. D. Talian, *Energy Storage Mater.* **2024**, 69, 103375.
- [61] X. Cao, H. Jia, W. Xu, J.-G. Zhang, *J. Electrochem. Soc.* **2021**, 168, 010522.
- [62] H. Adenusi, G. A. Chass, S. Passerini, K. V. Tian, G. Chen, *Adv. Energy Mater.* **2023**, 13, 2203307.
- [63] Z. Li, L. P. Hou, N. Yao, X. Y. Li, Z. X. Chen, X. Chen, X. Q. Zhang, B. Q. Li, Q. Zhang, *Angew. Chem.* **2023**, 135, e202309968.
- [64] B. Song, L. Su, X. Liu, W. Gao, T. Wang, Y. Ma, Y. Zhong, X. B. Cheng, Z. Zhu, J. He, *Electron.* **2023**, 1, e13.
- [65] F. Ren, Y. Wu, W. Zuo, W. Zhao, S. Pan, H. Lin, H. Yu, J. Lin, M. Lin, X. Yao, *Energy Environ. Sci.* **2024**, 17, 2743–2752.
- [66] Z. Li, Y. Li, C. X. Bi, Q. K. Zhang, L. P. Hou, X. Y. Li, J. Ma, X. Q. Zhang, B. Q. Li, R. Wen, *Adv. Funct. Mater.* **2024**, 34, 2304541.
- [67] L. Wang, Y. Ye, N. Chen, Y. Huang, L. Li, F. Wu, R. Chen, *Adv. Funct. Mater.* **2018**, 28, 1800919.
- [68] X. Ji, K. T. Lee, L. F. Nazar, *Nat. Mater.* **2009**, 8, 500–506.
- [69] M. A. Weret, W. N. Su, B. J. Hwang, *Batteries & Supercaps* **2022**, 5, e202200059.
- [70] J. Sun, Y. Liu, L. Liu, J. Bi, S. Wang, Z. Du, H. Du, K. Wang, W. Ai, W. Huang, *Adv. Mater.* **2023**, 35, 2211168.
- [71] H. Yuan, J. Q. Huang, H. J. Peng, M. M. Titirici, R. Xiang, R. Chen, Q. Liu, Q. Zhang, *Adv. Energy Mater.* **2018**, 8, 1802107.
- [72] J. He, A. Manthiram, *Energy Storage Mater.* **2019**, 20, 55–70.
- [73] T. Z. Hou, X. Chen, H. J. Peng, J. Q. Huang, B. Q. Li, Q. Zhang, B. Li, *Small* **2016**, 12, 3283–3291.
- [74] W. Li, Q. Zhang, G. Zheng, Z. W. Seh, H. Yao, Y. Cui, *Nano Lett.* **2013**, 13, 5534–5540.
- [75] Y. Zheng, S. Zheng, H. Xue, H. Pang, *J. Mater. Chem. A* **2019**, 7, 3469–3491.
- [76] H. Jiang, X. C. Liu, Y. Wu, Y. Shu, X. Gong, F. S. Ke, H. Deng, *Angew. Chem.* **2018**, 57, 3916–3921.
- [77] R. Mori, *J. Solid State Electrochem.* **2023**, 27, 813–839.
- [78] S. F. Ng, M. Y. L. Lau, W. J. Ong, *Adv. Mater.* **2021**, 33, 2008654.
- [79] W. Yao, J. Xu, L. Ma, X. Lu, D. Luo, J. Qian, L. Zhan, I. Manke, C. Yang, P. Adelhelm, *Adv. Mater.* **2023**, 35, 2212116.
- [80] G. Rong, X. Zhang, W. Zhao, Y. Qiu, M. Liu, F. Ye, Y. Xu, J. Chen, Y. Hou, W. Li, *Adv. Mater.* **2017**, 29, 1606187.
- [81] K. Xie, K. Yuan, K. Zhang, C. Shen, W. Lv, X. Liu, J.-G. Wang, B. Wei, *ACS Appl. Mater. Interfaces* **2017**, 9, 4605–4613.
- [82] L. Yan, N. Luo, W. Kong, S. Luo, H. Wu, K. Jiang, Q. Li, S. Fan, W. Duan, J. Wang, *J. Power Sources* **2018**, 389, 169–177.
- [83] C.-P. Yang, Y.-X. Yin, S.-F. Zhang, N.-W. Li, Y.-G. Guo, *Nat. Commun.* **2015**, 6, 8058.
- [84] Z. Liang, D. Lin, J. Zhao, Z. Lu, Y. Liu, C. Liu, Y. Lu, H. Wang, K. Yan, X. Tao, *Proc. Nat. Acad. Sci.* **2016**, 113, 2862–2867.
- [85] W. Li, H. Yao, K. Yan, G. Zheng, Z. Liang, Y.-M. Chiang, Y. Cui, *Nat. Commun.* **2015**, 6, 7436.
- [86] A. Jozwiuk, B. B. Berkes, T. Weiß, H. Sommer, J. Janek, T. Brezesinski, *Energy Environ. Sci.* **2016**, 9, 2603–2608.
- [87] C. Fang, B. Lu, G. Pawar, M. Zhang, D. Cheng, S. Chen, M. Ceja, J.-M. Doux, H. Musrock, M. Cai, *Nat. Energy* **2021**, 6, 987–994.
- [88] F. Wu, Y.-X. Yuan, X.-B. Cheng, Y. Bai, Y. Li, C. Wu, Q. Zhang, *Energy Storage Mater.* **2018**, 15, 148–170.
- [89] C.-X. Bi, L.-P. Hou, Z. Li, M. Zhao, X.-Q. Zhang, B.-Q. Li, Q. Zhang, J.-Q. Huang, *Energy Mater. Adv.* **2023**, 4, 0010.
- [90] X.-B. Cheng, C. Yan, J.-Q. Huang, P. Li, L. Zhu, L. Zhao, Y. Zhang, W. Zhu, S.-T. Yang, Q. Zhang, *Energy Storage Mater.* **2017**, 6, 18–25.
- [91] H. Liu, X. Sun, X. B. Cheng, C. Guo, F. Yu, W. Bao, T. Wang, J. Li, Q. Zhang, *Adv. Energy Mater.* **2022**, 12, 2202518.
- [92] R. Fang, K. Chen, Z. Sun, G. Hu, D. W. Wang, F. Li, *Interdiscip. Mater.* **2023**, 2, 761–770.
- [93] M. Hagen, P. Fanz, J. Tübke, *J. Power Sources* **2014**, 264, 30–34.
- [94] L. Shi, S. M. Bak, Z. Shadike, C. Wang, C. Niu, P. Northrup, H. Lee, A. Y. Baranovskiy, C. S. Anderson, J. Qin, S. Feng, X. Ren, D. Liu, X. Q. Yang, F. Gao, D. Lu, J. Xiao, J. Liu, *Energy Environ. Sci.* **2020**, 13, 3620–3632.
- [95] M. Zhao, B. Q. Li, H. J. Peng, H. Yuan, J. Y. Wei, J. Q. Huang, *Angew. Chem.* **2020**, 59, 12636–12652.
- [96] F. Schmidt, A. Korzenko, P. Härtel, F. S. Reuter, S. Ehrling, S. Dörfler, T. Abendroth, H. Althues, S. Kaskel, *J. Phys. E* **2022**, 4, 014004.
- [97] A. Bhargav, J. He, A. Gupta, A. Manthiram, *Joule* **2020**, 4, 285–291.
- [98] S. Das, M. Bhuyan, K. N. Gupta, O. Okpowe, A. Choi, J. Sweeny, D. Olawale, V. G. Pol, *Small* **2024**, 20, 2311850.
- [99] Z.-X. Chen, L.-P. Hou, C.-X. Bi, Q. Cheng, X.-Q. Zhang, B.-Q. Li, J.-Q. Huang, *Energy Storage Mater.* **2022**, 53, 315–321.
- [100] Z. Deng, Z. Huang, Y. Shen, Y. Huang, H. Ding, A. Luscombe, M. Johnson, J. E. Harlow, R. Gauthier, J. R. Dahn, *Joule* **2020**, 4, 2017–2029.
- [101] X.-B. Cheng, H.-J. Peng, J.-Q. Huang, R. Zhang, C.-Z. Zhao, Q. Zhang, *ACS Nano* **2015**, 9, 6373–6382.
- [102] K. Hatzell, W. Chang, W. Bao, M. Cai, T. Glossmann, S. Kalnaus, B. Liaw, Y. S. Meng, R. Mohtadi, Y. Wang, *Joule* **2024**, 8, 1550–1555.

- [103] B. Li, *ECS Meeting Abstract MA* **2022**, 01, 109.
- [104] C. Zhao, K. Amine, G.-L. Xu, *Acc. Chem. Res.* **2023**, 56, 2700–2712.
- [105] Q. Cheng, Z. X. Chen, X. Y. Li, C. X. Bi, F. Sun, X. Q. Zhang, X. Ma, B. Q. Li, J. Q. Huang, *Adv. Energy Mater.* **2023**, 13, 2301770.
- [106] D. Capkova, V. Knap, A. S. Fedorkova, D.-I. Stroe, *J. Energy Chem.* **2022**, 72, 318–325.
- [107] Z. Li, I. Sami, J. Yang, J. Li, R. V. Kumar, M. Chhowalla, *Nat. Energy* **2023**, 8, 84–93.
- [108] L. Chen, Y. Sun, X. Wei, L. Song, G. Tao, X. Cao, D. Wang, G. Zhou, Y. Song, *Adv. Mater.* **2023**, 35, 2300771.
- [109] Z. Yu, X. Huang, M. Zheng, S. Q. Zhang, Y. Yang, J. Lu, *Adv. Mater.* **2023**, 35, 2300861.
- [110] X. Huang, J. Xue, M. Xiao, S. Wang, Y. Li, S. Zhang, Y. Meng, *Energy Storage Mater.* **2020**, 30, 87–97.
- [111] X. Huang, M. Xiao, D. Han, J. Xue, S. Wang, Y. Meng, *J. Power Sources* **2021**, 489, 229503.
- [112] L. Huang, T. Lu, G. Xu, X. Zhang, Z. Jiang, Z. Zhang, Y. Wang, P. Han, G. Cui, L. Chen, *Joule* **2022**, 6, 906–922.
- [113] H. Zhou, C. Fear, M. Parekh, F. Gray, J. Fleetwood, T. Adams, V. Tomar, V. G. Pol, P. P. Mukherjee, *J. Electrochem. Soc.* **2022**, 169, 090521.
- [114] M. S. Gonzalez, Q. Yan, J. Holoubek, M. Li, Z. Wu, H. Zhou, S. Kim, H. Liu, B. Y. Jung, S. W. Lee, *Adv. Funct. Mater.* **2021**, 31, 2102198.
- [115] Z. Wei, Y. Ren, J. Sokolowski, X. Zhu, G. Wu, *InfoMat* **2020**, 2, 483–508.
- [116] Z. Wei, N. Zhang, T. Feng, F. Wu, T. Zhao, R. Chen, *Chem. Eng. J.* **2022**, 430, 132678.
- [117] Y. Yang, J. Zhang, *Adv. Energy Mater.* **2018**, 8, 1801778.
- [118] Y. Li, J. Zhang, C. Zhou, M. Ling, J. Lu, Y. Hou, Q. Zhang, Q. He, X. Zhan, F. Chen, *J. Alloys Compd.* **2020**, 826, 154197.
- [119] J. Wang, W. Cai, X. Mu, L. Han, N. Wu, C. Liao, Y. Kan, Y. Hu, *Chem. Eng. J.* **2021**, 416, 129087.
- [120] F.-N. Jiang, S.-J. Yang, Z.-X. Chen, H. Liu, H. Yuan, L. Liu, J.-Q. Huang, X.-B. Cheng, Q. Zhang, *Particuology* **2023**, 79, 10–17.
- [121] K. Liu, T. Ashwin, X. Hu, M. Lucu, W. D. Widanage, *Renewable Sustainable Energy Rev.* **2020**, 131, 110017.
- [122] D. Capkova, V. Knap, A. S. Fedorkova, D.-I. Stroe, *Appl. Energy* **2023**, 332, 120543.
- [123] M. Dubarry, N. Qin, P. Brooker, *Curr. Opin. Electrochem.* **2018**, 9, 106–113.
- [124] A. Krupp, R. Beckmann, T. Diekmann, E. Ferg, F. Schuldt, C. Agert, *Storage Mater.* **2022**, 45, 103506.
- [125] D. T. Boyle, W. Huang, H. Wang, Y. Li, H. Chen, Z. Yu, W. Zhang, Z. Bao, Y. Cui, *Nat. Energy* **2021**, 6, 487–494.
- [126] S.-H. Chung, A. Manthiram, *ACS Energy Lett.* **2017**, 2, 1056–1061.
- [127] S. M. Wood, C. Fang, E. J. Dufek, S. C. Nagpure, S. V. Sazhin, B. Liaw, Y. S. Meng, *Adv. Energy Mater.* **2018**, 8, 1801427.
- [128] L. C. Merrill, S. G. Rosenberg, K. L. Jungjohann, K. L. Harrison, *ACS Appl. Energ. Mater.* **2021**, 4, 7589–7598.
- [129] X. Cao, Y. Xu, L. Zou, J. Bao, Y. Chen, B. E. Matthews, J. Hu, X. He, M. H. Engelhard, C. Niu, *Energy Environ. Sci.* **2023**, 16, 1548–1559.
- [130] X. Cao, L. Zou, B. E. Matthews, L. Zhang, X. He, X. Ren, M. H. Engelhard, S. D. Burton, P. Z. El-Khoury, H.-S. Lim, *Energy Storage Mater.* **2021**, 34, 76–84.
- [131] K. L. Harrison, K. R. Zavadil, N. T. Hahn, X. Meng, J. W. Elam, A. Leenheer, J.-G. Zhang, K. L. Jungjohann, *ACS Nano* **2017**, 11, 11194–11205.
- [132] A. C. Kozen, C.-F. Lin, A. J. Pearse, M. A. Schroeder, X. Han, L. Hu, S.-B. Lee, G. W. Rubloff, M. Noked, *ACS Nano* **2015**, 9, 5884–5892.
- [133] N. Delaporte, Y. Wang, K. Zaghib, *Front. Mater.* **2019**, 6, 267.
- [134] A. Kolesnikov, M. Kolek, J. F. Dohmann, F. Horsthemke, M. Börner, P. Bieker, M. Winter, M. C. Stan, *Adv. Energy Mater.* **2020**, 10, 2000017.
- [135] D. Lin, Y. Liu, Y. Li, Y. Li, A. Pei, J. Xie, W. Huang, Y. Cui, *Nat. Chem.* **2019**, 11, 382–389.
- [136] Z. Wen, W. Fang, L. Chen, Z. Guo, N. Zhang, X. Liu, G. Chen, *Adv. Funct. Mater.* **2021**, 31, 2104930.
- [137] M. Wang, Z. Bai, T. Yang, C. Nie, X. Xu, Y. Wang, J. Yang, S. Dou, N. Wang, *Adv. Energy Mater.* **2022**, 12, 2201585.
- [138] D. Lv, J. Zheng, Q. Li, X. Xie, S. Ferrara, Z. Nie, L. B. Mehdi, N. D. Browning, J. G. Zhang, G. L. Graff, *Adv. Energy Mater.* **2015**, 5, 1402290.
- [139] M. Shaibani, M. S. Mirshekarloo, R. Singh, C. D. Easton, M. D. Cooray, N. Eshraghi, T. Abendroth, S. Dörfler, H. Althues, S. Kaskel, *Sci. Adv.* **2020**, 6, eaay2757.
- [140] N. Kang, Y. Lin, L. Yang, D. Lu, J. Xiao, Y. Qi, M. Cai, *Nat. Commun.* **2019**, 10, 4597.
- [141] X. Yu, J. Deng, R. Lv, Z.-H. Huang, B. Li, F. Kang, *Energy Storage Mater.* **2019**, 20, 14–23.
- [142] D. Cheng, P. Wu, J. Wang, X. Tang, T. An, H. Zhou, D. Zhang, T. Fan, *Carbon* **2019**, 143, 869–877.
- [143] G. Xu, B. Ding, P. Nie, L. Shen, H. Dou, X. Zhang, *ACS Appl. Mater. Interfaces* **2014**, 6, 194–199.
- [144] J. H. Park, W. Y. Choi, J. Yang, D. Kim, H. Gim, J. W. Lee, *Carbon* **2021**, 172, 624–636.
- [145] Y. Xiang, L. Lu, A. G. P. Kottapalli, Y. Pei, *Carbon Energy* **2022**, 4, 346–398.
- [146] J. B. Robinson, K. Xi, R. V. Kumar, A. C. Ferrari, H. Au, M.-M. Titirici, A. Parra-Puerto, A. Kucernak, S. D. Fitch, N. Garcia-Araez, *J. Phys. E* **2021**, 3, 031501.
- [147] Q. Zhao, J. Zheng, L. Archer, *ACS Energy Lett.* **2018**, 3, 2104–2113.
- [148] N. Erisen, N. B. Emerce, S. C. Erensoy, D. Eroglu, *Int. J. Energy Res.* **2018**, 42, 2631–2642.
- [149] Y. Jeoun, M.-S. Kim, S.-H. Lee, J. H. Um, Y.-E. Sung, S.-H. Yu, *Chem. Eng. J.* **2022**, 450, 138209.
- [150] H. Pan, K. S. Han, M. H. Engelhard, R. Cao, J. Chen, J. G. Zhang, K. T. Mueller, Y. Shao, J. Liu, *Adv. Funct. Mater.* **2018**, 28, 1707234.
- [151] J. Liu, Y. Zhou, T. Yan, X. P. Gao, *Adv. Funct. Mater.* **2024**, 34, 2309625.
- [152] H. Pan, Z. Cheng, Z. Zhou, S. Xie, W. Zhang, N. Han, W. Guo, J. Fransaer, J. Luo, A. Cabot, *Nano-Micro Lett.* **2023**, 15, 165.
- [153] C. Shen, J. Xie, M. Zhang, P. Andrei, M. Hendrickson, E. J. Plichta, J. P. Zheng, *J. Electrochem. Soc.* **2019**, 166, A5287–A5294.
- [154] T. Zerrin, R. Shang, B. Dong, E. C. Aguilar, J. Malvin, M. Ozkan, C. S. Ozkan, *Nano Energy* **2022**, 104, 107913.
- [155] M. Baek, H. Shin, K. Char, J. W. Choi, *Adv. Mater.* **2020**, 32, 2005022.
- [156] H. Chu, H. Noh, Y.-J. Kim, S. Yuk, J.-H. Lee, J. Lee, H. Kwack, Y. Kim, D.-K. Yang, H.-T. Kim, *Nat. Commun.* **2019**, 10, 188.
- [157] Q. Pang, A. Shyamsunder, B. Narayanan, C. Y. Kwok, L. A. Curtiss, L. F. Nazar, *Nat. Energy* **2018**, 3, 783–791.
- [158] J. Xia, B. Fitch, A. Watson, J. Cabaniss, R. Black, M. Yakovleva, in *Electrochemical Society Meeting Abstracts* 240, The Electrochemical Society, Inc., **2021**, 362–362.
- [159] T. Wang, J. He, Z. Zhu, X. B. Cheng, J. Zhu, B. Lu, Y. Wu, *Adv. Mater.* **2023**, 35, 2303520.
- [160] T. Zhou, J. Liang, S. Ye, Q. Zhang, J. Liu, *Energy Storage Mater.* **2023**, 55, 322–355.
- [161] H. Li, X. Wang, H. Ma, D. Guo, L. Wu, H. Jin, X. A. Chen, S. Wang, *ChemElectroChem* **2024**, 11, e202300696.
- [162] D. Yang, C. Li, M. Sharma, M. Li, J. Wang, J. Wei, K. Liu, Y. Zhang, J. Li, G. Henkelman, *Energy Storage Mater.* **2024**, 66, 103240.
- [163] J. Xiang, W. Shen, Z. Guo, J. Meng, L. Yuan, Y. Zhang, Z. Cheng, Y. Shen, X. Lu, Y. Huang, *Angew. Chem.* **2021**, 60, 14313–14318.
- [164] G. Liu, W. Wang, P. Zeng, C. Yuan, L. Wang, H. Li, H. Zhang, X. Sun, K. Dai, J. Mao, *Nano Lett.* **2022**, 22, 6366–6374.
- [165] H. Lin, S. Zhang, T. Zhang, H. Ye, Q. Yao, G. W. Zheng, J. Y. Lee, *Adv. Energy Mater.* **2019**, 9, 1902096.
- [166] T. Meng, J. Gao, J. Zhu, N. Li, M. Xu, C. M. Li, J. Jiang, *J. Mater. Chem. A* **2020**, 8, 11976–11985.
- [167] C. Yuan, X. Song, P. Zeng, G. Liu, S. Zhou, G. Zhao, H. Li, T. Yan, J. Mao, H. Yang, *Nano Energy* **2023**, 110, 108353.
- [168] J. Xie, H. J. Peng, J. Q. Huang, W. T. Xu, X. Chen, Q. Zhang, *Angew. Chem.* **2017**, 129, 16441–16445.
- [169] M. Yan, H. Chen, Y. Yu, H. Zhao, C. F. Li, Z. Y. Hu, P. Wu, L. Chen, H. Wang, D. Peng, *Adv. Energy Mater.* **2018**, 8, 1801066.
- [170] M. Jiang, G. Liu, Q. Zhang, D. Zhou, X. Yao, *ACS Appl. Mater. Interfaces* **2021**, 13, 18666–18672.
- [171] S. C. Jo, J. W. Hong, I. H. Choi, M. J. Kim, B. G. Kim, Y. J. Lee, H. Y. Choi, D. Kim, T. Kim, K. J. Baeg, *Small* **2022**, 18, 2200326.
- [172] Y. Zhao, W. Wu, J. Li, Z. Xu, L. Guan, *Adv. Mater.* **2014**, 26, 5113–5118.
- [173] I. Tantis, A. Bakandritsos, D. Zaoralova, M. Medved', P. Jakubec, J. Havlakova, R. Zbořil, M. Otyepka, *Adv. Funct. Mater.* **2021**, 31, 2101326.
- [174] C. Tang, B. Q. Li, Q. Zhang, L. Zhu, H. F. Wang, J. L. Shi, F. Wei, *Adv. Funct. Mater.* **2016**, 26, 577–585.
- [175] Z. Sun, J. Zhang, L. Yin, G. Hu, R. Fang, H.-M. Cheng, F. Li, *Nat. Commun.* **2017**, 8, 14627.
- [176] S. Feng, J. Liu, X. Zhang, L. Shi, C. Anderson, Y. Lin, M.-K. Song, J. Liu, J. Xiao, D. Lu, *Nano Energy* **2022**, 103, 107794.
- [177] R. Fang, S. Zhao, P. Hou, M. Cheng, S. Wang, H.-M. Cheng, C. Liu, F. Li, *Adv. Mater.* **2016**, 28, 3374–3382.
- [178] Z. Yu, M. Liu, D. Guo, J. Wang, X. Chen, J. Li, H. Jin, Z. Yang, X. A. Chen, S. Wang, *Angew. Chem.* **2020**, 132, 6468–6473.
- [179] X. Yang, J. Luo, X. Sun, *Chem. Soc. Rev.* **2020**, 49, 2140–2195.
- [180] X. Tang, X. Guo, W. Wu, G. Wang, *Adv. Energy Mater.* **2018**, 8, 1801897.
- [181] D. Xiong, X. Li, Z. Bai, S. Lu, *Small* **2018**, 14, 1703419.

- [182] L. Guan, H. Hu, L. Li, Y. Pan, Y. Zhu, Q. Li, H. Guo, K. Wang, Y. Huang, M. Zhang, *ACS Nano* **2020**, *14*, 6222–6231.
- [183] P. Wang, B. Xi, M. Huang, W. Chen, J. Feng, S. Xiong, *Adv. Energy Mater.* **2021**, *11*, 2002893.
- [184] L. Sun, Y. Liu, J. Xie, L. Fan, J. Wu, R. Jiang, Z. Jin, *Chem. Eng. J.* **2023**, *451*, 138370.
- [185] L. Wang, G. R. Li, S. Liu, X. P. Gao, *Adv. Funct. Mater.* **2021**, *31*, 2010693.
- [186] P. Xue, K. Zhu, W. Gong, J. Pu, X. Li, C. Guo, L. Wu, R. Wang, H. Li, J. Sun, *Adv. Energy Mater.* **2022**, *12*, 2200308.
- [187] W. Hou, P. Feng, X. Guo, Z. Wang, Z. Bai, Y. Bai, G. Wang, K. Sun, *Adv. Mater.* **2022**, *34*, 2202222.
- [188] Y. Zhang, G. Li, J. Wang, G. Cui, X. Wei, L. Shui, K. Kempa, G. Zhou, X. Wang, Z. Chen, *Adv. Funct. Mater.* **2020**, *30*, 2001165.
- [189] M. Wang, L. Fan, X. Sun, B. Guan, B. Jiang, X. Wu, D. Tian, K. Sun, Y. Qiu, X. Yin, *ACS Energy Lett.* **2020**, *5*, 3041–3050.
- [190] W. Yao, C. Tian, C. Yang, J. Xu, Y. Meng, I. Manke, N. Chen, Z. Wu, L. Zhan, Y. Wang, *Adv. Mater.* **2022**, *34*, 2106370.
- [191] R. Yan, Z. Zhao, M. Cheng, Z. Yang, C. Cheng, X. Liu, B. Yin, S. Li, *Angew. Chem.* **2023**, *135*, e202215414.
- [192] Y. Qi, N. Li, K. Zhang, Y. Yang, Z. Ren, J. You, Q. Hou, C. Shen, T. Jin, Z. Peng, *Adv. Mater.* **2022**, *34*, 2204810.
- [193] J. He, A. Bhargav, A. Manthiram, *ACS Nano* **2021**, *15*, 8583–8591.
- [194] Z. Li, Z. Xiao, S. Wang, Z. Cheng, P. Li, R. Wang, *Adv. Funct. Mater.* **2019**, *29*, 1902322.
- [195] X. Ge, H. Di, P. Wang, X. Miao, P. Zhang, H. Wang, J. Ma, L. Yin, *ACS Nano* **2020**, *14*, 16022–16035.
- [196] J. He, Y. Chen, W. Lv, K. Wen, C. Xu, W. Zhang, Y. Li, W. Qin, W. He, *ACS Nano* **2016**, *10*, 10981–10987.
- [197] K. Chen, Z. Sun, R. Fang, Y. Shi, H. M. Cheng, F. Li, *Adv. Funct. Mater.* **2018**, *28*, 1707592.
- [198] C. Huang, J. Yu, C. Li, Z. Cui, C. Zhang, C. Zhang, B. Nan, J. Li, J. Arbiol, A. Cabot, *Adv. Funct. Mater.* **2023**, *33*, 2305624.
- [199] Y. Song, Z. Sun, Z. Fan, W. Cai, Y. Shao, G. Sheng, M. Wang, L. Song, Z. Liu, Q. Zhang, *Nano Energy* **2020**, *70*, 104555.
- [200] W. Zhao, Y. Lei, Y. Zhu, Q. Wang, F. Zhang, X. Dong, H. N. Alshareef, *Nano Energy* **2021**, *86*, 106120.
- [201] X. Li, Q. Guan, Z. Zhuang, Y. Zhang, Y. Lin, J. Wang, C. Shen, H. Lin, Y. Wang, L. Zhan, *ACS Nano* **2023**, *17*, 1653–1662.
- [202] C. Zhao, G.-L. Xu, Z. Yu, L. Zhang, I. Hwang, Y.-X. Mo, Y. Ren, L. Cheng, C.-J. Sun, Y. Ren, *Nat. Nanotechnol.* **2021**, *16*, 166–173.
- [203] W. G. Lim, C. Y. Park, H. Jung, S. Kim, S. H. Kang, Y. G. Lee, Y. C. Jeong, S. B. Yang, K. Sohn, J. W. Han, *Adv. Mater.* **2023**, *35*, 2208999.
- [204] G. Li, J. Li, K. Wang, J. Zhang, K. Liao, H. Zhang, *ACS Appl. Mater. Interfaces* **2024**, *16*, 35123–35133.
- [205] A. M. Haregewoin, A. S. Wotango, B.-J. Hwang, *Energy Environ. Sci.* **2016**, *9*, 1955–1988.
- [206] S. Zhang, K. Ueno, K. Dokko, M. Watanabe, *Adv. Energy Mater.* **2015**, *5*, 1500117.
- [207] H. Shin, M. Baek, A. Gupta, K. Char, A. Manthiram, J. W. Choi, *Adv. Energy Mater.* **2020**, *10*, 2001456.
- [208] W. Chen, T. Lei, C. Wu, M. Deng, C. Gong, K. Hu, Y. Ma, L. Dai, W. Lv, W. He, *Adv. Energy Mater.* **2018**, *8*, 1702348.
- [209] J. Castillo, J. A. Coca-Clemente, J. Rikarte, A. Sáenz de Buruaga, A. Santiago, C. Li, *APL Mater.* **2023**, *11*, 010901.
- [210] C. Geng, W. Qu, Z. Han, L. Wang, W. Lv, Q. H. Yang, *Adv. Energy Mater.* **2023**, *13*, 2204246.
- [211] C. Luo, X. Liang, Y. Sun, W. Lv, Y. Sun, Z. Lu, W. Hua, H. Yang, R. Wang, C. Yan, *Energy Storage Mater.* **2020**, *33*, 290–297.
- [212] J. Y. Wei, X. Q. Zhang, L. P. Hou, P. Shi, B. Q. Li, Y. Xiao, C. Yan, H. Yuan, J. Q. Huang, *Adv. Mater.* **2020**, *32*, 2003012.
- [213] J. Guo, H. Pei, Y. Dou, S. Zhao, G. Shao, J. Liu, *Adv. Funct. Mater.* **2021**, *31*, 2010499.
- [214] N. Angulakshmi, R. B. Dhanalakshmi, S. Sathya, J. H. Ahn, A. M. Stephan, *Batteries & Supercaps* **2021**, *4*, 1064–1095.
- [215] H. Shi, W. Sun, J. Cao, S. Han, G. Lu, Z. A. Ghazi, X. Zhu, H. Lan, W. Lv, *Adv. Funct. Mater.* **2023**, *33*, 2306933.
- [216] X. Q. Zhang, Q. Jin, Y. L. Nan, L. P. Hou, B. Q. Li, X. Chen, Z. H. Jin, X. T. Zhang, J. Q. Huang, Q. Zhang, *Angew. Chem.* **2021**, *60*, 15503–15509.
- [217] D. Liu, L. Yuan, X. Li, J. Chen, R. Xiong, J. Meng, S. Zhu, Y. Huang, *ACS Appl. Mater. Interfaces* **2022**, *14*, 17585–17593.
- [218] X.-Y. Li, S. Feng, Y.-W. Song, C.-X. Zhao, Z. Li, Z.-X. Chen, Q. Cheng, X. Chen, X.-Q. Zhang, B.-Q. Li, *J. Am. Chem. Soc.* **2024**, *146*, 14754–14764.
- [219] L. P. Hou, Z. Li, N. Yao, C. X. Bi, B. Q. Li, X. Chen, X. Q. Zhang, Q. Zhang, *Adv. Mater.* **2022**, *34*, 2205284.
- [220] L.-P. Hou, X.-Q. Zhang, N. Yao, X. Chen, B.-Q. Li, P. Shi, C.-B. Jin, J.-Q. Huang, Q. Zhang, *Chem.* **2022**, *8*, 1083–1098.
- [221] L. L. Su, N. Yao, Z. Li, C. X. Bi, Z. X. Chen, X. Chen, B. Q. Li, X. Q. Zhang, J. Q. Huang, *Angew. Chem.* **2024**, *136*, e202318785.
- [222] X. Gao, Z. Yu, J. Wang, X. Zheng, Y. Ye, H. Gong, X. Xiao, Y. Yang, Y. Chen, S. E. Bone, *Proc. Natl. Acad. Sci.* **2023**, *120*, e2301260120.
- [223] H. Jia, J. M. Kim, P. Gao, Y. Xu, M. H. Engelhard, B. E. Matthews, C. Wang, W. Xu, *Angew. Chem.* **2023**, *135*, e202218005.
- [224] M. He, X. Li, X. Yang, C. Wang, M. L. Zheng, R. Li, P. Zuo, G. Yin, X. Sun, *Adv. Energy Mater.* **2021**, *11*, 2101004.
- [225] G. X. Liu, J. X. Tian, J. Wan, Y. Li, Z. Z. Shen, W. P. Chen, Y. Zhao, F. Wang, B. Liu, S. Xin, *Angew. Chem.* **2022**, *61*, e202212744.
- [226] Z.-X. Chen, Q. Cheng, X.-Y. Li, Z. Li, Y.-W. Song, F. Sun, M. Zhao, X.-Q. Zhang, B.-Q. Li, J.-Q. Huang, *J. Am. Chem. Soc.* **2023**, *145*, 16449–16457.
- [227] C. Luo, E. Hu, K. J. Gaskell, X. Fan, T. Gao, C. Cui, S. Ghose, X.-Q. Yang, C. Wang, *Proc. Natl. Acad. Sci.* **2020**, *117*, 14712–14720.
- [228] L. Zeng, J. Zhu, P. K. Chu, L. Huang, J. Wang, G. Zhou, X. F. Yu, *Adv. Mater.* **2022**, *34*, 2204636.
- [229] C. Yuan, X. Yang, P. Zeng, J. Mao, K. Dai, L. Zhang, X. Sun, *Nano Energy* **2021**, *84*, 105928.
- [230] P. Zeng, C. Yuan, J. An, X. Yang, C. Cheng, T. Yan, G. Liu, T.-S. Chan, J. Kang, L. Zhang, *Energy Storage Mater.* **2022**, *44*, 425–432.
- [231] C. Prehal, J.-M. von Mentlen, S. Drvarić Talian, A. Vizintin, R. Dominko, H. Amenitsch, L. Porcar, S. A. Freunberger, V. Wood, *Nat. Commun.* **2022**, *13*, 6326.
- [232] Y. T. Liu, S. Liu, G. R. Li, X. P. Gao, *Adv. Mater.* **2021**, *33*, 2003955.
- [233] F. Y. Fan, W. C. Carter, Y.-M. Chiang, *Adv. Mater.* **2015**, *27*, 5203–5209.
- [234] R. Meng, X. He, S. J. H. Ong, C. Cui, S. Song, P. Paoprasert, Q. Pang, Z. J. Xu, X. Liang, *Angew. Chem.* **2023**, *135*, e202309046.
- [235] E. P. Kamphaus, P. B. Balbuena, *J. Phys. Chem. C* **2021**, *125*, 20157–20170.
- [236] M. Cuisinier, P.-E. Cabelguen, B. Adams, A. Garsuch, M. Balasubramanian, L. Nazar, *Energy Environ. Sci.* **2014**, *7*, 2697–2705.
- [237] N. Zhong, C. Lei, R. Meng, J. Li, X. He, X. Liang, *Small* **2022**, *18*, 2200046.
- [238] Y. Chen, T. Wang, H. Tian, D. Su, Q. Zhang, G. Wang, *Adv. Mater.* **2021**, *33*, 2003666.
- [239] W. Zhang, F. Ma, Q. Wu, Z. Zeng, W. Zhong, S. Cheng, X. Chen, J. Xie, *Energy Environ. Mater.* **2023**, *6*, e12369.
- [240] F. Chu, M. Wang, J. Liu, Z. Guan, H. Yu, B. Liu, F. Wu, *Adv. Funct. Mater.* **2022**, *32*, 2205393.
- [241] E. Zhao, K. Nie, X. Yu, Y. S. Hu, F. Wang, J. Xiao, H. Li, X. Huang, *Adv. Funct. Mater.* **2018**, *28*, 1707543.
- [242] L. Zhang, T. Qian, X. Zhu, Z. Hu, M. Wang, L. Zhang, T. Jiang, J.-H. Tian, C. Yan, *Chem. Soc. Rev.* **2019**, *48*, 5432–5453.
- [243] Y. Yang, G. Zheng, Y. Cui, *Chem. Soc. Rev.* **2013**, *42*, 3018–3032.
- [244] R. Xu, J. Lu, K. Amine, *Adv. Energy Mater.* **2015**, *5*, 1500408.
- [245] F. Lin, Y. Liu, X. Yu, L. Cheng, A. Singer, O. G. Shpyrko, H. L. Xin, N. Tamura, C. Tian, T.-C. Weng, *Chem. Rev.* **2017**, *117*, 13123–13186.
- [246] K. A. See, M. Leskes, J. M. Griffin, S. Britto, P. D. Matthews, A. Emly, A. Van der Ven, D. S. Wright, A. J. Morris, C. P. Grey, *J. Am. Chem. Soc.* **2014**, *136*, 16368–16377.
- [247] Y. Yan, C. Cheng, L. Zhang, Y. Li, J. Lu, *Adv. Energy Mater.* **2019**, *9*, 1900148.
- [248] S. Rehman, M. Pope, S. Tao, E. McCalla, *Energy Environ. Sci.* **2022**, *15*, 1423–1460.
- [249] É. A. Santos, M. M. Amaral, B. S. Damasceno, L. M. Da Silva, H. G. Zanin, J. N. Weker, C. Rodella, *Nano Energy* **2024**, *130*, 110098.
- [250] T. Lei, W. Chen, W. Lv, J. Huang, J. Zhu, J. Chu, C. Yan, C. Wu, Y. Yan, W. He, *Joule* **2018**, *2*, 2091–2104.
- [251] X. Yang, X. Gao, Q. Sun, S. P. Jand, Y. Yu, Y. Zhao, X. Li, K. Adair, L. Y. Kuo, J. Rohrer, *Adv. Mater.* **2019**, *31*, 1901220.
- [252] S. Tu, X. Chen, X. Zhao, M. Cheng, P. Xiong, Y. He, Q. Zhang, Y. Xu, *Adv. Mater.* **2018**, *30*, 1804581.
- [253] N. Xu, T. Qian, X. Liu, J. Liu, Y. Chen, C. Yan, *Nano Lett.* **2017**, *17*, 538–543.
- [254] N. Saqib, G. M. Ohlhausen, J. M. Porter, *J. Power Sources* **2017**, *364*, 266–271.
- [255] A. Yang, G. Zhou, X. Kong, R. A. Vilá, A. Pei, Y. Wu, X. Yu, X. Zheng, C.-L. Wu, B. Liu, *Nat. Nanotechnol.* **2020**, *15*, 231–237.
- [256] G. Zhou, A. Yang, G. Gao, X. Yu, J. Xu, C. Liu, Y. Ye, A. Pei, Y. Wu, Y. Peng, *Sci. Adv.* **2020**, *6*, eaay5098.
- [257] H. Dai, L. Gomes, D. Maxwell, S. Zamani, K. Yang, D. Atienza, N. Dale, S. Mukerjee, *ACS Appl. Mater. Interfaces* **2024**, *16*, 8639–8654.

- [258] H. Dai, C. Gallagher, S.-M. Bak, L. Gomes, K. Yang, R. Dong, S. Badhrinathan, Q. Zhao, Y. Du, G.P. Pandey, *ChemRxiv*. 2024, doi:10.26434/chemrxiv-2024-gdbgq.
- [259] J. Conder, R. Bouchet, S. Trabesinger, C. Marino, L. Gubler, C. Villevieille, *Nat. Energy* 2017, 2, 1–7.
- [260] P. Yu, L. X. Feng, D. C. Ma, X. R. Sun, J. K. Pei, X. J. Zha, R. Y. Bao, Y. Wang, M. B. Yang, Z. P. Guo, *Adv. Funct. Mater.* 2021, 31, 2008652.
- [261] J. Lu, T. Wu, K. Amine, *Nat. Energy* 2017, 2, 1–13.
- [262] D. Liu, Z. Shadike, R. Lin, K. Qian, H. Li, K. Li, S. Wang, Q. Yu, M. Liu, S. Ganapathy, *Adv. Mater.* 2019, 31, 1806620.
- [263] W. Yao, K. Liao, T. Lai, H. Sul, A. Manthiram, *Chem. Rev.* 2024, 124, 4935–5118.
- [264] S. Lang, S. H. Yu, X. Feng, M. R. Krumov, H. D. Abruna, *Nat. Commun.* 2022, 13, 4811.
- [265] M. Hagen, P. Schiffels, M. Hammer, S. Dörfler, J. Tübke, M. Hoffmann, H. Althues, S. Kaskel, *J. Electrochem. Soc.* 2013, 160, A1205.
- [266] J.-J. Chen, R.-M. Yuan, J.-M. Feng, Q. Zhang, J.-X. Huang, G. Fu, M.-S. Zheng, B. Ren, Q.-F. Dong, *Chem. Mater.* 2015, 27, 2048–2055.
- [267] W. Zhu, A. Paolella, C.-S. Kim, D. Liu, Z. Feng, C. Gagnon, J. Trottier, A. Vijh, A. Guerfi, A. Mauger, *Sustain. Energy Fuels* 2017, 1, 737–747.
- [268] M. M. Rahman, A. Ronne, N. Wang, Y. Du, E. Hu, *ACS Energy Lett.* 2024, 9, 2024–2030.
- [269] W. Xu, S. Lang, K. Wang, R. Zeng, H. Li, X. Feng, M. R. Krumov, S.-M. Bak, C. J. Pollock, J. Yeo, *Sci. Adv.* 2023, 9, eadi5108.
- [270] P. Zhang, Y. Zhao, Y. Li, N. Li, S. R. P. Silva, G. Shao, P. Zhang, *Adv. Sci. (Weinh)* 2023, 10, 2206786.
- [271] L. Luo, J. Li, H. Yaghoobnejad Asl, A. Manthiram, *ACS Energy Lett.* 2020, 5, 1177–1185.
- [272] Y. Luo, Z. Fang, S. Duan, H. Wu, H. Liu, Y. Zhao, K. Wang, Q. Li, S. Fan, Z. Zheng, *Angew. Chem.* 2023, 62, e202215802.
- [273] Z. Yu, B. Wang, X. Liao, K. Zhao, Z. Yang, F. Xia, C. Sun, Z. Wang, C. Fan, J. Zhang, *Adv. Energy Mater.* 2020, 10, 2000907.
- [274] Y.-C. Lu, Q. He, H. A. Gasteiger, *J. Phys. Chem. C* 2014, 118, 5733–5741.
- [275] H. Schneider, C. Gollub, T. Weiß, J. Kulisch, K. Leitner, R. Schmidt, M. M. Safont-Sempere, Y. Mikhaylik, T. Kelley, C. Scordilis-Kelley, *J. Electrochem. Soc.* 2014, 161, A1399.
- [276] J. R. Macdonald, W. B. Johnson, I. Raistrick, D. Franceschetti, N. Wagner, M. McKubre, D. Macdonald, B. Sayers, N. Bonanos, B. Steele, *Impedance Spectroscopy: Theory, Experiment, and Applications*, John Wiley & Sons 2018.

Manuscript received: August 12, 2024

Revised manuscript received: September 9, 2024

Accepted manuscript online: September 16, 2024

Version of record online: October 30, 2024
